

Chapter 5

Epitaxial Growth of $\text{Si}_{1-y}\text{C}_y$ Alloys

5.1 Introduction

Traditionally, the incorporation of substitutional carbon into silicon and silicon-germanium alloys during growth is of great interest for engineering the strain in silicon layers. Carbon incorporation in SiGe can be used to compensate the compressive strain in SiGe layers grown commensurately w.r.t. silicon. As little as 1% carbon can compensate for the compressive strain induced by 10% Ge in silicon. Achieving high substitutional carbon fraction ($> 1\%$ carbon) in $\text{Si}_{1-y}\text{C}_y$ alloys is important to achieve significant strain for electron mobility improvement by compressively straining the silicon channel. The growth of epitaxial strained silicon-carbon alloys on Si (100) substrates is used in the source-drain regions of MOSFETs to induce tensile stress in channel regions to enhance electron carrier mobility [5.1][5.2]. Carbon in silicon has also been shown to reduce the boron diffusion in silicon [5.3][5.4][5.5]. Only a small fraction of carbon (10^{19} cm^{-3}) [5.3] needs to be incorporated to suppress the diffusion of boron. This was effect was used for the growth of $\text{Si}_{1-x-y}\text{Ge}_x\text{C}_y$ bases for hetero-bipolar junction transistors (HBTs).

5.2 Growth of Si:C Alloy Layers

There are several challenging issues in the growth of $\text{Si}_{1-y}\text{C}_y$ alloys. First, unlike growth with $\text{Si}_{1-x}\text{Ge}_x$ where it is easy to achieve high Ge fractions, it is difficult to achieve high substitutional carbon percentages in silicon. This is due to a significantly larger lattice mismatch between silicon and diamond (35%) than the lattice mismatch

between Si and Ge (4.2%). Second, a stable phase, silicon carbide (SiC) exists between silicon and diamond. Third, carbon also has a low solubility ($3 \times 10^{17}/\text{cm}^3$) in silicon [5.6] [5.7]. Substitutional carbon incorporated into silicon layers at a level above this value will be supersaturated. Fourth, nonsubstitutional carbon is observed to create deep levels in silicon [5.8]. Thus the carbon should be incorporated into a substitutional site and not an interstitial site.

Due to these difficulties, non-equilibrium growth techniques such as MBE and CVD are used to incorporate a high metastable substitutional carbon fraction [5.9][5.10][5.11]. Such non-equilibrium growth causes the buried carbon to be immobilized on the substitutional site [5.12][5.13].

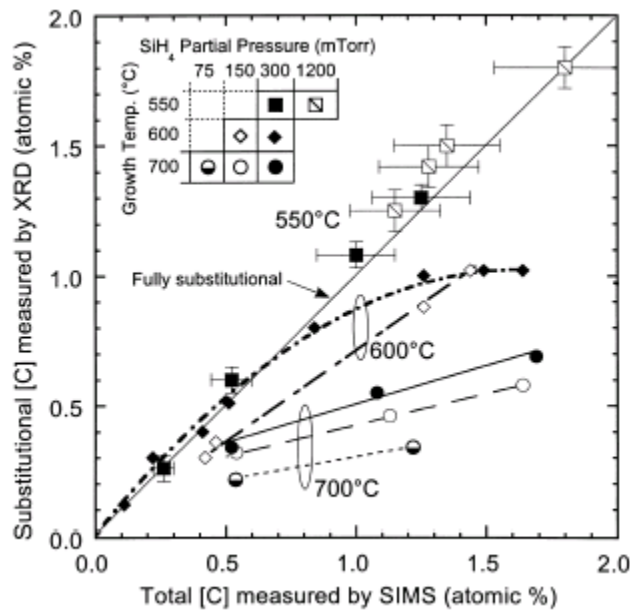


Figure 5.1. Plot of substitutional carbon (measured by the shift in lattice constant by x-ray diffraction) vs. total carbon measured by SIMS [5.11]

From Figure 5.1, the difficulty in the growth of silicon with high carbon percentages is clearly illustrated. From the “fully substitutional” line drawn in Figure 5.1, we observe

that at high temperatures, the carbon incorporates interstitially rather than substitutionally. Lowering the temperature causes more carbon to incorporate into substitutional sites. This illustrates the importance of metastable growth for the incorporation of carbon in silicon, as the carbon atoms on the surface cannot be given enough time to reach their favored (equilibrium) position of being an interstitial. Furthermore, it has been demonstrated in reference [5.11] and in the work of other authors [5.9][5.10] that by using a high growth rate at low temperature more carbon can be incorporated into substitutional sites. As described earlier (Chapter 2) the combination of high growth rate and low temperature are difficult to achieve in CVD epitaxy using silane. The growth of $\text{Si}_{1-y}\text{C}_y$ alloys using DCS as a silicon source (lower growth rate than with silane due to its chlorinated chemistry) and methylsilane [5.11] also indicates that a high growth rate is a necessity for high substitutional carbon incorporation. Therefore, to incorporate high carbon fractions ($>1\%$ carbon in silicon) higher-order silanes are potentially attractive to be used as the silicon source gas because high rates and low temperatures should help for substitutional carbon incorporation. We examined the use of NPS as a silicon source for achieving this goal.

5.3 Determining Substitutional Carbon Fraction in Silicon: Dilute Carbon Alloys

Due to the difference in lattice constant, thin silicon carbon alloy epitaxial layers may be grown pseudomorphic on silicon substrates. The Si:C alloy layer is tensilely strained in the planar directions and compressively strained in the vertical (growth) direction, as shown in Figure 5.2 below.

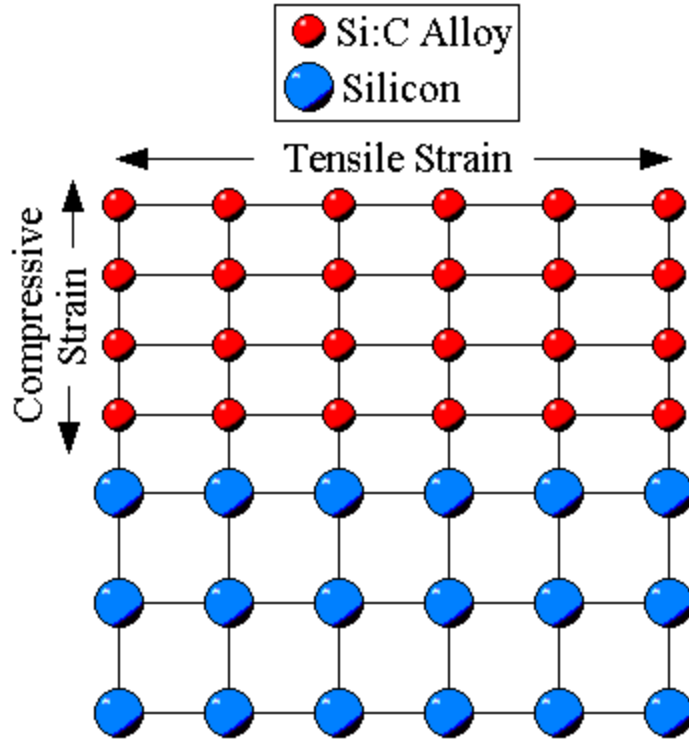


Figure 5.2. Schematic diagram illustrating the silicon substrate lattice and the growth of the pseudomorphic Si:C alloy layers on silicon substrate.

The vertical (004) lattice spacing of the compressively strained layers, a_{\perp} can be determined via x-ray diffraction (XRD) based on the shift from the substrate peak. From a_{\perp} , the carbon percentage can be extrapolated using Poisson's ratio and Vegard's law [5.14][5.15]:

$$\left(\frac{a_{Si_{1-y}C_y}^{\perp} - a_{Si}}{a_{Si}} \right) = \frac{1+\nu}{1-\nu} \left(\frac{a_{Si_{1-y}C_y}^{relaxed} - a_{Si}}{a_{Si}} \right)$$

This is rewritten in the equation below for simplicity:

$$Eq. 5.1 \quad a_{Si_{1-x}C_x}^{\perp} = a_{Si_{1-x}C_x}^{relaxed} + \frac{2C_{11}(x)}{C_{12}(x)} \left[a_{Si_{1-x}C_x}^{relaxed} - a_{Si} \right]$$

where $C_{11}(x)$ and $C_{12}(x)$ are the elastic constants of $Si_{1-x}C_x$ which are linearly extrapolated from Si and C, $a_{Si_{1-x}Cx}^{relaxed}$ is the unstrained bulk lattice constant of $Si_{1-x}C_x$, $a_{Si_{1-x}Cx}^{\perp}$ is the strained lattice constant of $Si_{1-x}C_x$, and a_{Si} is the bulk unstrained lattice constant of silicon (5.431 Ångstroms). The percentage of substitutional carbon varies depending on what model is used for the relaxed lattice constant of $Si_{1-x}C_x$ versus carbon fraction. Vegard's law could be applied between silicon and diamond or silicon and silicon-carbide. An alternate method is proposed by Kelires [5.16] and is generally accepted as the most accurate method in determining the substitutional carbon percentage. However, in this thesis, we use Vegard's law applied between silicon and silicon-carbide.

5.4 Si:C Alloy Epitaxial Layers Grown with NPS and Methylsilane

5.4.1 Growth of Si:C Epitaxial Layers Using NPS and Methylsilane

As described earlier, low temperatures and a high growth rate are generally required for Si:C alloy growth with high substitutional carbon fractions. Si:C alloys were grown with NPS as the silicon source and methylsilane ($SiCH_6$) as the carbon source. The growth pressure was 6 torr and the growth temperature was 575 °C. The thickness of the Si:C epitaxial layers are ~100 nm. Figure 5.3, shows XRD scans done in Princeton, and in Table 5.1 below are the corresponding gas flows of hydrogen, NPS and methylsilane gas flows. The methylsilane source is diluted 1% in hydrogen. The methylsilane flow given in the table is the actual methylsilane flow.

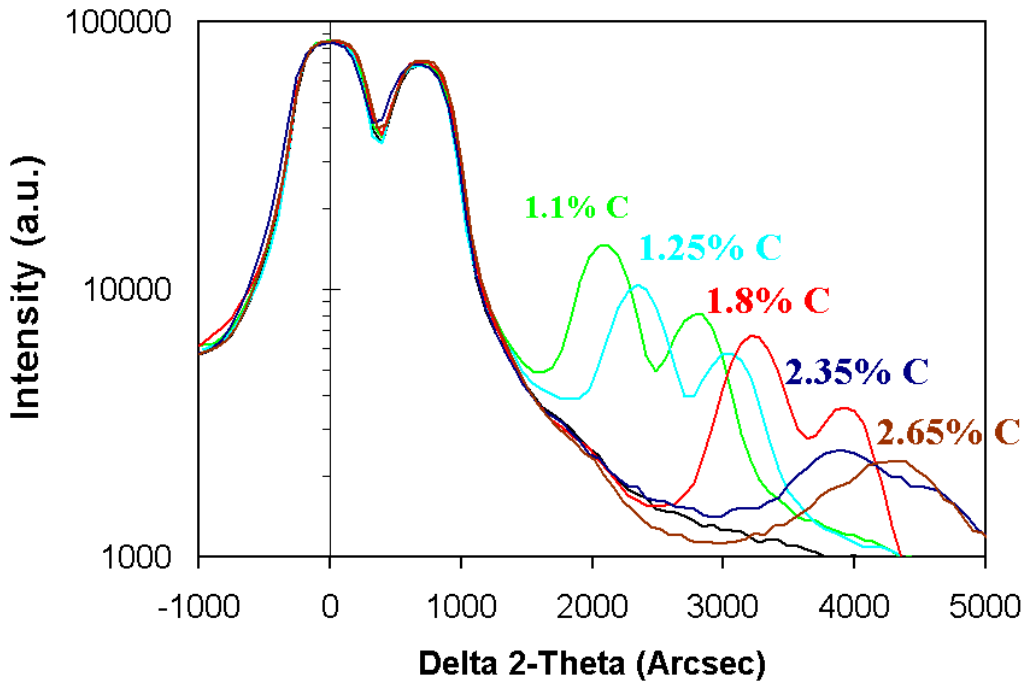


Figure 5.3. XRD rocking curves of various Si:C alloys grown at 575 °C and 6 torr pressure. The hydrogen, NPS and methylsilane flows are given in the table below. The growth thickness of the epitaxial layers is roughly 100 nm.

The two copper k_{α} peaks are not fully resolved out in our experimental setup. We determine the Si:C alloy strained lattice constant from the spacing between the two left peaks. As observed from figure 5.3 above, as the carbon percentage is increased the intensity of the peak is decreasing. At high carbon percentage ($C > 2\%$) the two peaks are difficult to distinguish. This could be due to relaxation of the silicon-carbon layers or a reduction in the layer quality. Assuming the critical thicknesses for commensurately strained $\text{Si}_{1-x}\text{Ge}_x$ and tensilely strained $\text{Si}_{1-y}\text{C}_y$ are similar for the same strain and assuming that 1% carbon compensates for roughly 10% Ge [5.17], the metastable critical thickness for $\text{Si}_{0.985}\text{C}_{0.015}$ layers is roughly 60 nm [5.18]. The results are summarized in the Table 5.1 below.

Table 5.1. Summary growth conditions and substitutional carbon fraction of Si:C alloys grown with NPS and methylsilane as the silicon and carbon sources respectively at a chamber pressure of 6 torr and a temperature of 575 °C.

Sample #	Carbon (XRD) %	H ₂ (sccm)	NPS Bubbler Flow (sccm)	SiCH ₆ (sccm)	H ₂ (partial pressure)	NPS estimated (partial pressure)	SiCH ₆ actual (partial pressure)	Growth Rate (nm/min)
1	1.1	600	50	1	5974 mtorr	17 mtorr	9 mtorr	10
2	1.3	150	50	1	5916 mtorr	54 mtorr	30 mtorr	24
3	1.8	150	30	1	5930 mtorr	36 mtorr	34 mtorr	18
4	2.35	150	20	1	5939 mtorr	25 mtorr	36 mtorr	13
5	2.6	150	15	1	5943 mtorr	20 mtorr	37 mtorr	?

In the table above we compare the substitutional (XRD) carbon levels in Si:C alloys of five samples based on the H₂, NPS (bubbler flow) and SiCH₆ gas flows. From the gas flows we also tabulated the actual partial pressures of H₂, NPS and SiCH₆. The actual NPS flow was estimated to be 3.6% of the NPS bubbler flow (Section 2.2). As observed from Table 5.1, the growth rate can be increases by increasing the NPS flow at fixed pressure and constant hydrogen carrier flow. This requires a commensurate increase in methylsilane flow to keep a high carbon concentration in the grown layer. Because increasing the hydrogen into the NPS bubbler above 50 sccm caused temporary clogging of our mass flow controller and increasing the methylsilane flow was limited by the methylsilane flow controller to 1 sccm (100 sccm of 1% methylsilane in hydrogen), we decreased our hydrogen flow while holding the hydrogen into the NPS bubbler at 50 sccm and held the methylsilane flow constant, as illustrated from the change in sample 1 to sample 2 in the table above. At fixed methylsilane/NPS flow ratio, we are increasing both the partial pressure of NPS and methylsilane, hence growth rate, leading to an increased carbon fraction. Once we were no longer able to decrease the hydrogen flow, we instead reduced the NPS flow to increase carbon levels as shown in Table 5.1 (samples 3 to 5). This increases the methylsilane to NPS ratio leading to more carbon being incorporated despite a reduction in the growth rate. Ideally, we would like to

increase both NPS with methylsilane while decreasing the hydrogen flow however due to limitations in our experimental apparatus we were unable to do so.

In Figure 5.4, we compare the carbon levels measured by SIMS (total carbon) and XRD (substitutional carbon) versus the methylsilane/NPS flow ratio for two different hydrogen carrier flows. The growth conditions were at 575 °C with a chamber pressure of 6 torr in all cases. Two different hydrogen flows of 600 sccm and 150 sccm were compared. By decreasing the hydrogen flow while the NPS and methylsilane ratio is held fixed, the amount of carbon incorporated is increased due to the increase of growth rate, consistent with the results of other authors [5.9][5.11]. As shown in Figure 5.4, by increasing the methysilane to NPS ratio the amount of carbon incorporated can be increased.

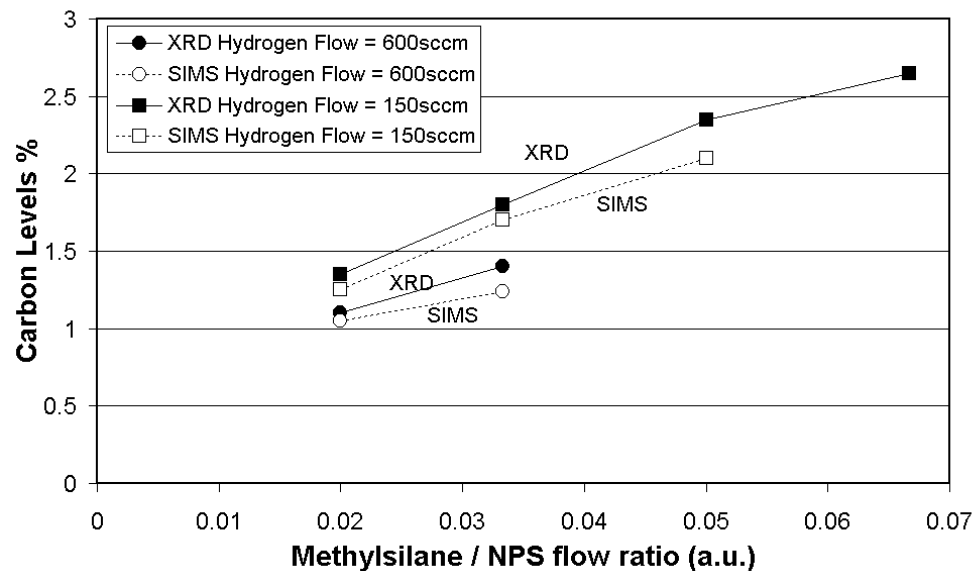


Figure 5.4. Carbon percentage determined by SIMS and calculated from XRD data versus the ratio of methylsilane to NPS source flow at fixed hydrogen flow. The squares represent hydrogen flow of 150 sccm and circles represent hydrogen flow of 600 sccm. The growth temperature was 575 °C and the chamber pressure was 6 torr.

The substitutional carbon percentage calculated from the XRD was then compared with the total carbon percentage determined from SIMS to determine if the $\text{Si}_{1-y}\text{C}_y$ alloys grown are fully substitutional. In Figure 5.5 below we compare substitutional carbon (XRD) vs. total carbon (SIMS) for growth conditions at 575 °C and 6Torr, with varying NPS, methylsilane and hydrogen flows. Relative error bars of 5% and 15% were used for the XRD and SIMS measurements respectively.

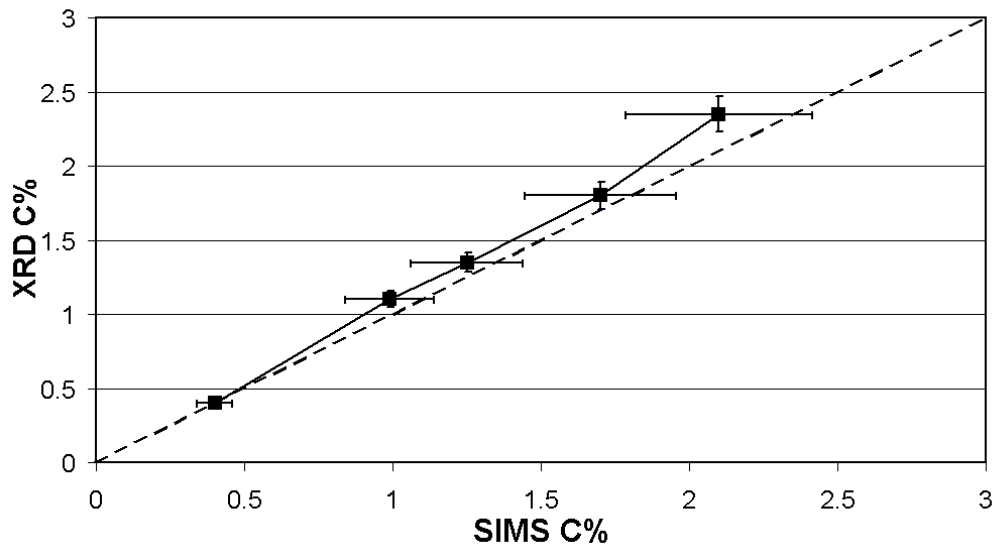


Figure 5.5. Comparison of substitutional carbon percentage measured from XRD vs. total carbon percentage determined by SIMS. Relative error bars of 5% and 15% were used for the XRD and SIMS measurements respectively. The dotted line represents fully substitutional carbon.

The dotted line in the figure is used to depict fully substitutional carbon levels. If the value calculated from XRD is equivalent to the carbon measured by SIMS then the carbon incorporated is fully substitutional. If the carbon measured from SIMS is greater than the carbon level determined from XRD then the carbon incorporated is partially interstitial or the grown layer is relaxed, causing a reduction in the value calculated from

XRD. It can be inferred that fully substitutional carbon percentages up to 2.1% has been achieved within the error bars of XRD and SIMS measurements.

To determine the quality of our $\text{Si}_{1-x}\text{C}_x$ epitaxy layers, high resolution X-ray diffraction (HR-XRD), (courtesy of Applied Materials) was performed on the as-grown silicon-carbon alloy layer of 1.8% using the same conditions depicted in Table 5.1 above and shown in Figure 5.3 above. The X-ray rocking curve of an ideal Si:C alloy layer of 1.8% carbon and 100 nm thickness was simulated. The HR-XRD and computer simulation result is plotted in Figure 5.6 below:

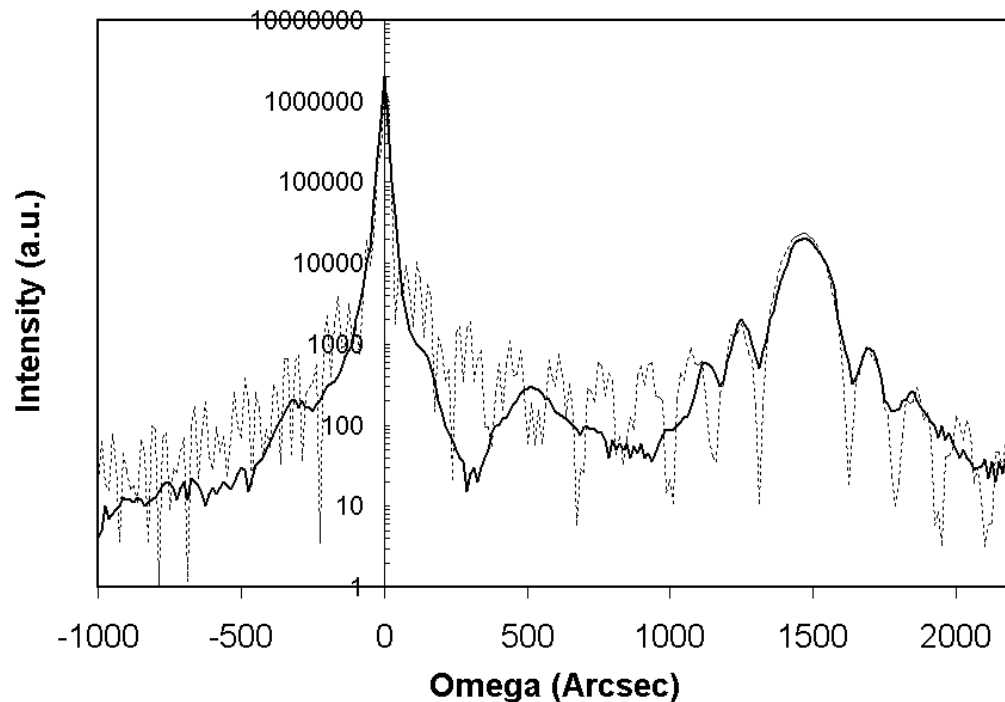


Figure 5.6. High-Resolution X-Ray Diffraction (HR-XRD) of a 130nm $\text{Si}_{1-y}\text{C}_y$ layer on Si showing a substitutional carbon level of 1.8% with lattice constant of 5.375 \AA . The solid line represents the raw data while the dotted lines indicates simulation. The growth temperature was 575 °C and the growth rate was 20 nm / min.

The as grown sample is in excellent agreement with the simulated result with several satellite peaks visible around the main $\text{Si}_{1-y}\text{C}_y$ peak indicating that the epitaxial silicon-carbon alloy layer is of high quality up to 1.8% of substitutional carbon.

5.4.2 Comparison of Growth Rates for High-Carbon Fraction Layers with Other Works

Comparison of our work to other reports of fully substitutional carbon with high carbon percentages by Rapid Thermal CVD (or fundamentally similar Low Pressure CVD) reveals that we have generally achieved the same substitutional carbon percentages at a slightly higher temperature and much higher growth rate (Table 5.2), although very little on growth rates from other groups has been reported. The growth rate versus carbon fraction is plotted in Figure 5.7 below, using the data from Table 5.1, Table 5.3, and references [5.8] and [5.19] and a data point at 575 °C at 6 torr using a hydrogen flow of 150 sccm with NPS flow of 2.1 sccm and MS flow of 2.5 sccm. The more concentrated methylsilane bottle allowed for a larger partial pressure of methylsilane without the need to eliminate the hydrogen carrier flow. This led to higher growth rates at the same NPS to methylsilane ratio, as now more NPS could be injected. Table 5.2 is a summary of the work done in our lab compared with the work done by other groups.

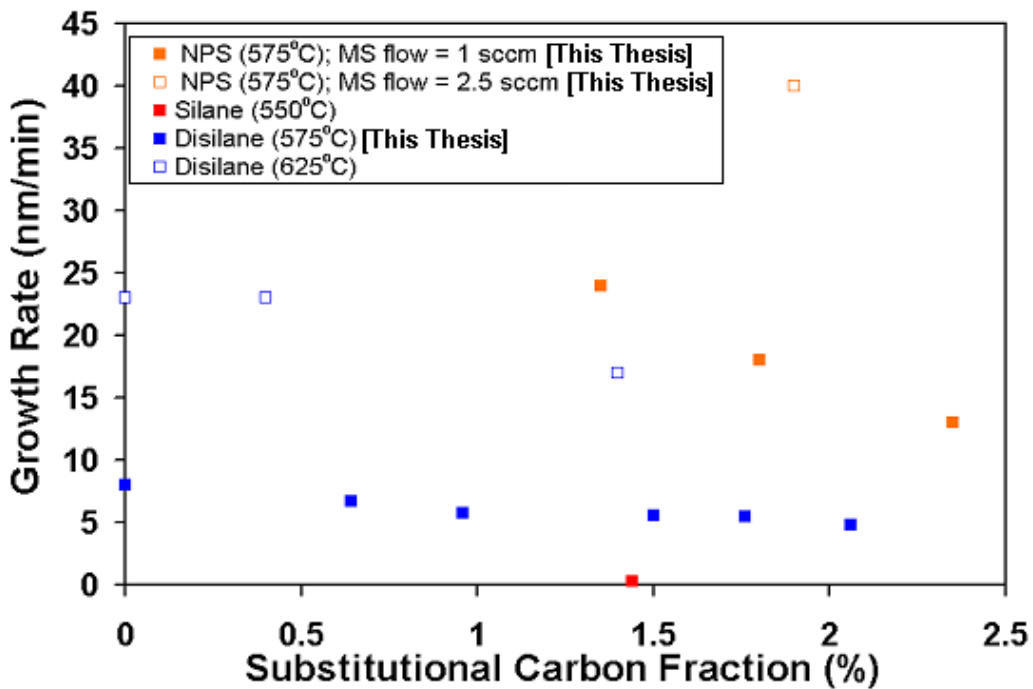


Figure 5.7. Growth rate versus substitutional carbon fraction for silane (red), disilane (blue) and NPS (orange). The growth conditions are given in Table 5.1 for NPS (orange filled square), Table 5.2 for disilane at 575 °C (blue filled square), reference 5.8 for silane (red), and reference 5.20 for disilane at 625 °C (blue open square), and 6 torr with 150 sccm hydrogen flow and a MS flow of 2.5 sccm for the NPS open square.

Table 5.2. Comparison of fully substitutional carbon % in silicon among different precursors.

Precursor	Silane [5.9]	Silane [5.14]	Disilane [5.20]	Trisilane [5.21]	NPS
Carbon Fraction %	1.8	1.44	2.35	2.6	1.9 / 2.1
Growth Rate (nm/min)	N/A	0.3	N/A	55	40 / 13
Temperature °C	550	550	525	550	575

We have demonstrated that NPS is a superior silicon source compared with disilane and silane for the incorporation of carbon rich silicon layers. We have achieved up to a growth rate of 40 nm/min for up to 1.9% carbon in silicon, significantly faster than that with silane. Also, for the same temperature (575 °C) the growth rates with NPS and

methylsilane are higher than the growth rates with disilane and methylsilane (see Figure 5.7). Furthermore, Si:C layers grown at higher growth rates have smaller oxygen concentrations and can be fully substitutional for up to 2% of carbon in silicon layers. Recently, growth of n-type Si:C layers with trisilane have been reported to have up to 2.6% C substitutionally at 550 °C with a growth rate of 55 nm/min [5.21]. Because similar growth mechanisms are expected in high-order silanes (i.e. trisilane, NPS etc.), this is consistent with our results that high-order silanes are technologically useful for achieving high substitutional carbon at high growth rates and low-temperatures. We were not able to achieve the same carbon fraction with NPS as published with trisilane. This is due to the fact that neither our NPS nor methylsilane sources were purified. Oxygen contamination is a well-known cause of the breakdown of epitaxy. Its effect is more enhanced in Si:C epitaxial alloy layers, probably due to an unknown surface effect related to carbon (see the next section).

5.4.3 Oxygen in Si:C Epitaxial Layers Grown with NPS and Methylsilane

Having achieved a high substitutional carbon fraction ($C > 2\%$) in silicon-carbon alloys, we wish to examine the background impurities in those layers with SIMS. We compared samples grown at 575 °C and 6 torr, with different NPS, hydrogen and methylsilane flows. The NPS gas source is impure and contaminated with oxygen. The background level of oxygen in films grown with NPS at 575 °C is $\sim 7 \times 10^{17}/\text{cm}^3$ but the gas impurity concentrations are unknown. The methylsilane gas source (Voltaix with 99.9% purity) has argon and oxygen impurity level of 2 ppmv and a carbon dioxide impurity level of 10 ppmv. The water impurity level is not reported. The methylsilane was 1% concentration diluted in 5N hydrogen (99.999% purity level) for all samples except for sample 4313 where the concentration was 5% methylsilane in hydrogen. The

carrier hydrogen gas used is 6N hydrogen (99.9999% purity level). There may be high levels of oxygen in our films; both our silicon source, NPS, and our carbon source, methylsilane (a.k.a mono-methylsilane, abbreviated MMS), are impure.

The background oxygen concentration measured by SIMS was plotted against the total carbon fraction below in Figure 5.8.

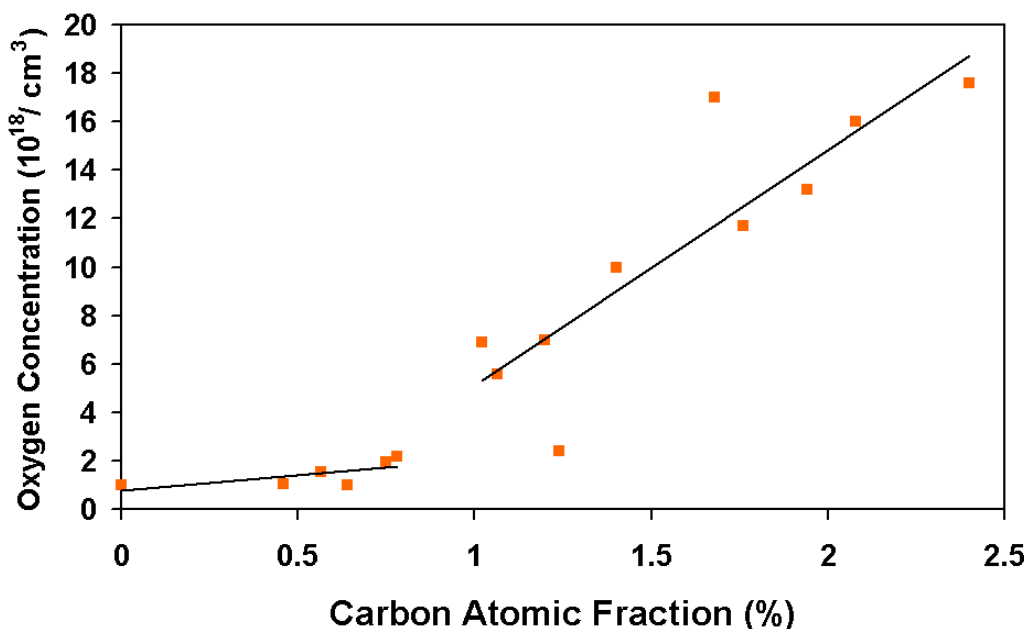


Figure 5.8. Background oxygen concentration measured by SIMS versus carbon percentage (XRD). The growth pressure was 6 torr and the growth temperature was 575 °C for all samples. All samples were grown with NPS and methylsilane. The background concentration of oxygen in silicon grown with NPS at this temperature is $\sim 10^{18} / \text{cm}^3$. Two least squares regression lines were plotted to describe the two different slopes of oxygen incorporation.

Based on Figure 5.8, there appears to be a point at around 1% carbon incorporated where the oxygen concentration in the sample seems to be rising. For small amounts of carbon incorporated ($C < 1\%$) the background oxygen concentration is around $\sim 10^{18} - 2 \times 10^{18} \text{ cm}^{-3}$ with a very slow increase of oxygen for an additional amounts of carbon (10^{18} cm^{-3} for 1% carbon increase). For carbon levels over 1% in silicon the total amount of oxygen

incorporated is then increasing at a faster rate, with the total amount of carbon incorporated ($13 * 10^{18}$ for 1% carbon increase). We would like to determine reason for the two different slopes and why oxygen increases when more carbon is incorporated. Unlike $\text{Si}_{1-x}\text{Ge}_x$ where addition germanium enhances desorption of hydrogen, (which leads to more open sites and hence oxygen incorporation), carbon does not have this effect [5.22]. We would like to determine if this increase in oxygen is due to the impure NPS source, the methylsilane source, or some other effect. We will attribute the “other effect” as a carbon-related surface effect. We now add a plot of methylsilane partial pressure and NPS partial pressure versus the carbon percentage on the secondary y-axis, shown in Figure 5.9 below:

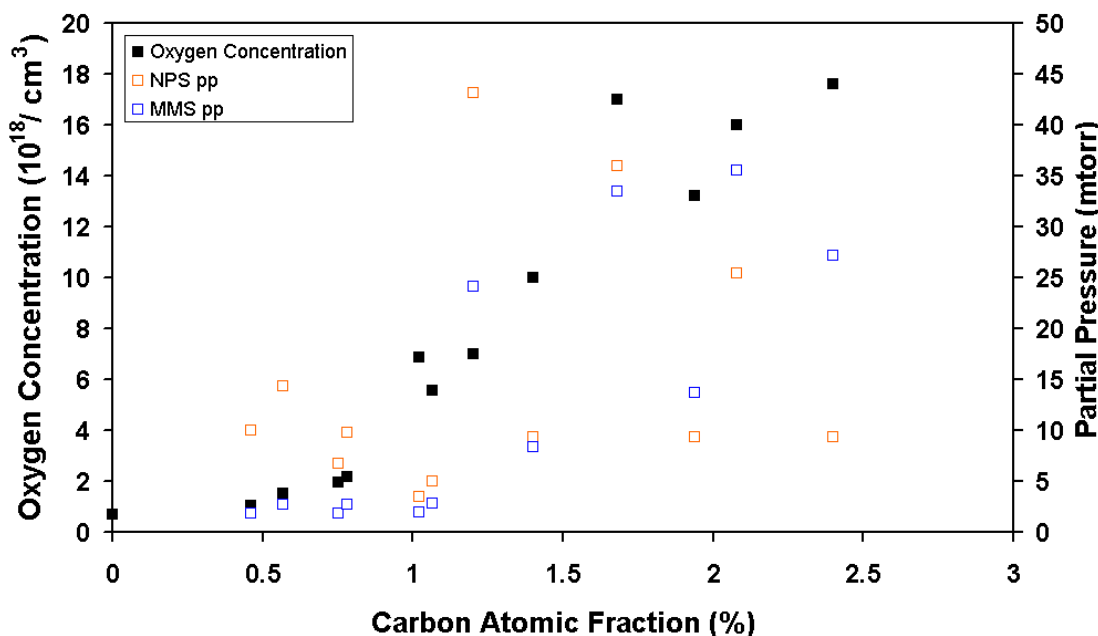


Figure 5.9. Oxygen concentration (solid squares) measured by SIMS vs. carbon atomic fraction (SIMS). The corresponding methylsilane (MMS) (blue open squares) and NPS (orange open squares) are plotted on the secondary y-axis. The growth pressure was 6 torr and the growth temperature was 575 °C for all samples.

From the plot we observe that the oxygen concentration (solid squares) is not highly correlated to the NPS partial pressure (orange open squares). It is evident that there is more of a relation between the oxygen concentration and the MMS partial pressure (blue open squares), although there is still some variance among the sample points. This may be due to the fact that the samples have slightly different growth rates. Since neither the impurities from the NPS or the MMS gas sources can account fully for the oxygen concentration, this implies that there is also surface effect due carbon that causes additional adsorption of oxygen. We will plot the adsorption rate of oxygen onto the Si:C surface. We make the assumption that the adsorption rate (A_{Oxygen}) is equivalent to the incorporation rate, which is the oxygen concentration times the growth rate. At our temperatures and partial pressures oxygen is stable on a silicon surface (i.e. oxygen does not desorb) [1.6]. The adsorption rate is the amount of oxygen that lands on the surface. The oxygen will come from the source and carrier gases (i.e. hydrogen, MMS and NPS). The amount that adsorbs will be proportional to the sticking coefficient. The sticking coefficient may be a function of the carbon concentration in the film, since the silicon oxygen bond and a carbon oxygen bond have different bond enthalpies.

We plot the adsorption rate of oxygen in Figure 5.10 below and tabulate the results in Table 5.3.

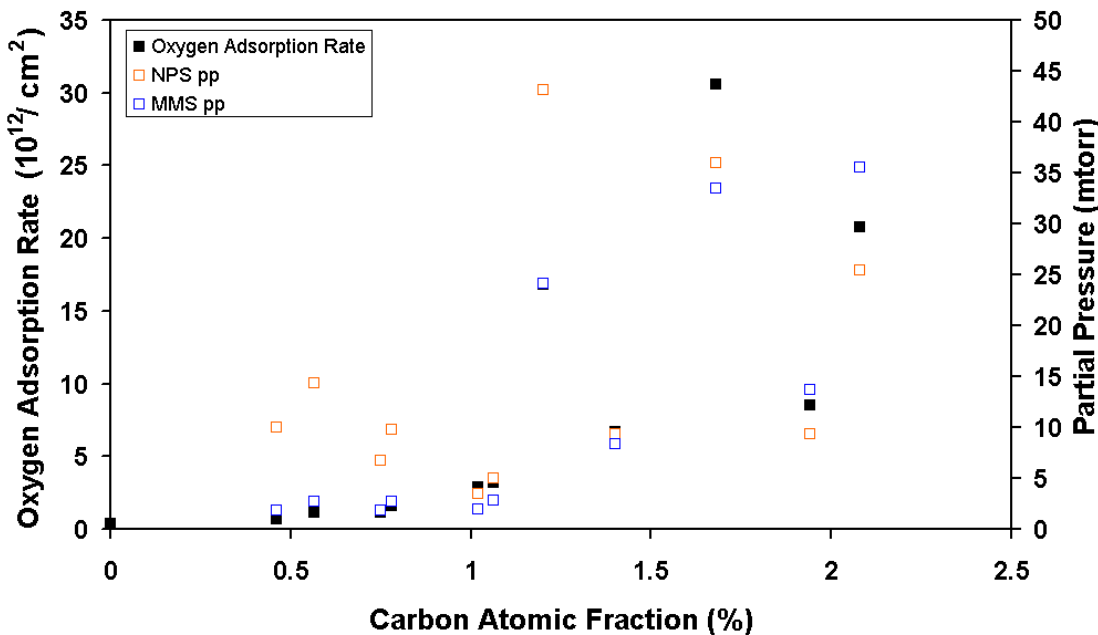


Figure 5.10. Oxygen adsorption rate (solid squares) vs. carbon atomic fraction. The corresponding methylsilane (MMS) (blue open squares) and NPS (orange open squares) are plotted on the secondary y-axis. The growth pressure was 6 torr and the growth temperature was 575 °C for all samples.

Table 5.3. Summary of growth conditions and total carbon fraction of Si:C alloys grown with NPS and methylsilane as the silicon and carbon sources respectively at a chamber pressure of 6 torr and a temperature of 575 °C. The growth rate, carbon and oxygen concentrations were determined by SIMS analysis with errors of 10%, 5% and 5% respectively. The NPS and MMS partial pressures are the actual partial pressures (estimated at 3.6% of the bubbler flow for NPS).

Sample #	H ₂ flow (sccm)	NPS flow (sccm)	MS flow (sccm)	H ₂ pp (mtorr)	NPS pp (mtorr)	MMS pp (mtorr)	GR (nm/min)	C %	O ₂ ¹⁸ (10 ¹⁸ cm ⁻³)	A _{Oxygen} (10 ¹² /s)
A	3100	150	1	5988	9.8	1.9	6.8	0.46	1.0	0.71
B	2100	150	1	5983	14.4	2.7	7.6	0.57	1.5	1.16
C	3100	100	1	5991	6.8	1.9	6	0.75	2.0	1.17
D	2100	100	1	5987	9.8	2.7	7.3	0.78	2.2	1.58
E	3100	50	1	5995	3.4	1.9	4.2	1.02	6.9	2.89
F	2100	50	1	5992	5.0	2.8	5.8	1.06	5.6	3.23
G	200	50	1	5933	43.2	24.1	24	1.2	7.0	16.8
H	1030	50	1.5	5982	9.4	8.3	6.7	1.4	10	6.67
I	150	30	1	5930	36	33.5	18	1.68	12	30.6
J	1045	50	2.5	5978	9.4	13.7	6.5	1.94	13	8.54
K	150	20	1	5939	24.5	35.5	13	2.1	16	20.8

We compare samples with the same MS partial pressure and varying NPS partial pressure. Comparing samples A, C, and E, we find that as the NPS partial pressure is decreased from (9.8 to 6.8 then to 3.4 mtorr), the adsorption rate of oxygen is increasing. The total background oxygen impurity level is decreasing since less NPS is used from samples A to C to E, yet the adsorption rate is increasing in the same order. This indicates that the carbon on the surface is increasing the oxygen sticking probability. While there is more oxygen in the background for sample “A” then for sample “C”, less of the oxygen is adsorbed onto the surface and incorporated. A comparison between B and D also leads us to the same conclusion. We also note that the adsorption rate of oxygen is not directly proportional to the carbon percentage. In Figure 5.10 above, we observe that the adsorption rate increases with carbon fraction and is also dependent on the NPS and MMS partial pressures. This indicates that more of the background oxygen is adsorbed onto the surface and incorporated into the film as the carbon atomic fraction is increased. Due to the varying gas flow condition of the samples and growth rates; it is difficult to separate the contributions to the oxygen background from the three sources of oxygen contamination (NPS, methylsilane, surface effect). This is due to the variance of the total oxygen background impurities from NPS and MMS used in the samples. We write an equation for the adsorption of oxygen onto the Si:C surface by splitting the adsorption of oxygen on silicon sites and on carbon sites.

$$\text{Eq. 5.2} \quad O_{\text{Total}} = (1-y)O_{\text{Si}_{1-y}} + k^n * y * O_{\text{C}_y}$$

Where O_{total} is the total oxygen adsorption rate, O_{Si} and O_{C} are the contributions from adsorption on top a silicon surface site and carbon surface site respectively, y is the carbon fraction, and k^n is a scaling constant to account for the difference in the adsorption rates, due to difference in the frequency of hydrogen desorption from a silicon site versus

a carbon site between a silicon site and a carbon site, and of order n., similar to the difference in frequency of hydrogen desorption from a germanium site versus a silicon site in SiGe films [5.23][5.24]. We can further separate the components based on the impurities coming from MMS and NPS.

$$\text{Eq. 5.3} \quad O_{Total} = (1-y)[O_{Si_{1-y}}(NPS) + O_{Si_{1-y}}(MMS)] + k^n * y * [O_{C_y}(NPS) + O_{C_y}(MMS)]$$

Where O_{Si} (NPS) is the oxygen adsorbed onto a silicon site due to oxygen from the NPS source, O_{Si} (MMS) is the oxygen adsorbed onto a silicon site due to oxygen form the MMS source, O_C (NPS) is the oxygen adsorbed onto a carbon site due to oxygen from the NPS source, O_C (MMS) is the oxygen adsorbed onto a carbon site due to oxygen form the MMS source. Based on this equation, we can explain the good correlation between the MMS pressure and oxygen adsorption into the film. Both the carbon atomic fraction and the amount of oxygen adsorbed are dependent on the MMS source. This implies that for good carbon growth a low oxygen impurity or purified MMS source is needed. Further work and knowledge of the actual oxygen impurity concentrations of both the MMS and NPS is needed to separate out the contributions due to each component and will not be done in this thesis.

The effect of the growth rate and temperature on the amount of oxygen incorporated into the films was next examined. We use a set of growth conditions which all yield approximately 1% carbon. The methysilane silane flow rate was set to 1 sccm and the flow through the NPS bubbler was set at 50 sccm for all samples. The plot of these two sets of data are shown in Figure 5.11 below and tabulated in Table 5.4:

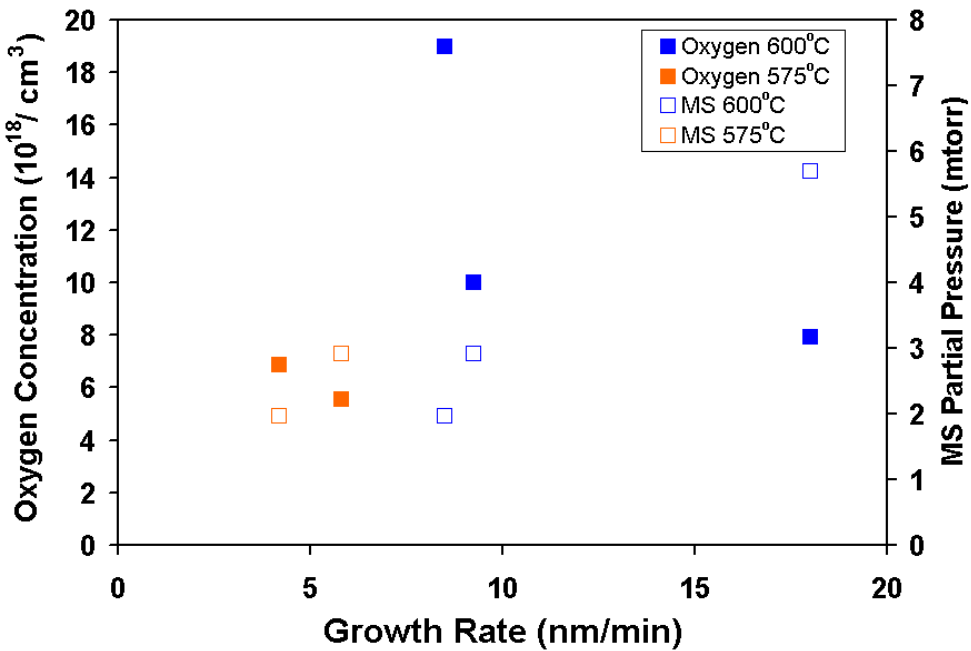


Figure 5.11. Background oxygen concentration (solid squares) measured by SIMS versus growth rate. The corresponding methylsilane (MS) partial pressure (open squares) was plotted on the secondary y-axis. The growth pressure was 6 torr and the growth temperature was 600 °C (blue) and 575 °C (orange). The carbon percentage for all samples is ~1%. The methylsilane silane flow rate was set to 1 sccm and the flow through the NPS bubbler was set at 50 sccm for all samples.

Table 5.4. Growth conditions of ~1% carbon atomic fraction in silicon at 575 °C and 600 °C, with NPS and MMS at 6 torr. The growth rate, carbon and oxygen concentrations were determined by SIMS analysis with errors of 10%, 5% and 5% respectively.

Temp	H ₂ flow (sccm)	NPS flow (sccm)	MS flow (sccm)	H ₂ pp (mtorr)	NPS pp (mtorr)	MMS pp (mtorr)	GR (nm/min)	C %	O ₂ (10^{18} cm^{-3})	A _{Oxygen} ($10^{12}/\text{s}$)
575°C	3100	50	1	5995	3.4	1.9	4.2	1.02	6.9	2.89
575°C	2100	50	1	5992	5.0	2.8	5.8	1.06	5.6	3.23
600°C	3100	50	1	5995	3.4	1.9	8.5	0.98	19.0	16.2
600°C	2100	50	1	5992	5.0	2.8	9.2	1.02	10.5	9.71
600°C	1100	50	1	5985	9.4	5.4	18	1.17	7.9	14.3

Comparing the oxygen levels (Figure 5.11) at the two different growth temperatures of 575 °C (orange) and 600 °C (blue), it is evident that for carbon percentage, a reduction in temperature also leads smaller amounts of oxygen incorporated even though the growth

rate is reduced. The adsorption rate of the oxygen (Table 5.4) is lower at the lower temperature although the background impurity levels are the same (i.e. same NPS and MMS partial pressures). There may be a higher surface concentration of carbon at the higher temperatures leading to a higher adsorption rate of oxygen, and that not all of the carbon is incorporated (i.e. surface segregation of carbon [5.25]). This could explain the variance and lack of dependence of the adsorption rate on the MMS and NPS partial pressures. The concentration of carbon of the surface is different for the samples even though the amount incorporated is ~1% atomic fraction. Surface segregation effects are covered in detail in chapter 7. The data implies that lower growth temperatures are better for background oxygen concentrations in Si:C alloy epitaxial layers. As the growth rate is increased the amount of oxygen incorporated into the film is also decreased. We would like to note that the methylsilane partial pressure does not correlate with the oxygen concentration (for a set carbon concentration), indicating that a high growth rate can reduce the effect of oxygen contamination coming from the methylsilane. This reduction is not due to a decrease in adsorption rate of oxygen on the surface but by decreasing the amount incorporated by increasing the growth rate.

We conclude that the higher the growth rate and the lower the temperature, the lower background oxygen in the Si:C epitaxy. The oxygen is probably coming from impure methylsilane and NPS sources and the adsorption is enhanced on a Si:C surface.

5.5 Si:C Alloy Epitaxial Layers Grown with Disilane and Methylsilane

5.5.1 Growth of Si:C Epitaxial Layers Using Disilane and Methylsilane

Si:C alloy epitaxial layers were also grown on Si (100) wafers in our reactor system using disilane as the silicon source and methylsilane as the carbon source. This allows for the comparison of two different silicon precursors (disilane and NPS). We can then determine how much of an effect the higher growth rate has on carbon incorporation. The use of disilane and methylsilane to grow Si:C alloy epitaxial layers has also been done by a previous student using 625 °C and 6 torr as the growth temperature and chamber pressure respectively, and their results are well documented in references [5.19][5.26]. We grow Si:C alloy epitaxial layers at 575 °C and 6 torr pressure, to compare the layers with those grown using NPS as the silicon source.

Our disilane source is 10% disilane in hydrogen. The methylsilane source is 5% methylsilane in hydrogen. The actual disilane flow was set to 10 sccm and hydrogen carrier flow was set to 3 slpm, the methylsilane flow was varied. The XRD of the layers grown are shown in Figure 5.12 below and summarized in Table 5.5:

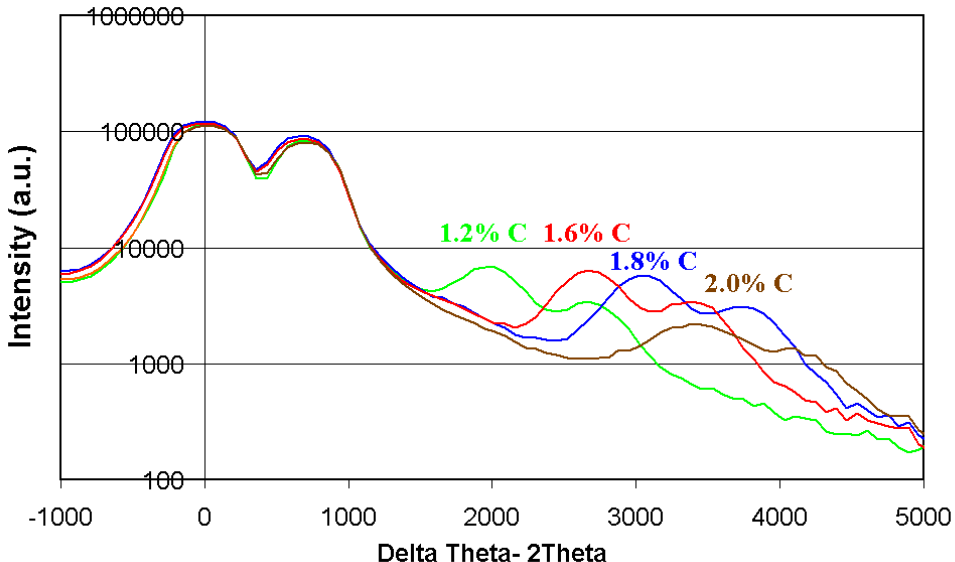


Figure 5.12. XRD rocking curves of various Si:C alloys grown at 575 °C and 6 torr pressure. The hydrogen, Disilane and methylsilane flows are given in the table below. The growth thickness of the epitaxial layers is roughly 100 nm.

Table 5.5. Summary of growth conditions and total carbon fraction of Si:C alloys grown with disilane (DS) and methylsilane (MS) as the silicon and carbon sources respectively at a chamber pressure of 6 torr and a temperature of 575 °C. Two sample numbers are given, the first one for the SIMS sample (multiple Si:C layers) and the second for the XRD sample (single Si:C layers of approximately ~100nm) grown under the same conditions. The disilane and methylsilane flows are tabulated as the actual flow.

Sample #	H ₂ flow (sccm)	DS flow (sccm)	MS flow (sccm)	H ₂ pp (mtorr)	DS pp (mtorr)	MS pp (mtorr)	GR (nm/min)	C % SIMS	C % XRD
Average	3090	10	0	5980.6	19.4	0	7	0	0
4845 4679	3109	10	1	5978.9	19.2	1.9	6.7	0.64	0.7
4845 4676	3128	10	2	5977	19.1	3.9	5.8	1.24	1.2
4943 4680	3137.5	10	2.5	5976.2	19	4.8	5.6	1.5	1.57
4845 4679	3147	10	3	5975.2	19	5.8	5.5	1.76	1.78
4943 4687	3156.5	10	3.5	5974.3	18.9	6.8	4.8	2.06	2.0

From the results above, we observe that up to 2% substitutional carbon can be incorporated in films using disilane and methylsilane. The growth rate of disilane is less than the growth rate using NPS. Also, similar to the Si:C films grown with NPS (Figure 5.3) the intensity of the XRD rocking curve for the Si_{0.98}C_{0.02} sample is less than intensity

of the other samples. This is likely to indicate degradation in epitaxy quality. Figure 5.13 below compares substitutional carbon (XRD) vs. total carbon (SIMS) for growth conditions at 575 °C using disilane and methylsilane.

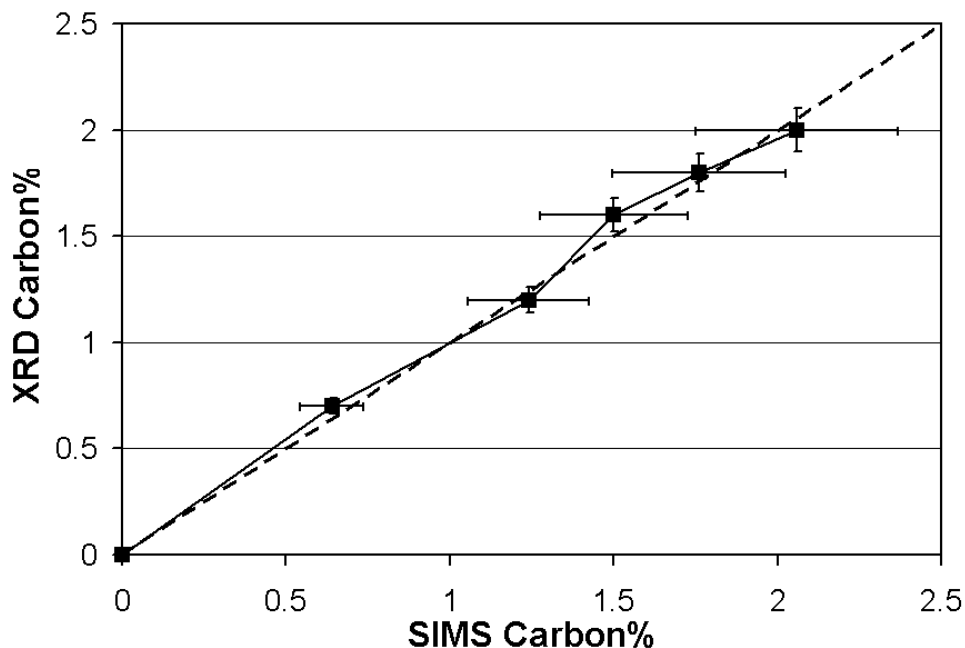


Figure 5.13. Comparison of substitutional carbon percentage measured from XRD vs. total carbon percentage determined by SIMS, for samples grown with methylsilane and disilane. Relative error bars of 5% and 15% were used for the XRD and SIMS measurements respectively. The dotted line represents fully substitutional carbon.

From the figure above, we can infer that fully substitutional carbon can be grown with disilane and methylsilane at 575 °C and 6 torr, for carbon percentages up to 2.0% carbon. The growth rates of the Si:C alloy layers grown with disilane and methylsilane (~6 nm/min) are less than the growth rates with NPS and methylsilane (20 nm/min). Why the sample with 2.0% carbon is fully substitutional but has a poor x-ray diffraction curve is not known.

5.5.2 Oxygen in Si:C Epitaxial Layers Grown with Disilane and Methylsilane

The oxygen incorporated in Si:C alloy layers grown with disilane and methylsilane was compared with the Si:C alloy layers grown with NPS and methylsilane. Neither the disilane (10% in hydrogen) nor the methylsilane (5% in hydrogen) gas sources went through any purification. The gas sources are both supplied by Voltaix. Based on Voltaix gas specifications, the disilane gas source has an argon and oxygen impurity level of 1 ppmv. The methylsilane gas source has argon and oxygen impurity level of 2 ppmv and a carbon dioxide impurity level of 10 ppmv. The water impurity level was not reported. The methylsilane and disilane source gases are diluted in 5N hydrogen (99.999% purity level). The carrier hydrogen gas used is 6N hydrogen (99.9999% purity level).

Similar to the NPS/methylsilane (section 5.4.3), the cause of the oxygen in the Si:C layers can be divided up into three components, oxygen contributions due to disilane, methylsilane, and a surface effect due to carbon on the silicon surface. The oxygen concentration coming from the disilane was determined by the average of several SIMS analysis and found to be at the SIMS background resolution of roughly $3 \times 10^{17} / \text{cm}^3$. A similar disilane partial pressure (~19 mtorr) was used in the growth of all Si:C alloy layers with disilane and MMS. We make the assumption that the oxygen background in the Si:C alloy layers is due to the MMS source and a surface effect related to carbon, and that the contribution from the oxygen in the disilane gas source is insignificant. We again make the assumption that the adsorption rate (A_{Oxygen}) is equivalent to the incorporation rate, which is the oxygen concentration times the growth rate. The oxygen adsorption rate and the MMS partial pressure are plotted in Figure 5.14 and summarized in Table 5.6 below.

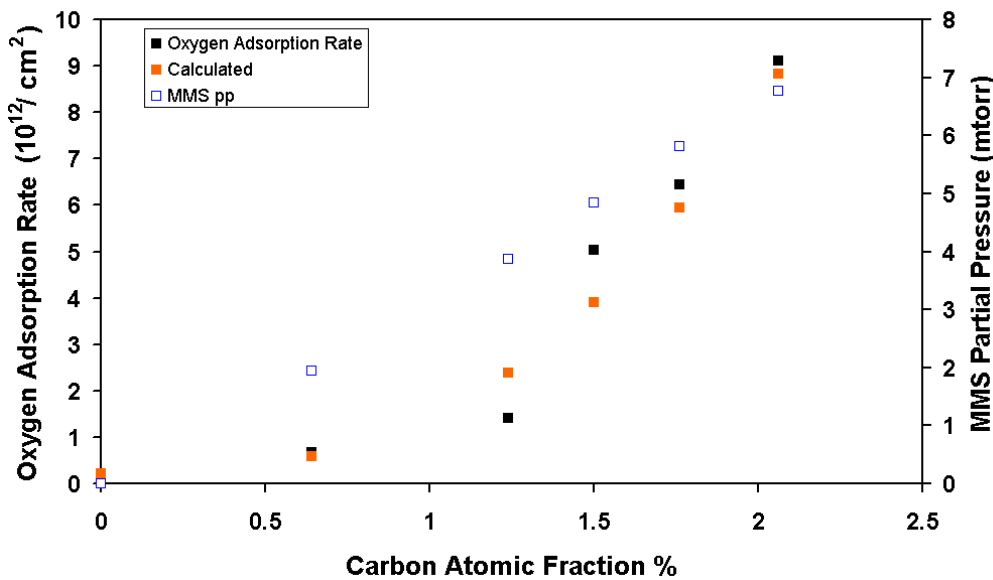


Figure 5.14. Oxygen adsorption rate (black solid squares) is plotted vs. carbon atomic percentage. The calculated oxygen adsorption rate (orange solid squares) is also plotted. The MMS partial pressure (blue open squares) is plotted on the secondary y-axis. All samples were grown at 575 °C and 6 torr, with 3 slpm hydrogen carrier and 10 sccm disilane flow.

Table 5.6. Summary of growth conditions and total carbon fraction of Si:C alloys grown with disilane (DS) and methylsilane (MS) as the silicon and carbon sources respectively at a chamber pressure of 6 torr and a temperature of 575 °C. The growth rate and oxygen concentrations are determined by SIMS analysis. The oxygen contributions from disilane, methylsilane, and the surface were calculated using the method described in the text above.

Sample	H ₂ flow (sccm)	Si ₂ H ₆ flow (sccm)	MMS flow (sccm)	H ₂ pp (mtorr)	Si ₂ H ₆ pp (mtorr)	MMS pp (mtorr)	GR (nm/min)	C %	O ₂ (10^{18} cm^{-3})	A _{Oxygen} ($10^{12}/\text{s}$)
Average	3090	10	0	5980.6	19.4	0	7	0	0.3	0.21
4845 4679	3109	10	1	5978.9	19.2	1.9	6.7	0.64	1.0	0.67
4845 4676	3128	10	2	5977	19.1	3.9	5.8	1.24	2.4	1.41
4943 4680	3137.5	10	2.5	5976.2	19	4.8	5.6	1.5	9.0	5.04
4845 4679	3147	10	3	5975.2	19	5.8	5.5	1.76	11.7	6.44
4943 4687	3156.5	10	3.5	5974.3	18.9	6.8	4.8	2.06	19.1	9.12

As shown in Figure 5.14 we observe a trend of increasing oxygen concentration along with increasing carbon atomic percentage, similar to that observed with NPS and methylsilane. We find that the oxygen adsorption rate is increasing faster than linear

while the MMS partial pressure is increasing linearly. We use Equation 5.3, and set the oxygen contribution from disilane to zero and assume that the oxygen contribution from the silicon site is small compared to that from the carbon site. We rewrite Equation 5.3 as Equation 5.4 below:

$$\begin{aligned} \text{Eq. 5.4} \quad O_{Total} &= (1-y)[O_{Si_{1-y}}(DS) + O_{Si_{1-y}}(MMS)] + k^n * y * [O_{C_y}(DS) + O_{C_y}(MMS)] \\ &\Rightarrow O_{Total} = k^n * y * [O_{C_y}(MMS)] \end{aligned}$$

We plot the calculated oxygen adsorption rate using a scaling factor, k^n of $4 \times 10^{11}/(\text{cm}^2 * \text{mtorr})$ with order 1.6. We do not understand the physics behind this result or whether 1.6 is the correct order. We find that the calculated result (plotted in Figure 5.14 above) is within error bars of the actual oxygen adsorption rate. The calculated oxygen adsorption rate is done to illustrate that there is a effect of carbon atoms on the surface that is increasing the oxygen adsorption rate. We do not understand why carbon increases the oxygen adsorption rate. One possibility is that the carbon-oxygen bond is stronger than the silicon-oxygen bond. Another possibility is that the surface becomes more disordered (i.e. loses its 2x1 reconstruction, similar to limited epitaxy thickness), allowing for an increase in oxygen adsorption onto the surface. We find that the oxygen adsorption rates in Si:C alloy layers grown with NPS and MMS and the oxygen adsorption rates in Si:C alloy layers grown with disilane and MMS are all on the order of $10^{12} / \text{cm}^2$, in spite of much higher impurity levels in the NPS and MMS. This suggests that the amount of carbon on the surface is different for the two higher-order silanes (i.e. a different amount of carbon is incorporated and segregated back to the surface).

5.6 Si:C Alloy Epitaxial Layers Grown with NPS and Methylchloride

Si:C alloy epitaxy growth was also investigated upon using methylchloride (also known as chloromethane, CH_3Cl) as the carbon source. The reason we tried methylchloride was that it might be easier to achieve selective Si:C epitaxy, due to the chlorinated chemistry of methylchloride. The results are shown in Figure 5.15 below and summarized in Table 5.7:

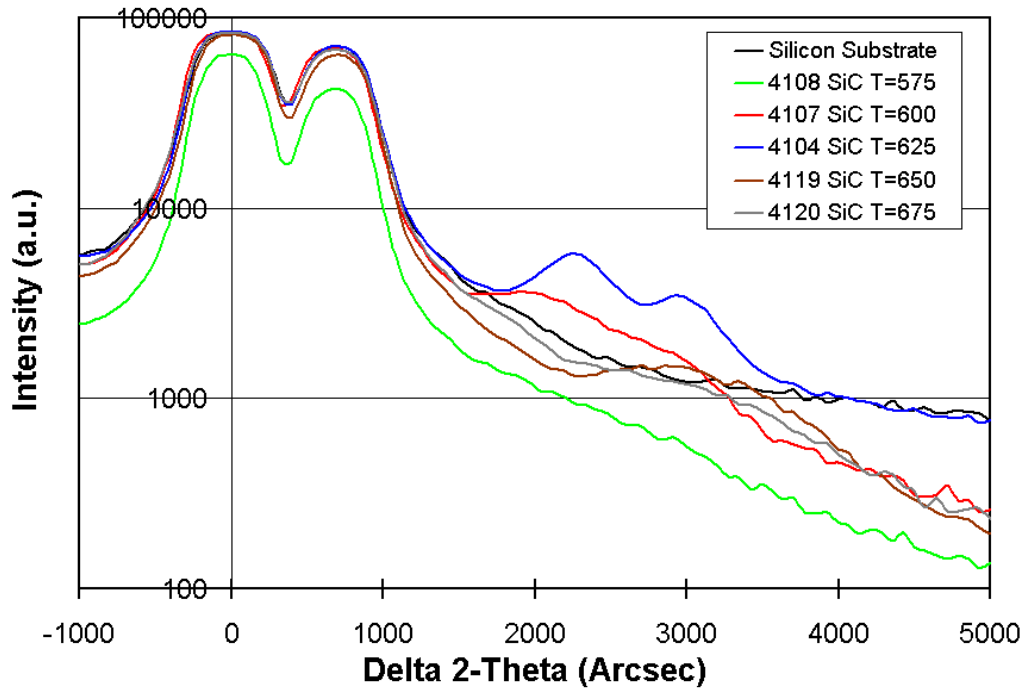


Figure 5.15. XRD rocking curves of various Si:C alloys grown at different temperatures using NPS and methylchloride as the silicon and carbon sources respectively. The NPS flow was 100 sccm and the methylchloride flow was 15 sccm. The temperatures were varied from 575 °C to 675 °C in 25 °C increments. The target growth thickness of the Si:C epitaxial layers is 100 nm.

Table 5.7. Summary of Si:C alloys grown with NPS and methylchloride as the silicon and carbon sources respectively

Growth Temperature	Carbon % (XRD)	Hydrogen (sccm)	NPS (sccm)	Methylchloride (sccm)	Growth Rate (nm/min)
575	?	3000	100	15	8
600	1.2	3000	100	15	14
625	1.35	3000	100	15	25
650	1.7	3000	100	15	50
675	1.85	3000	100	15	100

Using methylchloride and NPS, there was no peak related to $\text{Si}_{1-y}\text{C}_y$ observed for layers grown at 575 °C. There is a small and broad carbon peak at 600 °C. The peak observed at 600 °C is well resolved and right of the peak observed at 625 °C. Increasing the temperature to 650 °C peak shifts to the right again, indicating a higher carbon fraction. A very broad carbon peak is observed for growth of $\text{Si}_{1-y}\text{C}_y$ layers at 675 °C. Comparing peak intensities we observe that the intensity increases from 600 °C to 625 °C, and then decreases subsequently by increasing the temperature. The latter decrease in intensity going from 625 °C and upward could be attributed to the fact that the carbon may not be fully substitutional and the layers were degraded. The fact that the 600 °C intensity is not as high as the 625 °C intensity was surprising. It is possible that the methylchloride molecule was not cracking sufficiently at the lower temperatures, and therefore inhibited the growing surface, leading to thinner layers. The thinner Si:C layers may not have been resolved by the XRD scans. In conclusion, there exists only a small growth window for Si:C using methylchloride as the carbon source. At low temperatures we may not be able to incorporate carbon as the molecule may not be cracking; at high temperatures we may be unable to incorporate the carbon without degrading the epitaxial layers. We conclude that methylchloride is not a good source for the growth of $\text{Si}_{1-x}\text{C}_x$ layers.

5.7 Summary

The technique for the incorporation of $\text{Si}_{1-y}\text{C}_y$ alloys with dilute carbon fractions in silicon epitaxial layers are discussed in this chapter. X-ray diffraction and Vegard's law was used to determine the substitutional amount of carbon. High quality $\text{Si}_{1-y}\text{C}_y$ alloys layers were achieved using a neopentasilane as silicon source with methylsilane. Very high growth rates of $\text{Si}_{1-y}\text{C}_y$ alloys of 18nm/min and 13nm/min for fully substitutional carbon levels of 1.8% and 2.1%, respectively, were achieved. The highest substitutional carbon level achieved was 2.65% (strained perpendicular lattice constant of 5.347Å) as determined by X-ray diffraction. Si:C alloys were grown using two different silicon sources (NPS and disilane) and two different carbon sources (methylsilane and methylchloride). Oxygen levels in Si:C epitaxy layers are examined. The primary cause of the oxygen background appears to be coming from the methylsilane source, although a part of it may be due to a surface effect related to carbon. Based on background oxygen levels, our data suggests that high growth rates, lower temperatures, and cleaner methylsilane and silicon sources are desirable for Si:C epitaxy layers with reduced oxygen concentrations.

Chapter 6

Low Temperature In-Situ Surface Cleaning by Etching of Silicon, and Selective Silicon and Silicon-Germanium Epitaxy

6.1 Introduction to Low Temperature In-Situ Surface Cleaning

In order to have good quality epitaxy, the starting surface must be free of surface contaminants. It is quite difficult to begin with a silicon surface that is free of impurities. After any chemical cleaning before growth the silicon wafer must first be transferred from the air into the reactor chamber. The chemicals and water may have impurities. The air is also filled with unwanted impurities that can adhere to the surface of the wafer, such as moisture, oxygen, and carbon.

To remove these impurities, thermal baking in hydrogen at high temperatures ($T > 1000^{\circ}\text{C}$) was conventionally used in CVD for in-situ cleaning. Oxygen on the silicon surface is desorbed via the following reaction: [6.1]

Eq. 6.1

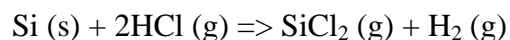


An HF dip to remove the native oxide and passivate the surface with hydrogen has been shown to significantly reduce the oxygen and carbon at the interface between a silicon substrate and epitaxial layer [6.2]. However, there are still trace amounts of these contaminants on the surface ($\sim 10^{13} \text{ cm}^{-2}$) [6.3]. Thermal baking in hydrogen at temperatures of around 750-800 °C were still necessary to remove these remaining trace contaminants [6.4][6.5]. With novel source gases such as trisilane and neopentasilane, reasonable epitaxy growth rates at low temperature have been achieved. However, cleaning steps still require a temperature greater than 750 °C, limiting the thermal budget of the growth process. In this chapter we will examine a novel surface cleaning technique: etching of the top silicon (or SiGe) surface layer with chlorine, which should remove the unwanted impurities from the surface.

6.2 In-situ Silicon Etchants

Thermal etching of silicon in-situ in epitaxial reactors is typically done using hydrogen chloride (HCl) in a hydrogen ambient at temperatures above 800 °C. For temperatures less than 750 °C, the etch rates with HCl have been observed to be less than 1nm/min [6.6]. (It has been shown however, that SiGe surfaces can be etched with HCl at temperatures of 625 °C [6.6]. This is believed to be due to the enhanced desorption of hydrogen from SiGe surfaces, which allows for the adsorption of the HCl) The mechanism by which silicon is etched by HCl is given in Equation 6.2 below:

Eq. 6.2



Previously attempts have been made to use chlorine instead of hydrogen chloride to etch silicon in a hydrogen ambient [6.7]. It was observed that the etch rate was still negligible

below 750 °C. The authors believed that the hydrogen carrier gas was reacting with the chlorine to form HCl, inhibiting any improvement of etch rates from using Cl₂ as the etchant.

Our silicon etching experiments were done using a flow of 15 sccm of chlorine gas with a flow of 3 slpm of hydrogen gas, set at a chamber pressure of 6 torr with varied temperatures. Etch rate experiments were done on silicon wafers with patterned silicon dioxide. The etch rate was determined by step height measurements between the silicon and the silicon dioxide surface patterns. The etch rate of the silicon dioxide was found to be negligible for the temperature range of 500 °C – 1000 °C (measured to be less than 10⁻² nm/min). At high temperatures 900 °C and 1000 °C, the silicon etch rates were 35nm/min and 220nm/min respectively. Negligible etch rates (less than 0.1 nm/min) of silicon using chlorine in hydrogen at 575 °C and 600 °C were observed in our lab consistent with other authors [6.7]. The etch rates of HCl and Cl₂ in hydrogen are plotted in Figure 6.1 below. From Figure 6.1 below, we can observe that etching with chlorine in a hydrogen ambient offers little improvement over etching with HCl in hydrogen.

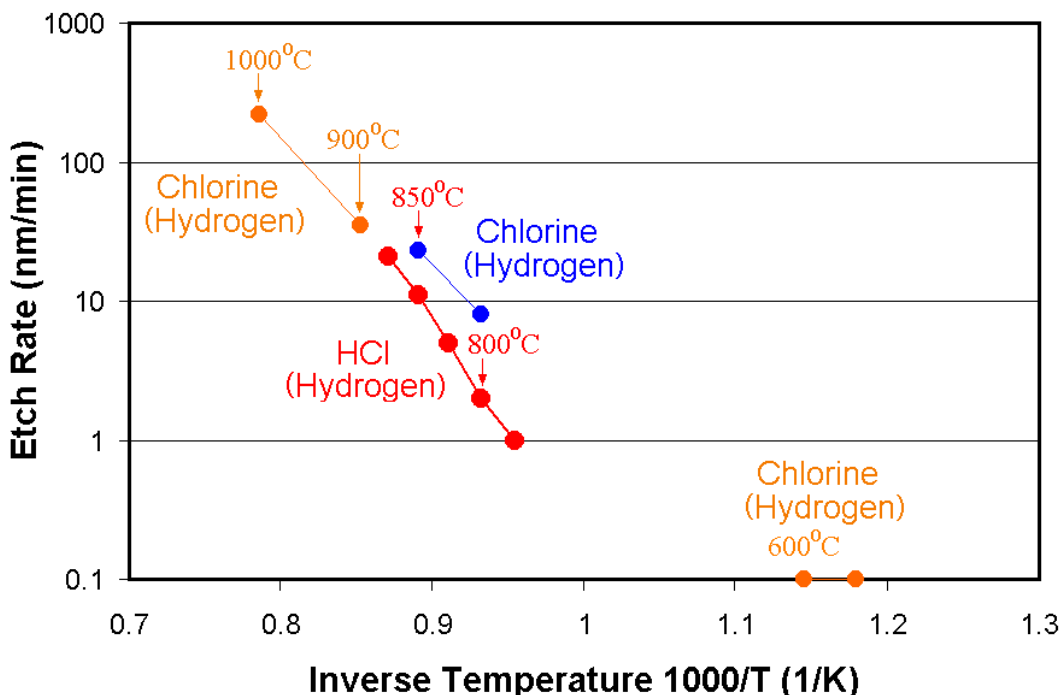


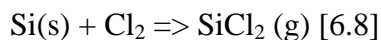
Figure 6.1. Etch rates of chlorine and HCl in hydrogen ambient. The chlorine in hydrogen (orange) data is from experiments conducted in our lab at a chamber pressure of 6 torr, with a flow of 15 sccm of chlorine gas and a flow of 3slpm of nitrogen gas. At 600 °C, the etch rate was less than 0.1 nm/min. HCl data is from reference 6.6 and the chlorine in hydrogen (blue) is from reference 6.7.

6.3 Silicon Etching with Chlorine in a Nitrogen Ambient

6.3.1 Etch Rates

To prevent chlorine from reacting with hydrogen, we used a nitrogen ambient instead of a hydrogen ambient for the thermal etching of silicon with chlorine. The surface reaction by which chlorine etches silicon is given by the following Equation 6.3:

Eq. 6.3



A partial pressure of 6 torr of nitrogen and 30 mtorr of chlorine was used in our experiments. Etch rates of 11nm/min, 5nm/min, and 1nm/min were achieved at 575 °C, 550 °C, and 525 °C respectively. The etch rates are plotted versus temperature in Figure 6.2 below.

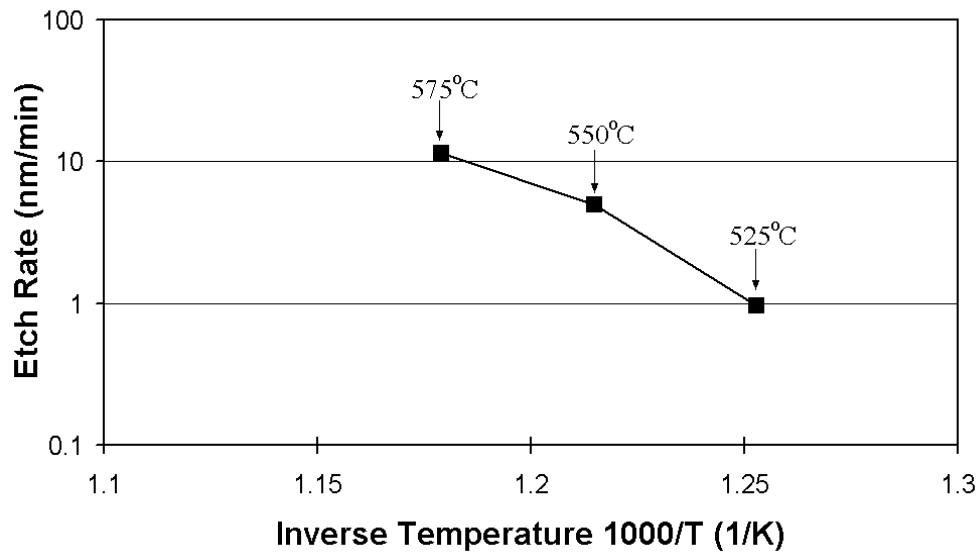


Figure 6.2. Chlorine etch rates (nm/min) vs. inverse temperature. The etch rates are measured by step height measurements. The chamber pressure is set to 6 torr, with 3 slpm of nitrogen carrier flow and 15 sccm Cl₂ gas flow.

Using an etch temperature of 575 °C, the etch rate was measured as a function of chlorine flow rates while holding the nitrogen flow and chamber pressure constant at 3 slpm and 6 torr respectively. The results are plotted in Figure 6.3 below.

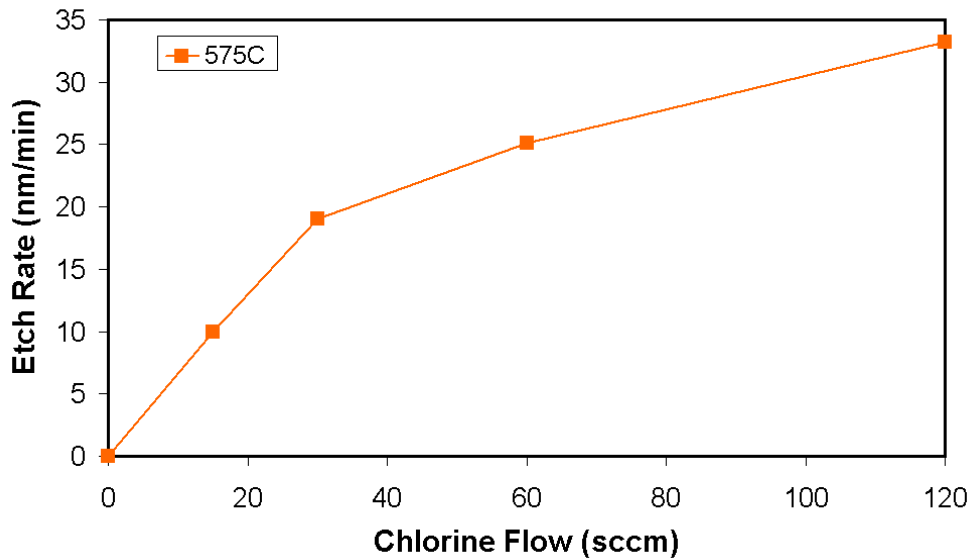


Figure 6.3. Silicon etch rates versus chlorine flow in nitrogen ambient at 575 °C and 6 torr chamber pressure.

The etch rate first increases linearly with the chlorine flow, and then increases at a slower rate. The rate is still increasing with the flow rate at 120 sccm, indicating that even faster etch rates may still be achievable. We would like to note that the chlorine etch rate (10-30 nm/min) in nitrogen can exceed the growth rates of silicon using both NPS and trisilane at 575 °C [6.9][6.10]. This is important for further selective epitaxy applications where the ability to etch away a nucleated surface layer on oxide is vital.

6.3.2 Surface Roughness After Etching

Smooth surfaces are desirable prior to the start of epitaxy. Surface roughness leads to the deterioration in the breakdown voltage of gate oxides [6.11]. Impurities on the surface need to be removed without roughening the surface. The surface roughnesses of the etched silicon surfaces were examined using AFM. The results are shown in Figure 6.4 below:

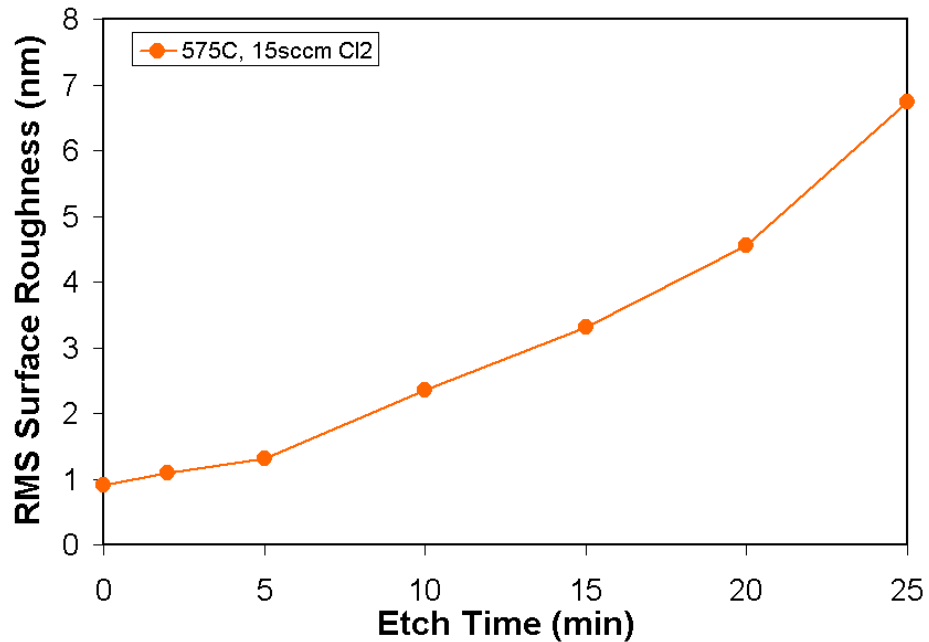


Figure 6.4. RMS surface roughness versus etch time using 15 sccm of chlorine gas in nitrogen ambient at 575 °C and 6 torr chamber pressure.

As the surface being etched, surface roughness increases over time. To keep the roughness under ~ 1nm RMS, only small etch times (< 2 minutes) can be used in order to minimize surface roughening. The AFM scan of a sample etched for 2 min with 1nm RMS roughness is shown in Figure 6.5 below:

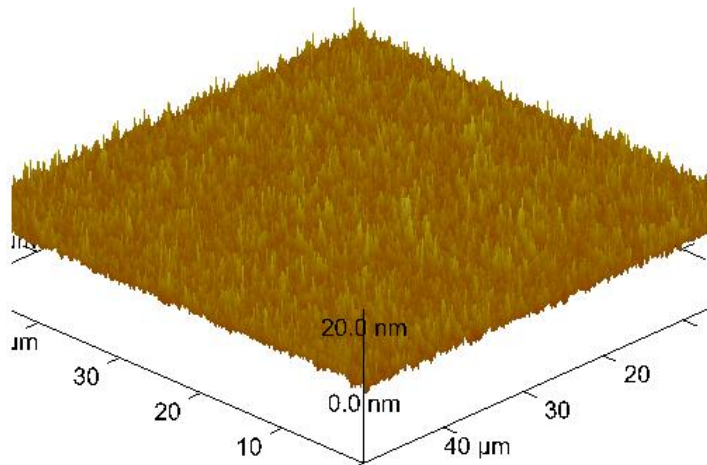


Figure 6.5. AFM image of silicon surface after etching of 20nm of silicon at 575 °C and a pressure of 6 torr with a flow of 15 sccm of chlorine. RMS surface roughness is ~ 1nm

6.4 Silicon Surface Cleaning by Etching

6.4.1 Oxygen and Carbon Impurity Removal via Etching

The effectiveness of the chlorine etching for cleaning a silicon surface prior to epitaxy was examined. SIMS was done to compare the interface impurity concentration after silicon epitaxy that had no in-situ clean step with that after epitaxy that had a 575 °C chlorine etch step. Prior to silicon growth in both steps, the sample was cleaned with a conventional ex-situ wet clean of H₂SO₄/H₂O₂ and a dilute HF dip [6.4]. The silicon epitaxial layer was grown in this experiment at 700 °C at 6 torr chamber pressure using dichlorosilane (DCS) as the silicon source. A 2.5-nm boron doping marker was used to indicate the start of silicon epitaxy in both cases. Both experiments were performed on a single wafer so data could be obtained with a single SIMS measurement. After the first wet cleaning the sample was loaded into the reactor in a hydrogen environment. The temperature was raised to 700 °C and approximately 150 nm of silicon was grown, without any cleaning steps such as an intentional hydrogen bake. (The wafer was at 700 °C for about 15 seconds before the DCS was turned on to start the growth.) The wafer was then taken out of the reactor and exposed to air for 12 hours. Now the sample was chemically cleaned again as described earlier. After loading the sample was then heated to 575 °C in hydrogen ambient, using a hydrogen flow of 3 slpm. The hydrogen was then turned off and nitrogen was turned on to the same flow rate. Then using a flow of 15 sccm of chlorine with a flow of 3 slpm of nitrogen gas at 575 °C and 6 torr, we etched off approximately 20 nm of silicon prior to the start of epitaxial growth. After etching, the ambient was switched back to hydrogen, the temperature was then raised from 575 °C to 700 °C and 50 nm of silicon was grown. From the SIMS shown in Figure 6.6, we observed an interfacial spike in both oxygen and carbon levels for the growth with no

cleaning step and no interfacial oxygen above the SIMS background was visible in the case of the chlorine etching. The interfacial spike in the carbon level is also significantly smaller in the latter case.

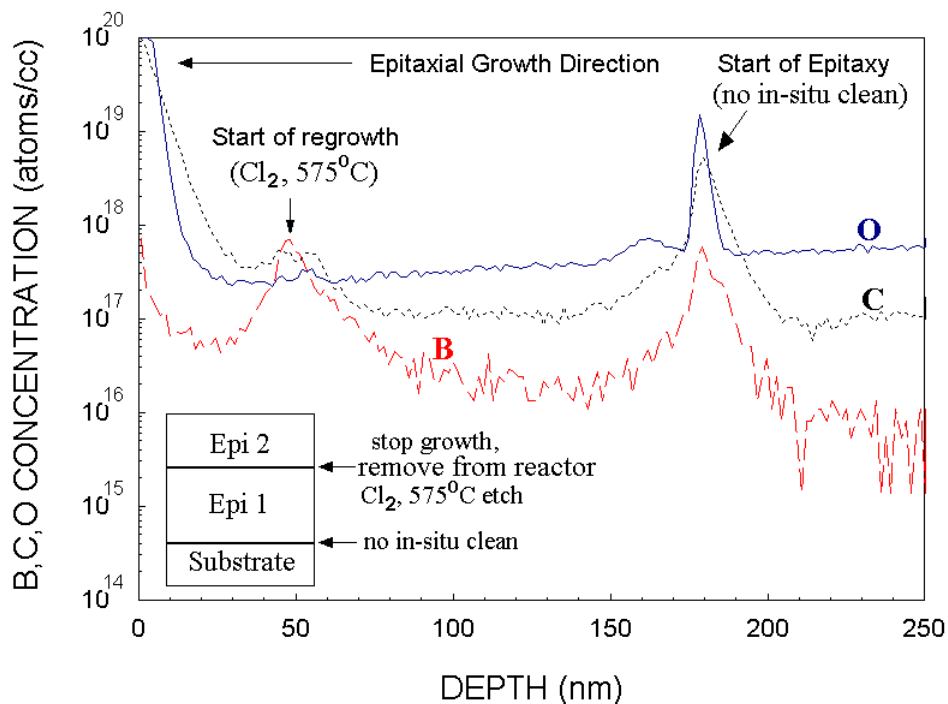


Figure 6.6. Secondary Ion Mass Spectrometry plotting depth versus impurity concentration for B (dashed), C (dotted), and O (solid). No in-situ cleaning was done at the start of epitaxy as indicated on the plot. After the first silicon epitaxy step, the wafer was removed from the reactor, exposed to air for 12 hours, and reloaded after wet cleaning again. 20nm of silicon was etched back using chlorine at 575 °C prior to the second epitaxial step. No oxygen spike and a clear reduction of carbon impurities demonstrate the effectiveness of chlorine in cleaning silicon surfaces. The inset depicts the structure of the sample.

The carbon and oxygen levels were integrated at both growth interfaces and the results are summarized in Table 6.1. There is more than an order of magnitude decrease of both surface oxygen and carbon after chlorine surface etching.

Table 6.1. Integrated carbon and oxygen levels for both the no in-situ clean and chlorine cleaning at 575 °C

In-Situ Clean	Integrated Oxygen Concentration	Integrated Carbon Concentration
None	8×10^{12} atoms/cm ²	3×10^{12} atoms/cm ²
575°C Cl ₂ etch	< 10^{11} atoms/cm ²	< 2×10^{11} atoms/cm ²

6.4.2 Phosphorus Impurity Removal via Etching

Experiments were done to test the ability of chlorine surface etching steps to remove other surface impurities, specifically phosphorus. Phosphorus as an impurity is extremely efficient at sticking on silicon surfaces and difficult to remove [6.12][6.13]. To remove phosphorus from the surface of silicon, high temperature thermal desorption is required [6.14]. Phosphorus is known to ride up onto the growing layer (surface segregation), leading to poor doping transitions when the phosphine source gas is turned off during silicon epitaxy. This effect is modeled in detail in chapter 7. We attempt to remove the surface phosphorus layers to avoid surface segregation effects.

To determine the effectiveness of the silicon etching in the removal of phosphorus, a thermal desorption step at 800 °C, a chlorine surface cleaning step by etching at 575 °C, and no in-situ cleaning were compared. Silicon was grown in this experiment at 700 °C at 6 torr chamber pressure using dichlorosilane (DCS) as the silicon source in hydrogen ambient. The growth was halted and a flow of 500 sccm of phosphine gas (100ppm phosphine in hydrogen) was injected into the chamber with 3 slpm hydrogen flow at a temperature of 700 °C at 6 torr chamber pressure for 5 minutes to coat the surface with phosphorus.

For the first cleaning step, we attempted to remove the phosphorus from the surface by etching with chlorine at 575 °C. Silicon was then grown and a thin SiGe layer was

then grown to reduce the surface concentration of phosphorus prior to the next phosphine dose, followed by a second phosphine exposure. (The SiGe is effective at gettering the surface phosphorous into the solid [6.15]) After the second phosphine dose, we attempted to remove the phosphorus via desorption by heating the surface to 800 °C for 10 minutes in 3 slpm hydrogen at 6 torr. Silicon was then grown followed by a thin SiGe layer to reduce the surface concentration of phosphorus prior to the next phosphine dose, followed by a final phosphine exposure. After the last phosphine dose, no cleaning step was performed and more silicon was grown. At no time was the chamber opened or the sample removed from the chamber during this experiment. A SIMS measurement of dopants and impurities vs. depth is shown in Figure 6.7.

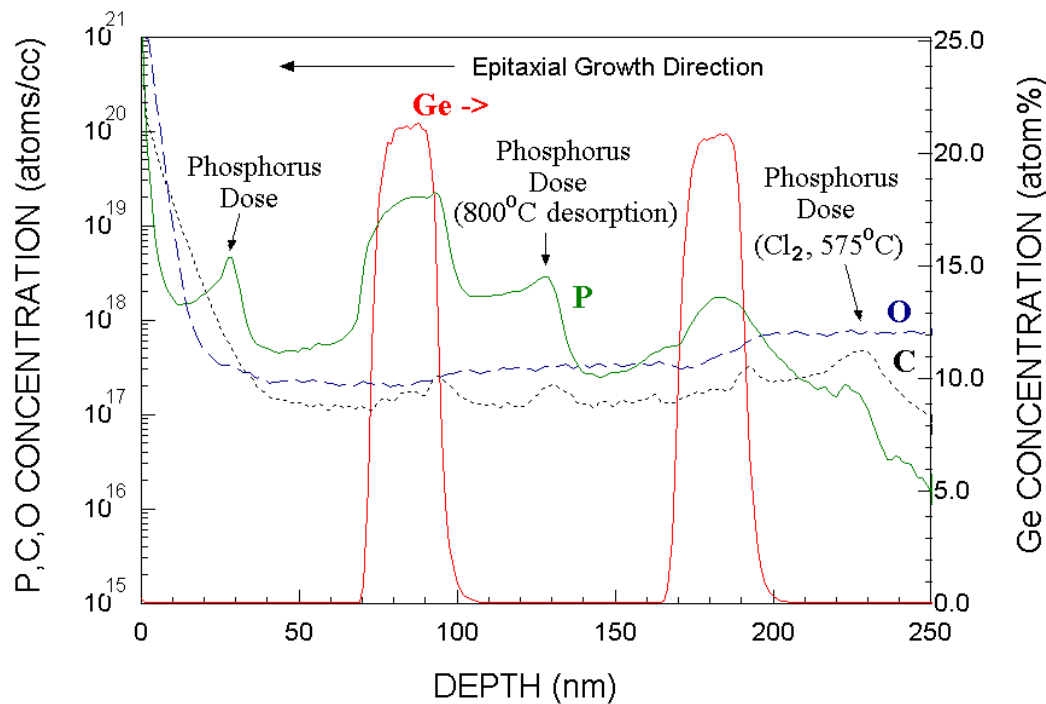


Figure 6.7. Secondary Ion Mass Spectrometry plotting depth versus impurity concentration for P (solid), C (dotted), and O (dashed). Growth was halted to cover the surface with phosphorus by injecting phosphine into the chamber at 3 different times during the growth. After the first two phosphine doses, different techniques were used to attempt to remove the phosphorus from the surface. SiGe layers were grown in between phosphorus doses to reduce the surface phosphorus concentration.

No phosphorus spike was observed at the interface treated with the chlorine etching step, indicating that chlorine etching removed all of the phosphorus from the surface prior to growth. A phosphorus spike at the growth interface after 800 °C thermal treatment was still observed showing that the treatment was less effective than the etching. The surface desorption of the remaining phosphorus led to a high concentration in the top SiGe layer. (The spreading of the phosphorus from the first SiGe layer into the substrate is possibly due to the annealing step at 800 °C). The last phosphorus spike, without any cleaning step, is used as the control for comparison. At each interface the phosphorus levels were integrated and are summarized in Table 6.2.

Table 6.2: Integrated phosphorus levels for no in-situ clean, chlorine cleaning at 575 °C, and 800 °C desorption.

In-Situ Clean	Integrated Phosphorus Concentration
None	3×10^{12} atoms/cm ²
575°C Cl ₂	< 10^{11} atoms/cm ²
800°C desorption	2×10^{12} atoms/cm ²

No significant reduction in phosphorus concentration was observed from the 800 °C desorption technique, which produced a decrease from 3×10^{12} atoms/cm² to 2×10^{12} atoms/cm², while the Cl₂ etching step reduced the phosphorus concentration significantly from 3×10^{12} atoms/cm² to less than 10^{11} atoms/cm². This indicates that the chlorine etching of the silicon surface also etched away the phosphorus atoms that were adsorbed onto the surface. Note, however that in the first and second cases a large amount of phosphorus was gettered by the SiGe layer (2×10^{12} / cm² after the chlorine etch and 3×10^{13} / cm² after the 800 °C desorption step). In the first case the background phosphorus in the chamber accumulation was probably gettered by the SiGe. In the second case, a large surface concentration of phosphorus was incorporated into the SiGe layer from the phosphorus not removed by desorption at 800 °C.

6.5 Quality of Epitaxial Growth on Chlorine-Etched Surfaces

To characterize the epitaxial quality on layers grown after etching with chlorine, a Si/SiGe/Si quantum well structure was grown after chlorine etching in nitrogen for 2 minutes. The silicon layers were grown with DCS ($700\text{ }^{\circ}\text{C}$), and the SiGe layers were grown with DCS and germane ($625\text{ }^{\circ}\text{C}$) for both samples. The photoluminescence (PL) intensity of silicon is very sensitive to the rate of non-radiative recombination, and thus to the defect density. Photoluminescence measurements were taken comparing a reference Si/SiGe/Si quantum well with a $1000\text{ }^{\circ}\text{C}$ hydrogen thermal clean step before growth of the Si/SiGe/Si quantum well to one grown after chlorine etching without any thermal cleaning (Figure 6.8).

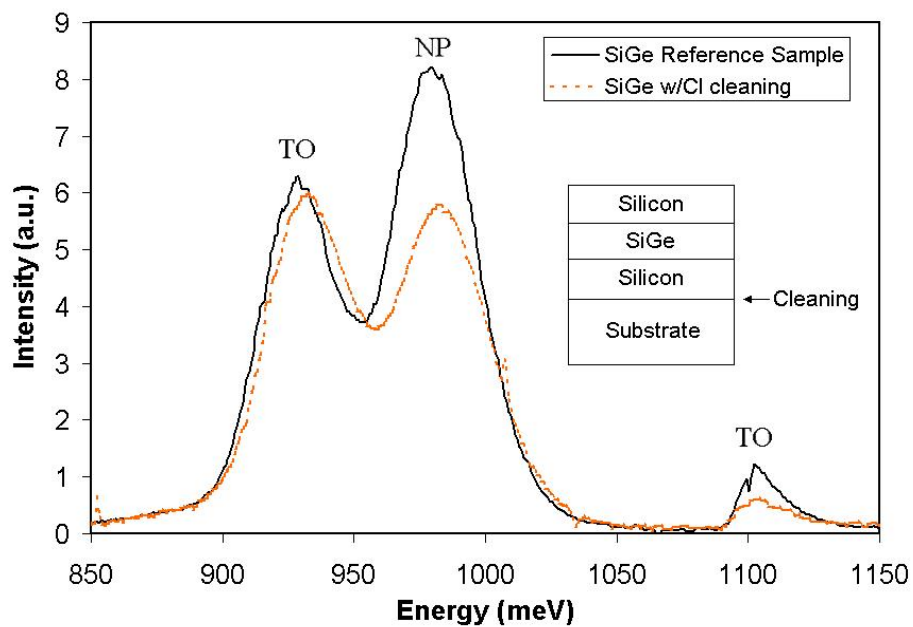


Figure 6.8. Photoluminescence intensity vs. photon energy at 77K . Indicated on the plot are the TO (transverse optical phonon replica) for Si and SiGe and the NP (no phonon) peaks for SiGe. Photoluminescence for a reference SiGe quantum well with a $1000\text{ }^{\circ}\text{C}$ bake in hydrogen instead of a Cl_2 etching step is compared with the structure with Cl_2 etching of the substrate.

The SiGe layers were grown after the chlorine etch step. If chlorine etching had a detrimental effect on the subsequent epitaxy, then all the layers after chlorine etching would be of a poor crystalline quality. The comparable photoluminescence intensities of SiGe and Si indicate high-quality defect-free silicon epitaxy growth on a chlorine-etched surface.

6.6 Selective Silicon-Germanium Epitaxy

6.6.1 Techniques for Achieving Selective Epitaxial Growth

Selective epitaxy is the growth on epitaxy on patterned substrates, where epitaxy growth occurs only on a crystalline silicon surface and does not grow on any other surface (typically an oxide or nitride surface). This technique used to achieve raised-source/drains and in certain epitaxial regrowth applications where only growth in certain regions is desired [6.16]. Silicon will often grow even on the oxide/nitride surface after a certain nucleation (incubation) period. The growth on a non-silicon surface (e.g. oxide) would be either polysilicon or amorphous silicon. Selective epitaxy can be achieved three different ways.

In the first (desired) case the nucleation period is long enough such that a selective layer can be grown only on the crystalline silicon region. This requires an extremely clean reactor system and high-vacuum conditions; unwanted surface contamination leads to nucleation sites, which will reduce the nucleation time [6.17].

In the second case a silicon etchant (typically HCl) as injected at the same time of growth. This technique achieves selective growth by either the prevention of a nucleation layer from forming or by extending the nucleation time so that enough selective epitaxy

is achieved. The mechanism is that the chlorine leads to some etching occurring simultaneous with growth. With chlorinated growth sources (such as DCS), often no extra chlorinated etch gases sources such HCl is required. The etchant reduced the growth rate.

The third case deposition /etch cycles are used. This technique is a cross between the first and second techniques and is illustrated in Figure 6.9 below:

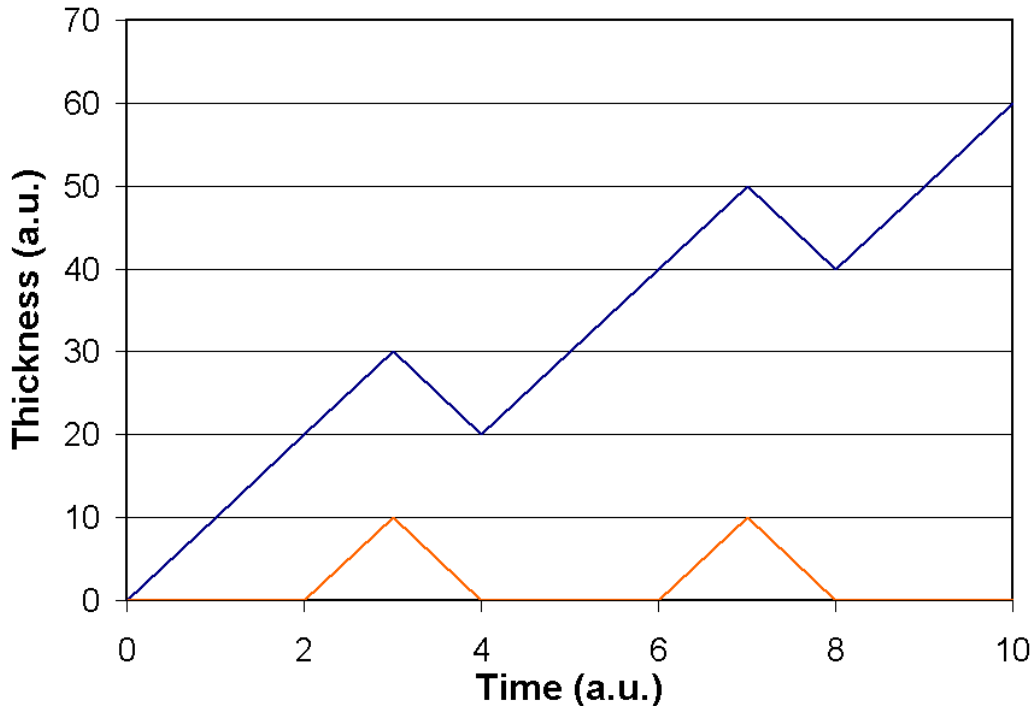


Figure 6.9. Growth thickness versus deposition time illustrating selective growth using deposition / etch cycles. The blue line is the net growth on a silicon surface and the orange line is the deposition on oxide.

Growth on both the silicon and on the oxide (arbitrary non-selective surface) occurs. However, the growth on the oxide (orange line in Figure 6.9) does not occur right away as it takes a certain amount of time (2 units in Figure 6.9) before a layer has nucleated. During the nucleation time, silicon is constantly deposited on the crystalline surface (blue). After the layer on oxide has grown a small amount (time at 3 units), the deposition

is halted and we proceed to etch both the crystalline silicon layer and the nucleation layer (time from 3 to 4). The oxide surface is then removed of all nuclei, and we then proceed to do deposition again. After each cycle the amount of “selective” epitaxy increases until the desired amount is achieved.

6.6.2 Nucleation Time for SiGe on Oxide-Patterned Wafers

We will attempt to achieve selective epitaxy of SiGe on silicon (100) wafers w/ patterned silicon dioxide using the deposition / etch cycle technique. The growth of SiGe was done at a chamber pressure of 6 torr and growth temperature of 625 °C. The growth was conducted in hydrogen ambient with hydrogen flow of 3 slpm. The flow of DCS was 26 sccm and the flow of germane was 100 sccm (0.8% germane in hydrogen). The growth rate (non-selective) is 6 nm/min and the germane fraction is 20%. The SiGe nucleation experiments were first conducted on patterned silicon wafers without the flow of the etchant HCl. The pattern comprised of 30 micron silicon stripes and 100 micron oxide stripes. The nucleation time was determined to be 12 minutes before any growth was detected on the oxide using reflectance spectroscopy (Nanospec using the poly on oxide program). A value of more than 10 Angstroms on the oxide was interpreted as deposition. We then attempted to grow SiGe on RIE (reactive ion etching) etched trenches 20 nm in width and 200nm apart and 55 nm in depth (Figure 6.10).

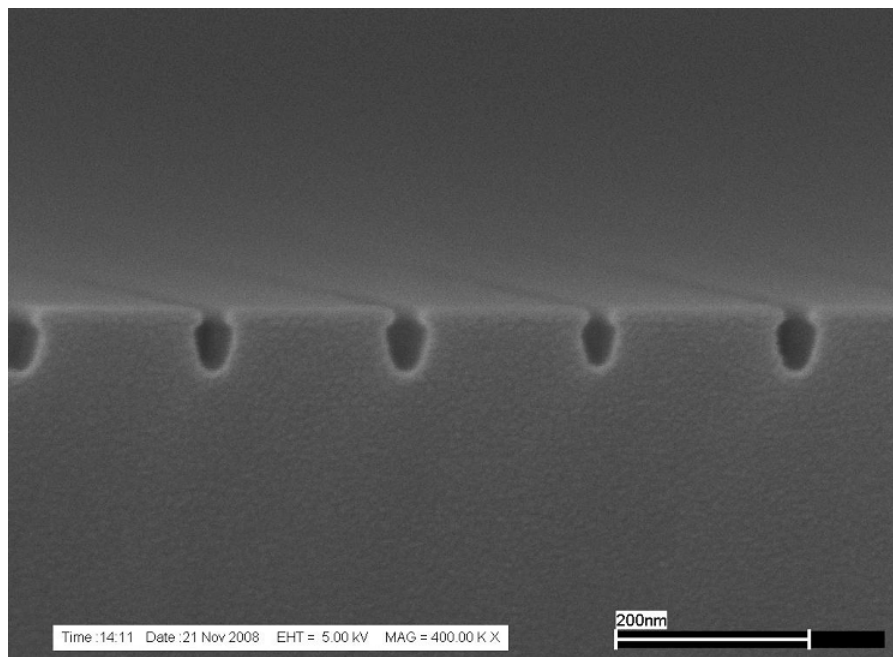


Figure 6.10. SEM image of 20 nm wide trenches patterned using nano-imprinting and etched by RIE, used for selective SiGe epitaxial experiments. (Courtesy of Chao Wang) Note that that is a very thin oxide layer (8 nm) as the pattern on the top silicon surface which was used as the etch mask for the trench etching in silicon. This layer is barely visible on the SEM.

Several nucleation time experiments of 10, 7 and 3 minutes were conducted on the trench-patterned samples. The results are shown in Figures 6.11a-c below.

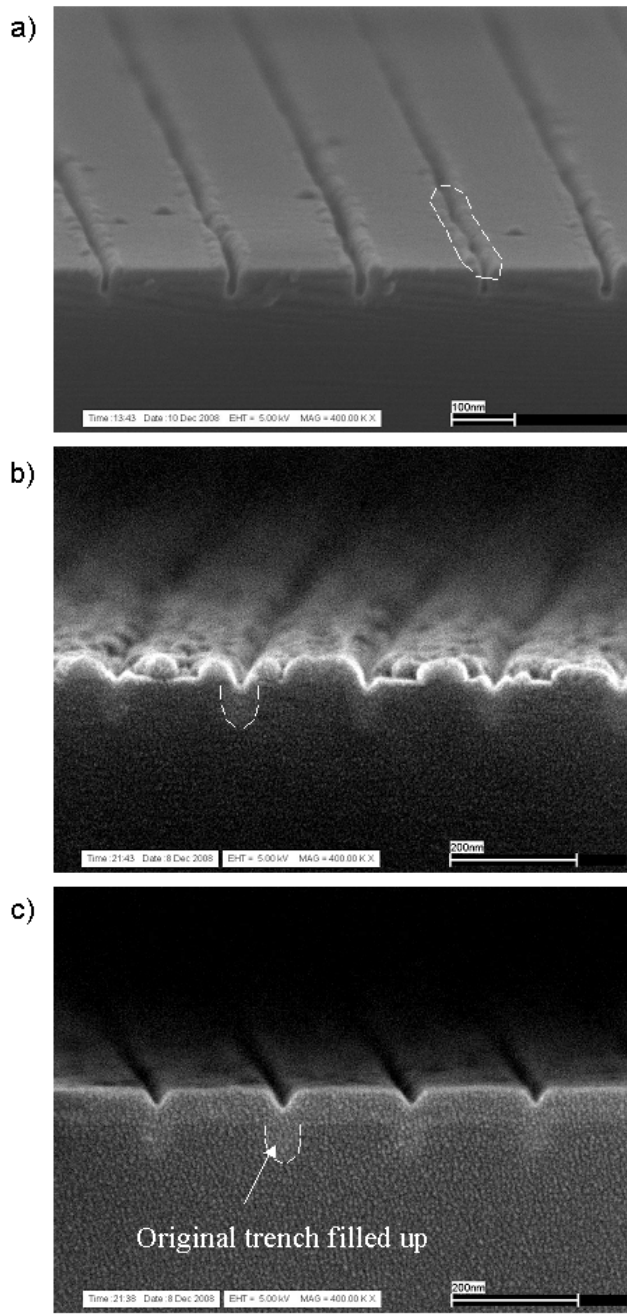


Figure 6.11a-c. SEM of a) 3 minute, b) 7 minute, c) 10 mintue, SiGe growth on RIE etched 20 nm wide trenches. We note the SiGe growth rate on the patterned sample is twice the non-selective (blanket) SiGe growth rate. The growth conditions are 6 torr chamber pressure, 625 °C, 3 slpm hydrogen, 26 sccm DCS and 100 sccm germane gas flows. The dotted circle in a) highlights the nucleation on the edges of the trench. The dotted white lines indicate the filled trench in b and c. SEM images courtesy of Chao Wang.

As shown in the three figures above, the nucleation time is approximately 3 minutes. We observe that nuclei begin at the edges of the trench starting at approximately 3 minutes. At the growth time is increased the nuclei coalesce, and is roughly 30 nm in height in Figure 6.11b after a growth time of 7 minutes. The nuclei then coalesce into a smooth layer after ten minutes of growth (Figure 6.11a).

To achieve selective epitaxial growth, we used the Cyclical Deposition and Etch (CDE) method of Figure 6.9. HCl was used as the etchant and HCl etch rates were taken from a paper [6.6]. It was shown that SiGe etch rates were much higher than the silicon etch rates using HCl, due to the enhanced desorption of hydrogen on a SiGe surface. This allowed for the use of HCl at low temperatures (< 700 °C) for the etching of SiGe surfaces. Conventionally, HCl is only used as an etchant for silicon surfaces at high temperatures ($T > 800$ °C).

We then proceeded the grow selective SiGe by growing for 3 minutes using the aforementioned recipe, and stop to etch for 5 minutes at 625 °C at 6 torr, with 3 slpm hydrogen and 90 sccm of HCl. Then another deposition step is done for three minutes followed by another 5 minute etch using HCl and hydrogen. The final growth was compared with the original etched trenches 20nm in width and 55 nm in depth, shown below in Figure 6.12a (original)& b (after selective SiGe growth). As shown in the Figure 6.12c by the dotted line, the original trench is now completely filled with SiGe epitaxy. No growth is observed on the regions with oxide, indicating that selective growth was achieved with using DCS, germane and HCl at 625 °C and 6 torr.

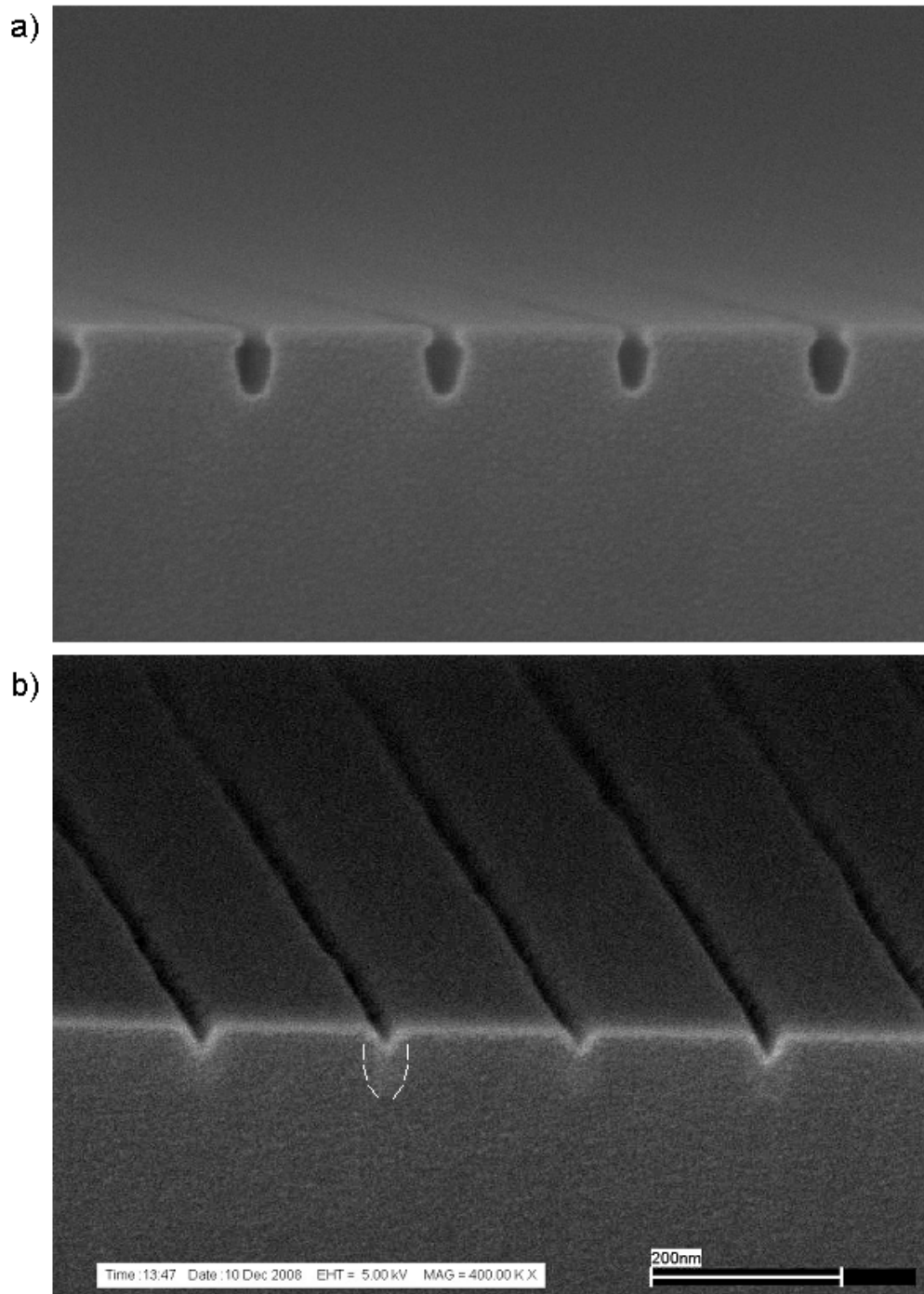


Figure 6.12. SEM of successful selective epitaxial SiGe growth on 20 nm wide trenches. The difference of the color of the trenches is due to the fact that they are SiGe whereas the rest of the sample is silicon. (Courtesy of Chao Wang)

6.7 Selective Epitaxial Growth of Silicon using NPS and HCl

Selective epitaxial growth was attempted with using NPS (50 sccm) and HCl (300sccm) in a continuous process at 600 °C and 6 torr with 3 slpm of hydrogen carrier gas. The silicon growth rate without HCl under the same conditions is 12 nm /min. The nucleation time of NPS with HCl was first determined, and estimated to be about 20 seconds. Without the HCl the nucleation time was estimated to be almost instantaneous (~0 secs). The result is shown in Figure 6.13 below:

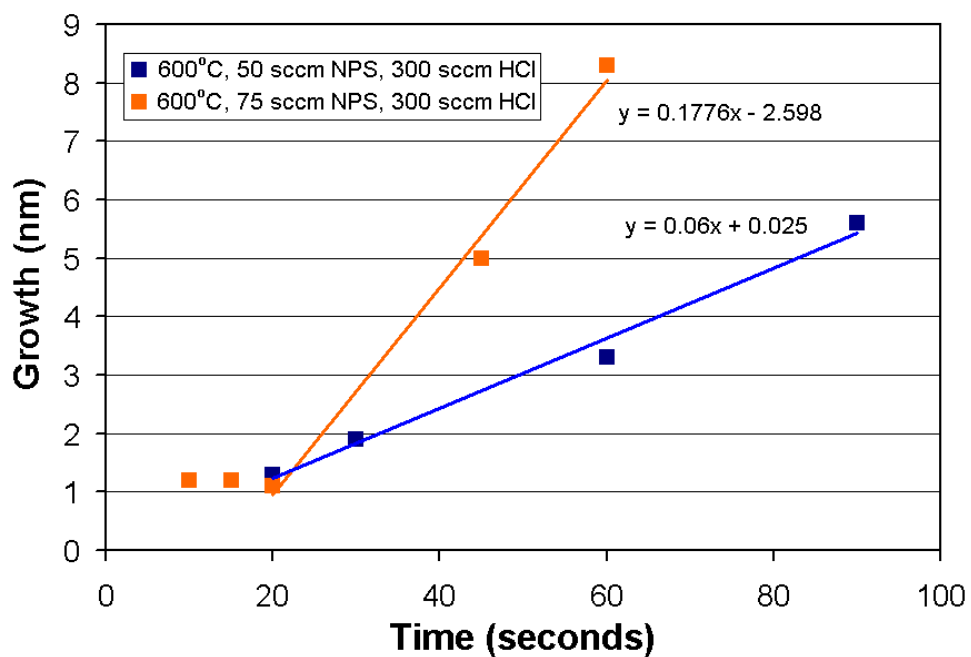


Figure 6.13. Nucleation time experiment with NPS and HCl. The growth on oxide (nm) versus the growth time was plotted for two different growth conditions. The growth conditions was 6 torr chamber pressure, at 6 torr, 3 slpm of hydrogen flow, with 300sccm of HCl flow with either 50 sccm of NPS (bubbler) flow (blue) or 75 sccm of NPS (bubbler) flow (orange).

The deposition on oxide was measured by reflectance spectrometry (Nanospec) using the “polysilicon on 100 nm oxide program” was used. 1 nm of the silicon growth on the oxide, is the lower limit of the “Nanospec” tool used. At 600 °C HCl does not etch away

silicon (section 6.2). When HCl is combined with NPS, there is a reduction of growth rate. This may be due to the fact that there are more open sites on the surface for adsorption during epitaxial growth with NPS, allowing for the adsorption of HCl onto the surface.

To etch away unwanted nuclei sites on the oxide the etch temperature was raised to 650 °C. Deposition was done with 50 sccm of hydrogen flow through the NPS bubbler with 300 sccm of HCl flow, then etch cycles of 300 sccm of HCl and 3 slpm of hydrogen carrier flow was done at 6 torr chamber pressure and 650 °C. A total of 30 deposition and etch cycles was done for 45 minutes of total time. The resulting deposition is shown in Figure 6.14 below:

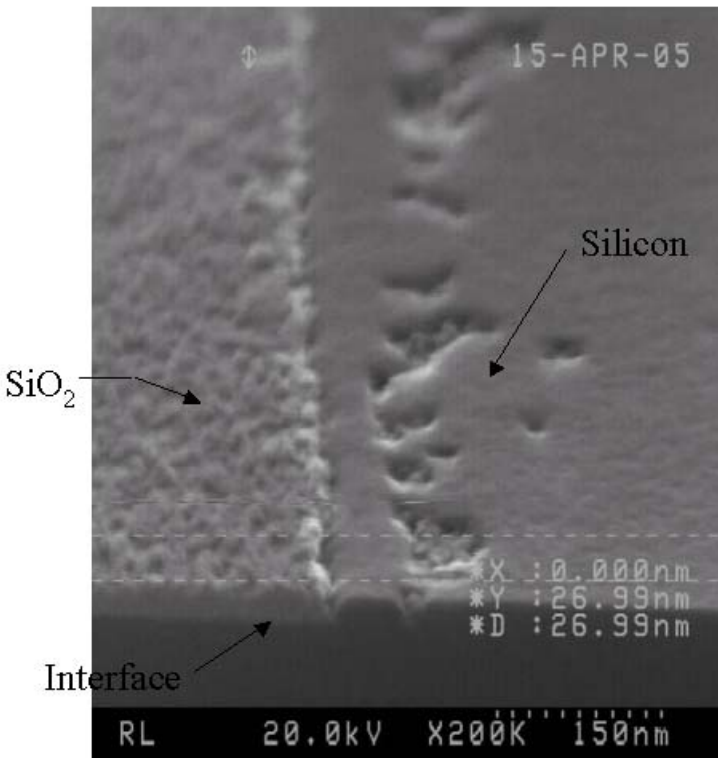


Figure 6.14. Selective growth on oxide done with deposition / etch cycles using NPS and HCl. The deposition was done at 600 °C, at 6 torr with 3 slpm of hydrogen, 50 sccm of hydrogen through the NPS bubbler, and 300 sccm of HCl. The etch cycle was done at 650 °C, at 6 torr, with 3 slpm hydrogen flow, and 300 sccm of HCl. The "Interface" labeled in the picture denotes the start of the silicon dioxide pattern on silicon.

The total growth of selective epitaxy was 12 nm. The growth rate was measured to be 0.27 nm / min. While selective growth was achieved with HCl and NPS, this method is not technologically attractive due to the low growth rate.

6.8 Summary

In this chapter, we have demonstrated the feasibility of low temperature in-situ silicon etching as an alternative to in-situ thermal cleaning of the silicon surface. The chlorine etch rates of silicon in nitrogen ambient are orders of magnitude higher than the etch rates using HCl or chlorine in a hydrogen ambient in the temperature range of 525 °C to 575 °C. This allowed for in-situ etching of silicon at low temperatures and silicon etch rate up to 35 nm / min was achieved at 575 °C. Silicon surface cleaning experiments via the etching of silicon via chlorine in a nitrogen ambient were conducted. This technique was shown to be capable of removing oxygen, carbon, and phosphorus from the surface. Conventionally, these impurities are removed only by thermal desorption at high temperatures ($T > 800$ °C). However, there is some difficulty using chlorine as long etch times (> 2 minutes) causes the roughening of the silicon surface. Selective growth techniques were explained in this chapter. Selective SiGe epitaxial growth was also achieved using DCS and germane along with HCl as the etchant in a hydrogen ambient. Selective growth of silicon using NPS and HCl was also achieved. However, the growth rate (0.27 nm/min) was too low for any practical application.

Chapter 7

Phenomenological Model of Phosphorus Incorporation of Silicon

7.1 Introduction

In this work, *in-situ* phosphorus doping of silicon epitaxy from 575 °C to 1100 °C by low-pressure rapid thermal chemical vapor deposition (RTCVD) in a cold-wall system, using phosphine (PH_3) as the phosphorus source and a variety of silicon sources (DCS, silane, disilane, NPS) are compared. In contrast to boron doping in silicon where high concentrations ($>10^{20} \text{ cm}^{-3}$) and sharp turn-on and turn-off profiles (5-10 nm/decade on both the leading and trailing edges) are obtained [7.1], high concentration n-type doping with an abrupt profile has always been difficult. It has been reported that high concentrations of phosphine doping can severely depress the growth rate [7.2][7.3] and that residual dopant in the chamber and phosphorus segregation [7.4][7.5] on the wafer surface can also cause an unintentional doping tail after the phosphorus gas is turned off. In this chapter we will formulate a phenomenological model of how phosphorus doping occurs and compare the phosphorus doping profiles among the aforementioned silicon precursors.

7.2 Phosphorus Background Concentration in Epitaxial Layers Grown with Dichlorosilane

7.2.1 Phosphorus Background from CV Measurements

A background concentration of phosphorus in the range of $10^{17} / \text{cm}^3$ is observed from SIMS measurements in samples grown with our CVD reactor using DCS as the silicon gas with no intentional doping in the temperature range of 700 °C to 1000 °C. We would like to determine how this background concentration changes with temperature and in a silicon germanium layer. Four different structures were grown at different temperatures and conditions were conducted on (100) oriented n-type (10-20 Ohm-cm) substrate silicon wafers. The chamber pressure was set to 6 torr with 3 slpm of hydrogen gas flow in all cases. A flow of 26 sccm of DCS was used in all silicon layers and 100 sccm of germane (0.8% in hydrogen) gas was used in the SiGe (22% Ge) layers. Schottky diodes were then fabricated to test the background concentration by sputtering aluminum through a shadow mask (circular patterns of 1 mm in radius). The cross sectional views of the four test structures are shown in Figure 7.1 below:

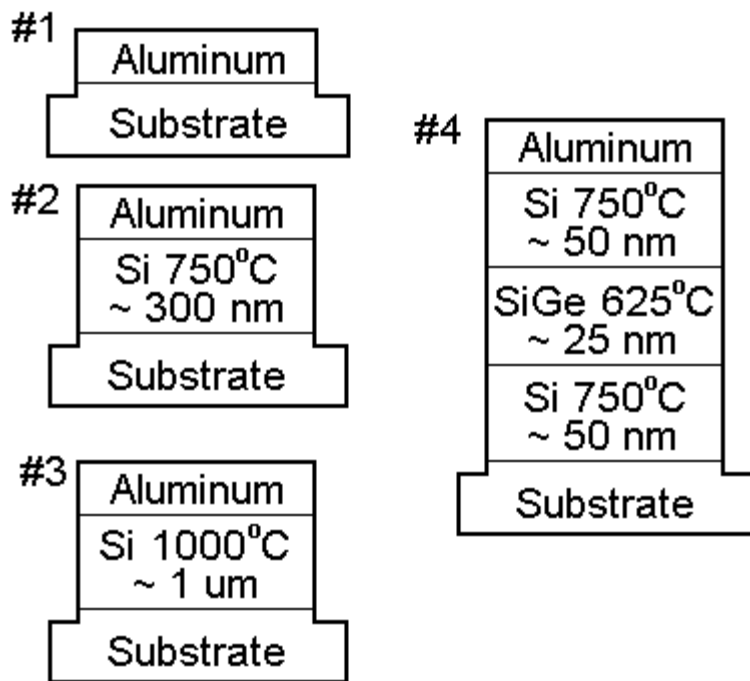


Figure 7.1. Cross sectional view of the four different Schottky diode structures used to determine the background phosphorus concentrations in undoped epitaxial layers grown using DCS in our RTCVD chamber at 6 torr with 3 slpm flow of hydrogen as the carrier gas. A second contact was added on the back of the substrate. Mesa etching was done but not necessary.

The first structure (#1 in Figure 7.1) is used as control sample to verify that the Schottky diodes were fabricated correctly (i.e. the resulting diode gave the correct substrate doping). The second and third samples were grown at 750 °C and 1000 °C respectively using DCS. A structure with a layer grown at our typical growth temperature of 700 °C was not used since the growth rate at 700 °C is 2.5 nm/min. At that growth rate the experiment was deemed too time and material consuming. The fourth structure was used to determine the background doping in a SiGe layer grown at 625 °C. The substrate background is n-type phosphorus doped with doping concentration of roughly $5 \times 10^{14} / \text{cm}^3$. The thickness on the layers in the four structures was chosen so that the depletion layer resulting from the Schottky diode would not deplete into the substrate.

We use these four structures to determine the dopant concentration by CV measurements. Capacitance voltage (CV) experiments were then conducted on the four structures. Using the three equations given below we determine the dopant concentration, N_D and the depletion width, X_d , based on our data from the CV measurements.

Eq. 7.1

$$C = \frac{\epsilon_{Si} A}{x_d}$$

Eq. 7.2

$$x_d = \sqrt{\frac{2\epsilon_{Si}(V_{bi} - V)}{qN_D}}$$

Eq. 7.3

$$\frac{1}{C^2} = \left(\frac{x_d}{\epsilon_{Si} A} \right)^2 = \frac{2(V_{bi} - V)}{A^2 \epsilon_{Si} q N_D}$$

C is the capacitance given in Farads, ϵ_{Si} is $11.7\epsilon_0$, the dielectric constant of silicon. ϵ_0 is 8.854×10^{-14} F cm $^{-1}$, the permittivity of vacuum. A is the area of the Schottky diode, $q = 1.602 \times 10^{-19}$ Coulombs, is the electron charge, V_{bi} is the built in voltage and V is voltage given in volts. We rewrite Equation 7.3 to isolate the dopant concentration N_D in Equation 7.4

Eq. 7.4

$$N_D = \frac{1}{q\epsilon_{Si} d \left(\frac{1}{C^2} \right) / d(-V)}$$

We plot $1/C^2$ vs. the voltage for three of our four structures. We were unable to resolve the SiGe layer from the silicon layers due to the small thickness, 25nm, of the SiGe layer. The data for the remaining three structures are shown in Figure 7.2 below.

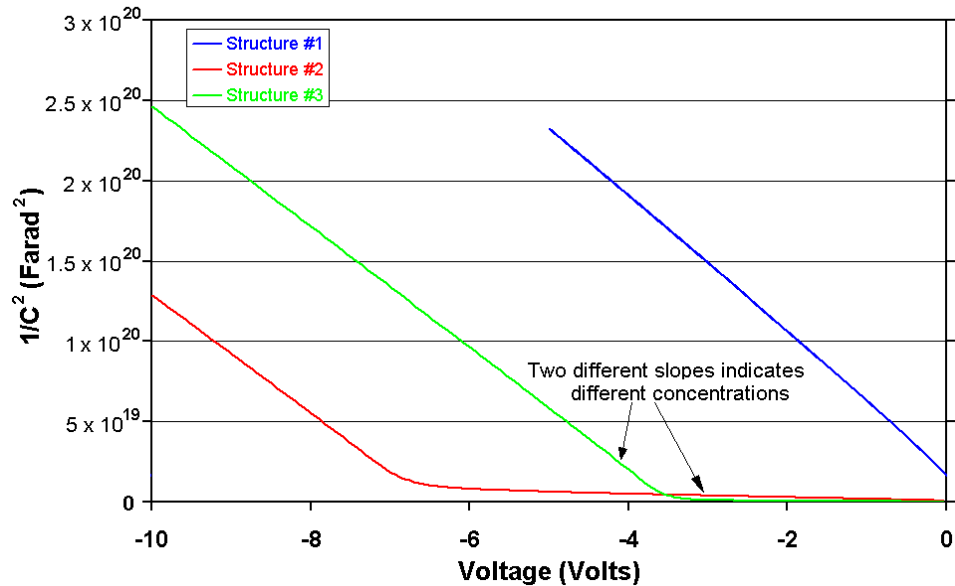


Figure 7.2. $1/C^2$ vs. voltage for the Schottky diodes fabricated for three structures in Figure 7.1 on top of an n-type substrates. The two different slopes indicate different doping concentrations.

From Figure 7.2 above, we find that in structures #2 and #3, there are two different slopes to the $1/C^2$ versus voltage plot. The slope is inversely proportional to the dopant concentration. All three structures have a portion of its $1/C^2$ curve with a similar slope. This is the n-type substrate layer of 10-20 ohm-cm. Two of the structures #2 and #3 have two different slopes, indicating that there are two layers with different dopant concentrations. This is expected; we know that the silicon layers grown with DCS are phosphorus-doped and slightly n-type. We re-plot Figure 7.2 plotting the dopant concentration versus the voltage in Figure 7.3 below. We now find that we can clearly see that there are two different silicon layers in structures #2 and #3. We mark the different layers based on the dopant concentration. The silicon layer grown at $1000\text{ }^\circ\text{C}$ has a dopant concentration of $\sim 10^{16} / \text{cm}^3$, and the silicon layer grown at $750\text{ }^\circ\text{C}$ has a dopant concentration of $\sim 4-5 \times 10^{16} / \text{cm}^3$. In Figure 7.4 the depletion width is plotted versus the dopant concentration. This is done to determine the thickness of the silicon

layers. We find that the thickness of the silicon layer grown at 1000 °C is roughly one micron thick, and the silicon layer grown at 750 °C is about 300 nm. These values are in agreement with our target growth thickness.

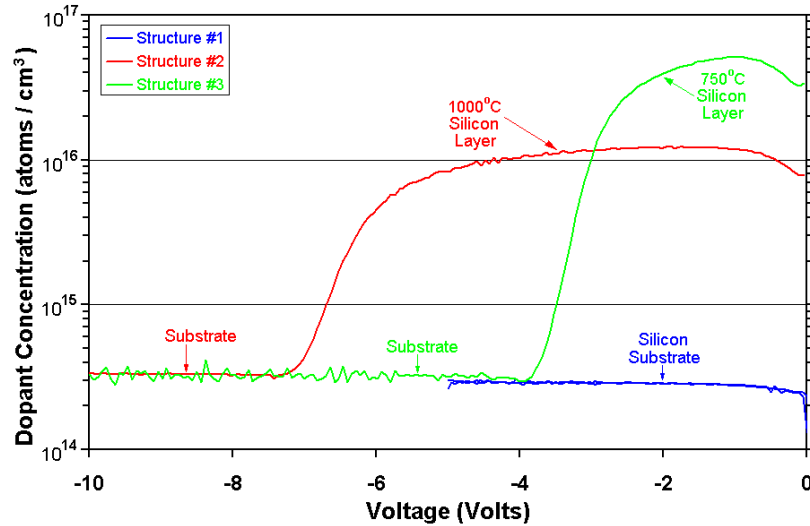


Figure 7.3. Dopant concentration vs. voltage for the Schottky diodes fabricated for three structures in Figure 7.1 on top of an n-type substrates. The separate layers for the structures are marked off based on the dopant concentrations.

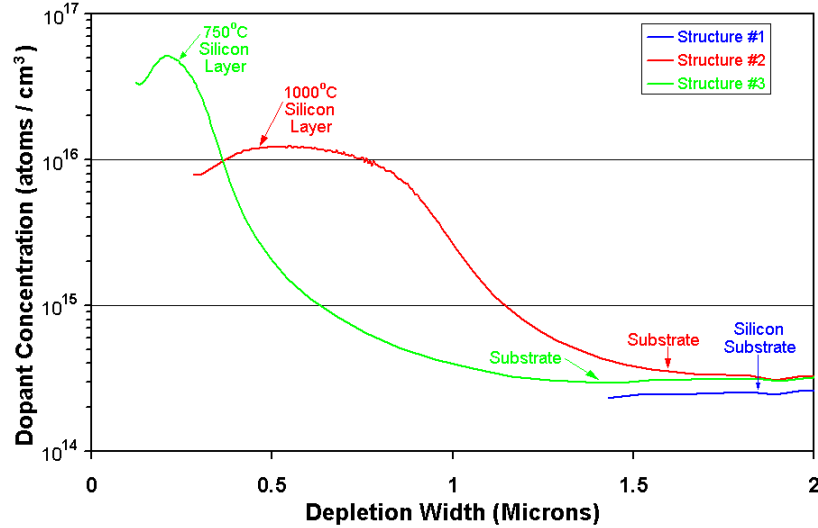


Figure 7.4. Depletion width versus dopant concentration for the Schottky diodes fabricated for three structures in Figure 7.1 on top of an n-type substrates. The separate layers for the structures are marked off based on the dopant concentrations.

Our results from CV measurements are compared with historic data based on SIMS measurements of phosphorus dopant concentration. We make the assumption that the phosphorus concentration measure by SIMS is 100% electrically active, (i.e. all substitutional phosphorus). The results are compared in Figure 7.5 below.

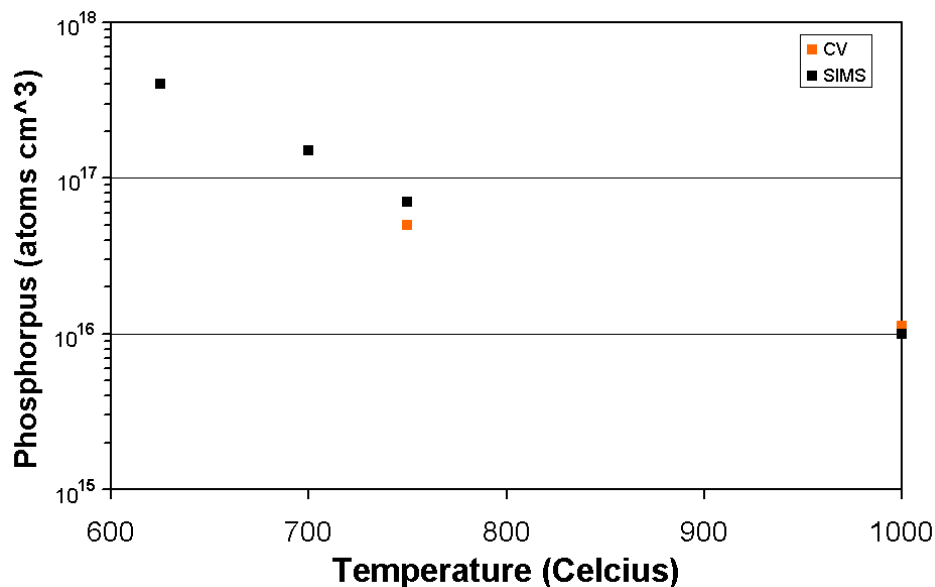


Figure 7.5. Phosphorus concentration vs. the growth temperature for silicon layers and SiGe layers (625 °C growth point) grown with DCS as the silicon source. The phosphorus concentration measured by SIMS is in solid black squares, while the concentration measured by CV is in solid orange squares.

We find that the CV results are in good agreement with our historic SIMS data. The historic SIMS data is an average of multiple SIMS samples. We find a trend in that as the temperature of growth of the silicon layer is lowered more phosphorus is incorporated into the silicon layer. Furthermore, there is also an increase in phosphorus concentration in the $\text{Si}_{0.8}\text{Ge}_{0.2}$ layers grown at 625 °C. However, we believe that the increase in SiGe layer is due to the germanium and not the reduced growth temperature [7.6].

7.2.2 Phosphorus Background from SIMS

In all of our SIMS analysis of samples that used DCS as the silicon source, we observed a phosphorus background on the order of $10^{17} / \text{cm}^3$. No phosphorus doping level above the SIMS resolution limit ($\sim 5 * 10^{16} / \text{cm}^3$) was observed with our other silicon precursors (Table 3.1). Shown in Figure 7.6 below is the SIMS result of a sample with a Si/SiGe/Si structure. All layers grown in this sample are not intentionally doped with phosphine, PH₃ (our typical phosphorus dopant gas).

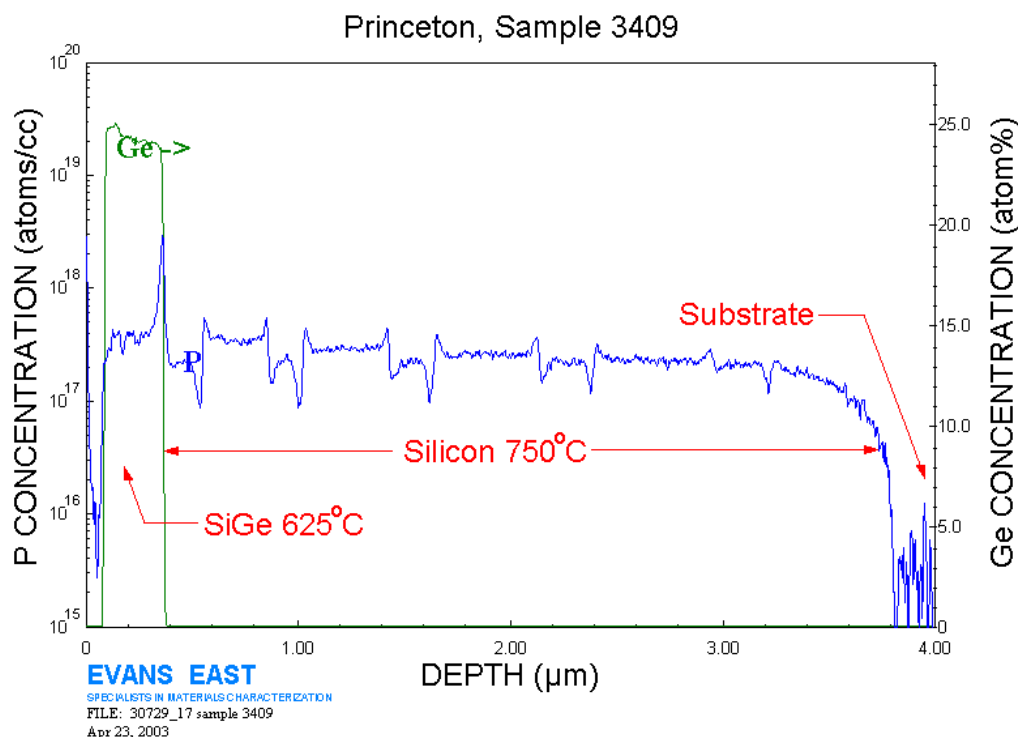


Figure 7.6. Phosphorus concentration (blue) vs. depth measured by SIMS for sample 3409. The germanium concentration (green) of the SiGe layers is shown on the secondary y-axis. The growth temperatures of the silicon layers are marked out in red. The phosphorus blips in the epitaxial layer grown at 750 °C may be SIMS artifacts due to the boron doping in five layers each $\sim 200\text{nm}$ thick (not shown in plot).

In sample 3409, we observe several trends from the phosphorus background concentrations. The first trend is that there is a transient starting from the substrate, where the phosphorus background doping builds up until it reaches a steady state concentration. Next we observe a spike in phosphorus concentration at the silicon / SiGe interface. The phosphorus concentration then has a transient decay in the SiGe layer, before reaching steady state. These trends are indicative of a surface segregation effect where the phosphorus atoms deposited onto the silicon surface are not being incorporated into the solid but rather “riding” back up onto the surface. What this means is that only a portion of the adsorbed surface phosphorus atoms are being incorporated. The rest of the surface phosphorous atoms remain on the growing interface as each layer is incorporated. This leads to a buildup effect where the surface now has more phosphorus atoms until a steady state is reached. This surface segregation effect was observed in all of our epitaxial samples grown with DCS as the silicon source gas. In Section 7.3 we formulate a phenomenological model and explain this effect. Another sample (2947) shown in Figure 7.7 below also depicts this effect.

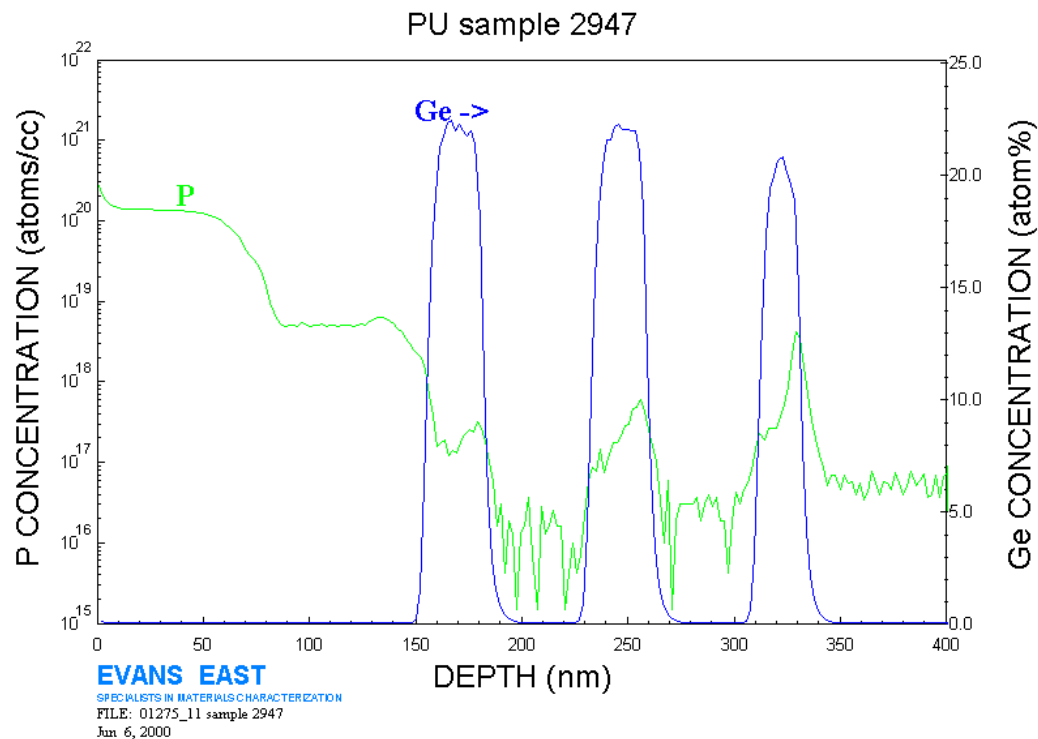


Figure 7.7. Phosphorus concentration (blue) vs. depth measured by SIMS for sample 2947. The germanium concentration (green) of the SiGe layers is shown on the secondary y-axis. The growth temperature of the silicon layers is 725 °C and the growth temperature of the SiGe layer is 625 °C.

In sample 2947 starting from the right (400 nm on the plot) and moving left we note that at each silicon / SiGe interface there is a spike in phosphorus concentration similar to the SIMS of sample 3409. In each of the successive silicon layers (going from right to left) the background phosphorus layer decreases and along with the subsequent spike in the SiGe layer. This indicates that the phosphorus concentration on the silicon surface has decreased after the growth of a SiGe layer. The last two phosphorus layers (5×10^{18} and 10^{20}) were intentionally doped. We can summarize our observations (Figures 7.5, 7.6 and 7.7) into four trends.

- 1) A buildup of doping in low temperatures silicon layers to a steady state value

- 2) Increased phosphorus concentration at lower temperature growths
- 3) Increased concentration upon switching from silicon to silicon-germanium layers
- 4) Decay transients observed in silicon-germanium layers

We will explain the reason for these trends in the next section.

7.3 Phenomenological Model of Phosphorus Adsorption/Incorporation

7.3.1 Model Assumptions and Equations

We develop a phenomenological model for the mechanism of the surface segregation of phosphorus and utilize this model to explain the background doping trends of phosphorus. Our model is a surface kinetic model. There are four possible kinetic process steps that can take place on the surface of silicon. A schematic of these steps are shown in Figure 7.8 below.

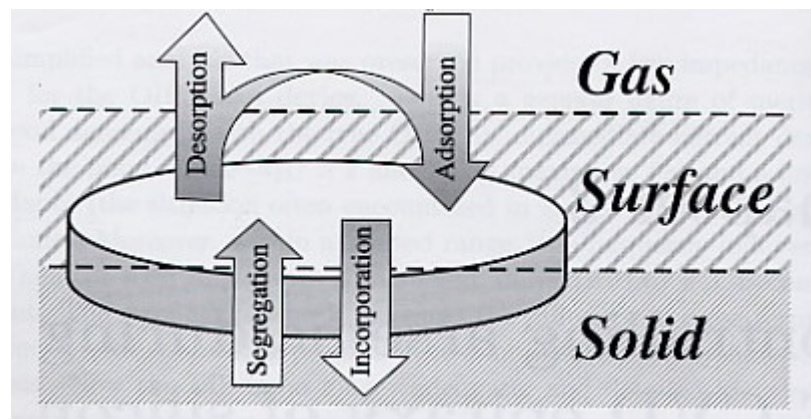


Figure 7.8. Schematic of the surface kinetics of a silicon adatom on the silicon surface. The four different processes (adsorption, desorption, segregation, and incorporation) are shown. [7.7]

The four kinetic steps are desorption from the silicon surface into the gas phase, adsorption from the gas phase onto the silicon surface, incorporation from the surface into the solid, and segregation from the solid back onto the surface. We can write the change in phosphorus surface concentration with the following equation:

Eq. 7.5

$$\frac{d\theta}{dt} = A - D + S - I$$

Where θ is the surface concentration of phosphorus, A is adsorption, D is desorption, S is segregation from the substrate back to the surface and I is incorporation. Based on the results in another paper, we safely assume that no desorption can occur at temperatures $< 800 \text{ }^{\circ}\text{C}$ [7.8].

We will describe the adsorption as a function of temperature, material and growth conditions (i.e. $A = A(T,M)$ where T is the temperature and M is the material). We will assume that no segregation (diffusion) from the substrate occurs back to the surface ($S = 0$). Due to the small diffusion constants at low temperatures, (i.e. $4.2 \times 10^{-19} \text{ cm}^2/\text{s}$ at $700 \text{ }^{\circ}\text{C}$ & $3.6 \times 10^{-18} \text{ cm}^2/\text{s}$ at $750 \text{ }^{\circ}\text{C}$ [7.9]), atoms in the substrate cannot diffuse back to the growing surface. This segregation is different than surface segregation, later described in this chapter. We write the equation for the diffusion length below:

Eq. 7.6

$$L = \sqrt{(D * t)} \Rightarrow t = L^2 / D$$

where, L is the diffusion length, D is the diffusion constant and t is time. For instance, to segregate (diffuse) through two monolayers at $700 \text{ }^{\circ}\text{C}$, it takes 103 seconds. During that time 190 monolayers of silicon are grown for our typical growth rates. We assume the incorporation I, is a linear function of the surface concentration θ , and an incorporation

constant that is dependent on temperature, material, and growth conditions (i.e. $I = \theta_s * i(T,M)$).

Equation 7.5 is rewritten as the following equation below:

$$\text{Eq. 7.7} \quad \frac{d\theta}{dt} = A(T,M) - \theta_s * i(T,M)$$

We will obtain the boundary conditions from the initial concentration and the steady state final condition to solve the non-homogenous linear differential equation. At steady state, $d\theta / dt = 0$, hence $A(T,M) = \theta_s * i(T,M) = I(T,M)$, so that the adsorption is equivalent to the incorporation. This is expected since at steady state every adatom adsorbed is incorporated. We know that the dopant concentration N_D , is equal to the incorporation rate ($I(T,M)$) divided by the growth rate, G_R . We can now express the adsorption rate as the following equation:

$$\text{Eq. 7.8} \quad A(T,M) = \theta_s * i(T,M) = I(T,M) = N_D * G_R$$

When not in steady state if A and i are constant, we can also express the surface concentration as a function of time with a steady state term and a transient term.

$$\text{Eq. 7.9} \quad \theta_s = \frac{A(T,M)}{i(T,M)} + C * e^{-t*i(T,M)}$$

where C is a constant determined by the boundary conditions. At steady state the surface concentration is the adsorption divided by the incorporation ($\theta_s = A(T,M) / i(T,M)$). The dopant concentration in the growing layer is now rewritten in Equation 7.10 below:

$$\text{Eq. 7.10} \quad N_D(t) = \frac{I}{G_R} = \frac{\theta_s(t) * i(T,M)}{G_R}$$

The instantaneous doping is determined by the surface concentration, incorporation time constant and growth rate. There are only two fitting parameters in our model: the adsorption rate, $A(T,M)$ and the incorporation constant, $i(T,M)$, both of which depend on the temperature, T , and the material, M (silicon or $\text{Si}_{1-x}\text{Ge}_x$) and the growth conditions. From these two parameters both the surface concentration θ and the dopant concentration N_D are fitted to the SIMS results.

7.3.2 Demonstration of Model Fitting and Results

A program was written using MATLAB for curve fitting our model with the SIMS results. A demonstration fit was done for sample 3409 (shown in Figure 7.6) in Figure 7.9 below:

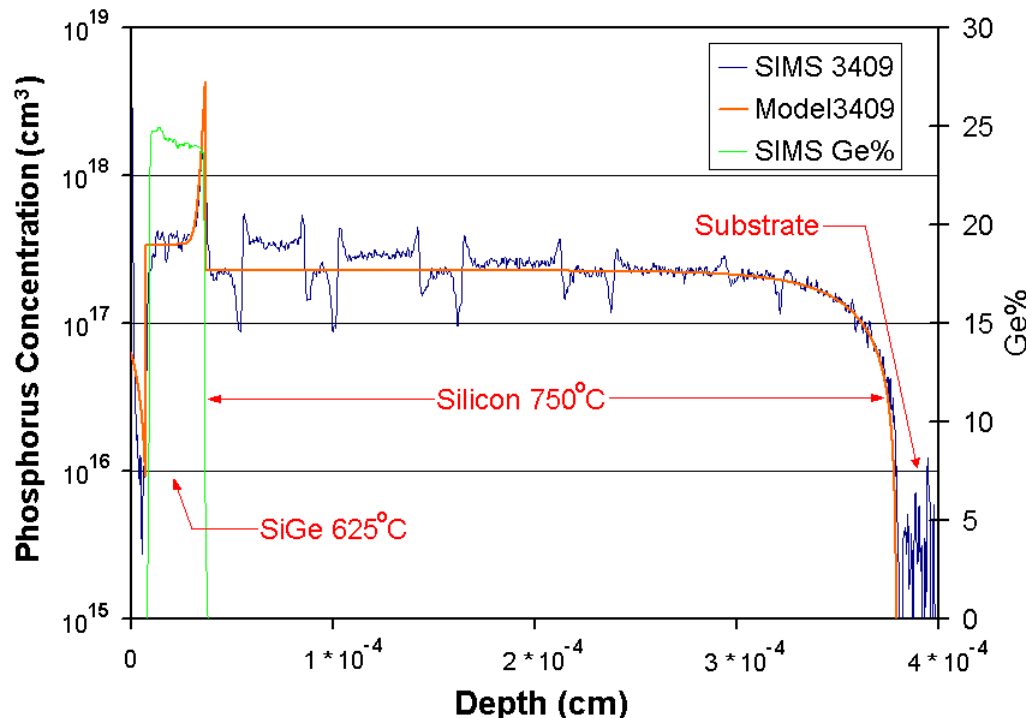


Figure 7.9. Demonstration fit of our model (orange) with the SIMS (blue) plot of phosphorus concentration vs. depth for sample 3409 (Figure 7.6).

$A(T,M)$ and $I(T,M)$ for a silicon layer grown at 750 °C and for the silicon germanium layer grown at 625 °C. In the next few figures we will explain in detail how we fit our model to obtain the parameters for $A(T,M)$ and $I(T,M)$. We begin our model at the start of growth of sample 3409. The initial surface phosphorus concentration at the start of epitaxy is set to zero (ideal clean surface). Shown in Figure 7.10, is a plot of the dopant concentration versus the depth of the sample. The growth is in the opposite direction of the depth (i.e. depth of 0 corresponds to the surface of the sample), growing from right to left in Figure 7.9 above.

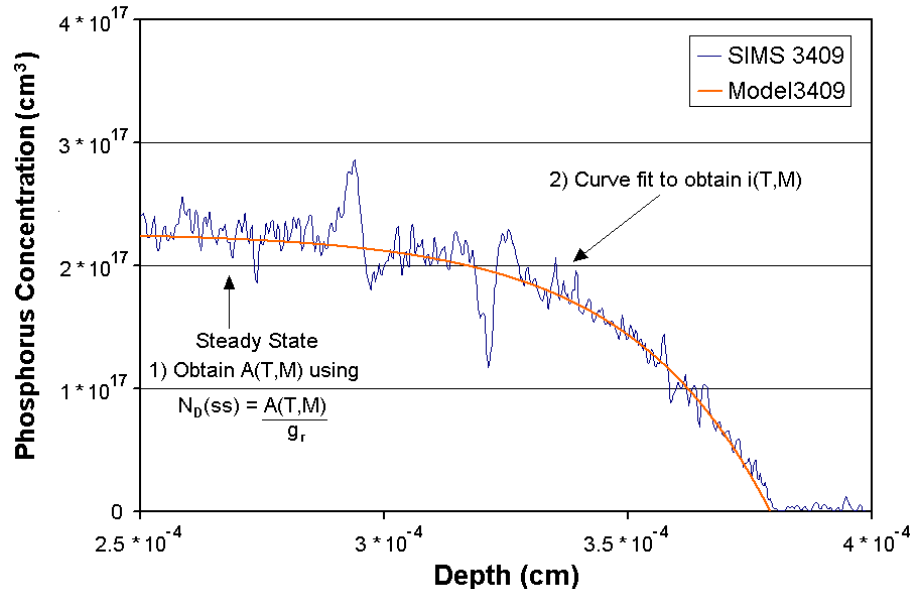


Figure 7.10. Model fit of phosphorus concentration versus depth comparing the SIMS result (blue) with our model (orange) results. The first two steps of modeling the dopant concentration for the sample 3409 are shown in this figure.

We first determine the adsorption rate of phosphorus onto the silicon surface. We do this we take the the dopant concentration at steady state, $N_D(ss)$, and multiply that by the growth rate, based on SIMS, to determine the adsorption rate, $A (T,M)$. At steady state everything adsorbed onto the surface is incorporated and the doping concentration is

equal to the adsorbed phosphorus atoms divided by the growth rate. We then fit the curve to obtain the incorporation rate, i (T,M). The surface concentration was also determined using Equation 7.9 above. Now that we have determined both the adsorption and incorporation rate we can calculate the surface concentration based on Equation 7.9. The surface concentration versus depth is plotted in Figure 7.11 below. From Figure 7.11 we observe that the surface concentration is slowly building up to a certain steady state value in the range of $6-7 * 10^{12} / \text{cm}^2$. This is indicating that the phosphorus on the surface is segregating back to the surface (i.e. riding back up to the surface instead of being incorporated), with approximately one hundredth of a monolayer of phosphorus left on the surface.

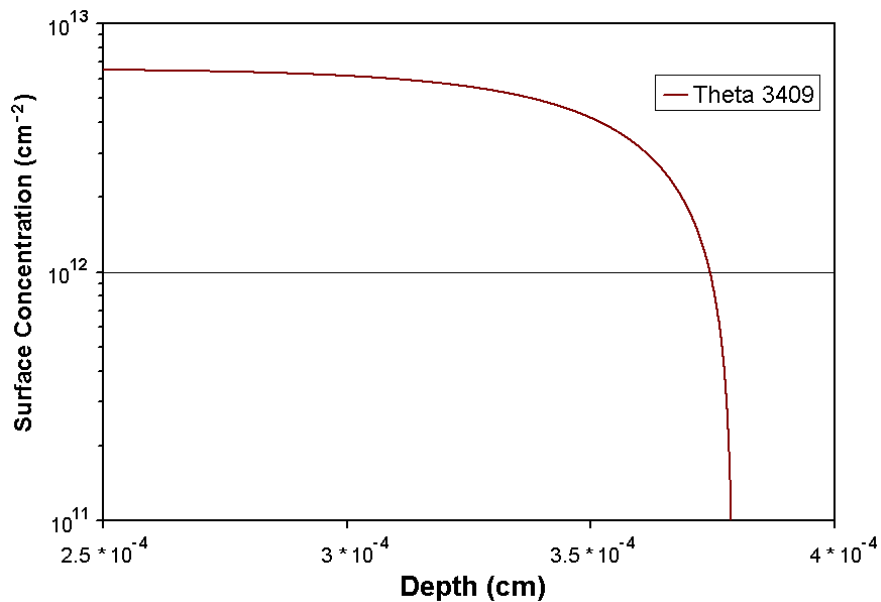


Figure 7.11. Plot of surface phosphorus concentration versus the depth. The surface phosphorus concentration was determined from our model.

We now demonstrate our model fit for the rest of the sample 3409 starting from the transition from Si to SiGe and into the Si capping layer. The comparison between the model and the SIMS result is shown below in Figure 7.12.

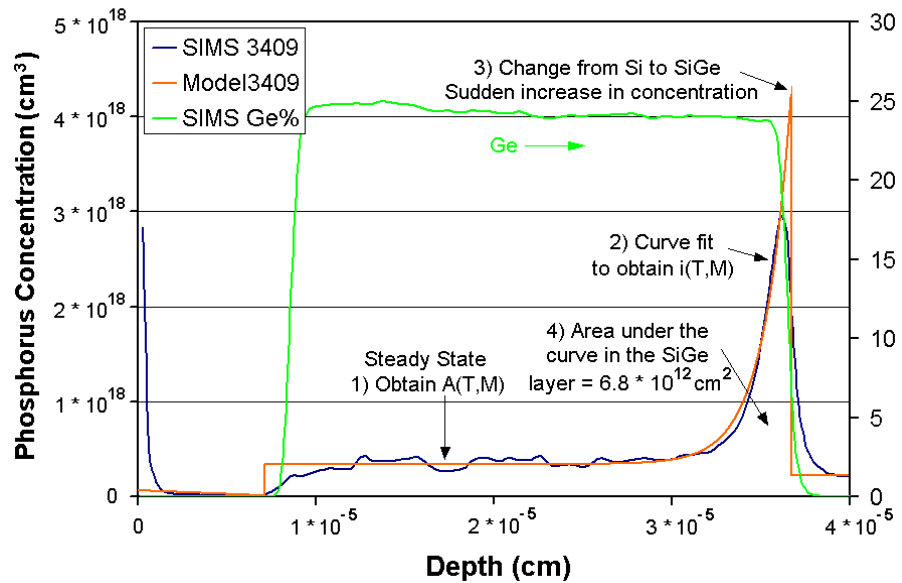


Figure 7.12. Model fit of phosphorus concentration versus depth comparing the SIMS result (blue) with our model (orange) results.

We first obtain $A(T,M)$ from the steady state value of N_D (Step 1). Then we fit the curve of the exponential decay of the phosphorus in the SiGe layer to obtain $i(T,M)$ (Step 2). Note that there is a sudden discontinuous (Step 3) increase in the phosphorus concentration (7.12) at the start of the SiGe layer. This is due to a difference in the incorporation rate of phosphorus between silicon and SiGe (i.e. $i(750^\circ\text{C}, \text{Si})$ not equal to $i(625^\circ\text{C}, \text{Si}_{0.8}\text{Ge}_{0.2})$). Note that the area under the curve from the peak phosphorus concentration to the steady state concentration is equivalent to the surface concentration at the interface at the transition from silicon to SiGe deposition. In Figure 7.13 below, we plot the surface concentration of phosphorus starting from the transition from Si to SiGe and into the Si capping layer.

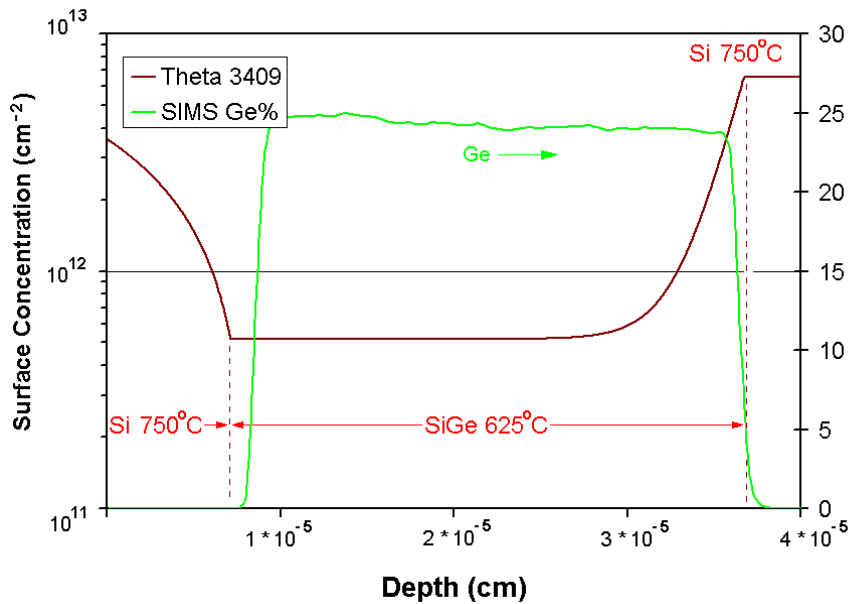


Figure 7.13. Model fit of surface concentration versus depth based on our model.

The surface concentration at the start of the SiGe layer begins to decrease at the start of the interface. We note that the steady state surface concentration in the silicon layer was 6.8×10^{12} atoms/cm² in the silicon layer grown at 750 °C. When the growth is switched from silicon to SiGe the surface concentration decreases to a new steady state value of $\sim 5 \times 10^{11}$ atoms/cm². This implies that the incorporation rate of phosphorus is higher on a SiGe surface compared with the incorporation rate of phosphorus on a silicon surface. Phosphorus on the surface is more likely to be incorporated into the film instead of segregating back to the growing surface. A larger portion of the phosphorus adatoms on the surface is incorporated in a SiGe layer, explaining the sudden spike in phosphorus concentration upon the switch from silicon to SiGe, as now more of the surface phosphorus atoms are incorporated. This higher incorporation rate also reduces the phosphorus surface coverage in the SiGe layer.

We model the phosphorus concentration profiles for multiple samples. We plot the phosphorus adsorption rate and incorporation constant in silicon at different

temperatures based on our simulation in Figures 7.14a and 7.14b. The surface concentration determined from the adsorption rate and incorporation constant is plotted in Figure 7.14c.

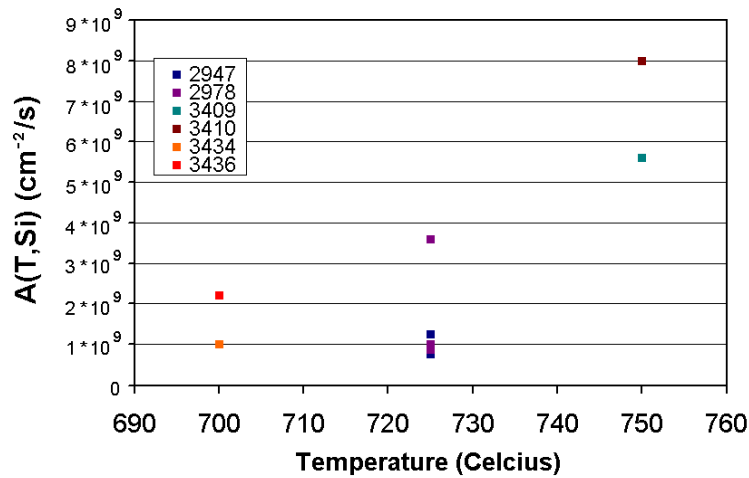


Figure 7.14a. Adsorption constant of phosphorus, $A(T,Si)$, versus temperature in silicon layers of six different samples.

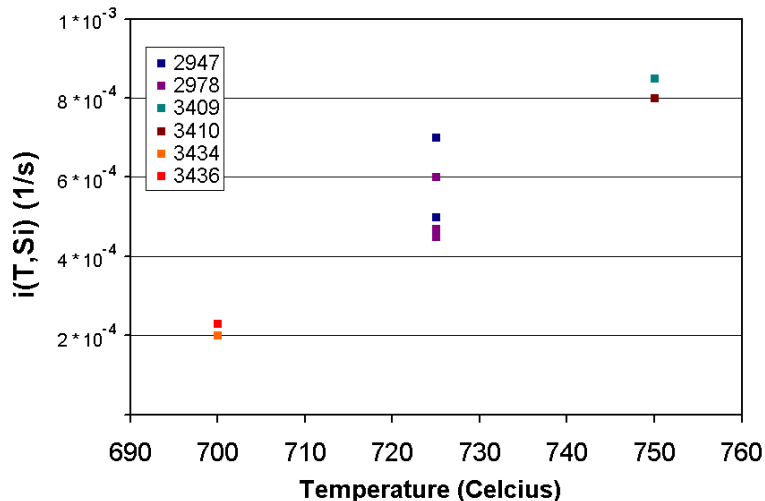


Figure 7.14b. Incorporation constant of phosphorus, $i(T, Si)$, versus temperature in silicon layers of six different samples.

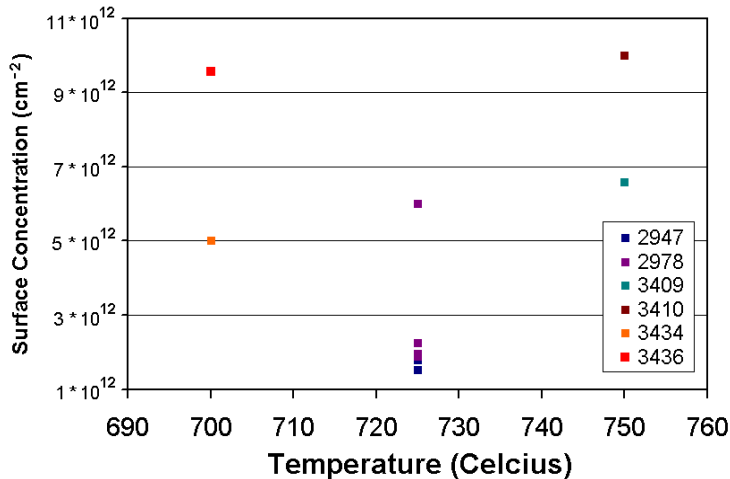


Figure 7.14c. Steady state surface phosphorus concentration versus temperature for silicon layers in six samples. The surface concentration was determined from our model.

From Figure 7.14a above, the data has some scatter most likely due to different background phosphorus levels in the reactor chamber on different days. As a general trend the adsorption rate is increasing faster than linearly with respect to temperature and on the order of 10^9 atoms / $\text{cm}^2\text{-sec}$. This may be due to more hydrogen desorption from the surface at higher temperatures, allowing more open sites for phosphorous adsorption, for the same phosphorus background source. There may also be increased desorption off of the chamber walls, where phosphorus may have adsorbed onto, leading to readsorption onto the silicon surface. In Figure 7.14b, we find that the incorporation constant is also increasing with temperature. This has less scatter than the adsorption, A. This is expected since it is a property of the surface, describing what fraction of the surface layer is incorporated into the solid as the growth proceeds. We note that the surface concentration (Figure 7.14c) has no clear trend with respect to temperature.

We plot the phosphorus adsorption rate and incorporation constant in SiGe at 625 °C for different concentrations based on our simulation in Figures 7.15a and 7.15b. The

surface concentration determined from the adsorption rate and incorporation constant is plotted in Figure 7.15c.

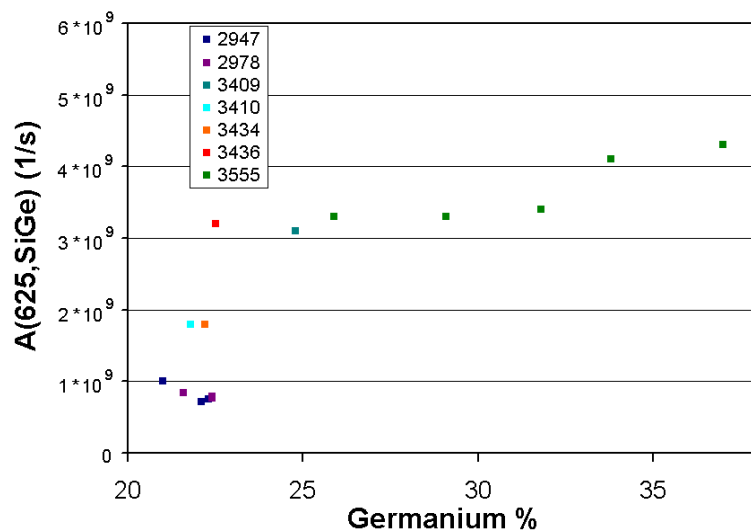


Figure 7.15a. Adsorption constant of phosphorus, $A(625^\circ\text{C}, \text{SiGe})$, versus germanium percentage of seven different samples.

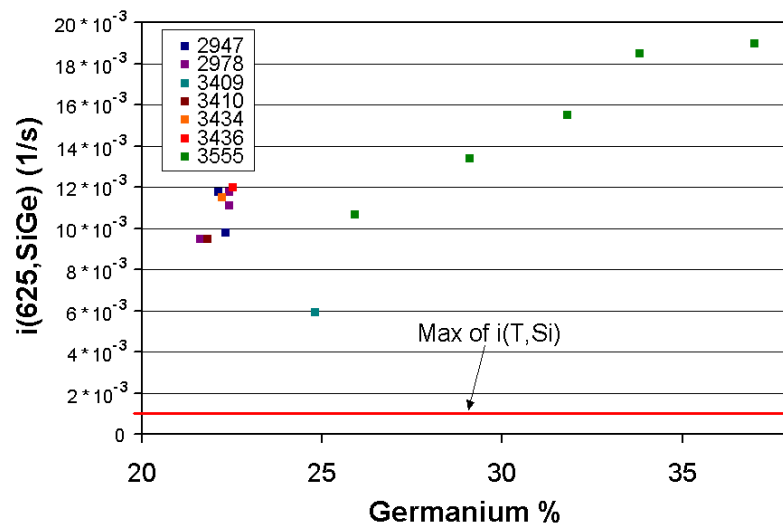


Figure 7.15b. Incorporation constant of phosphorus, $A(625^\circ\text{C}, \text{SiGe})$, versus germanium percentage for seven different samples. The red line indicated the maximum incorporation constant of the silicon samples in Figure 7.14b.

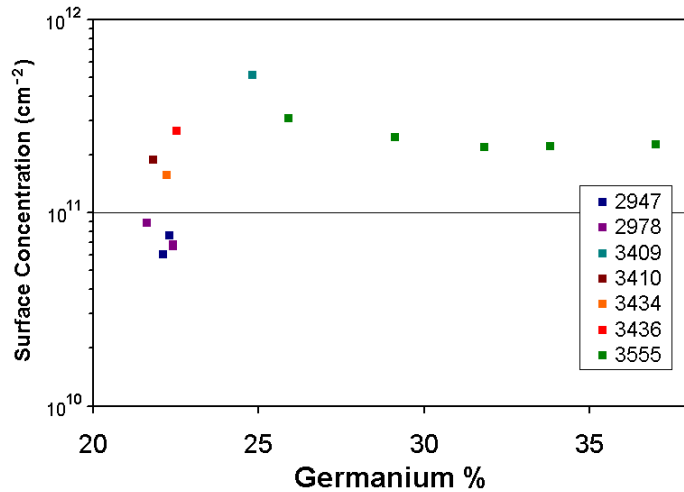


Figure 7.15c. Steady state surface phosphorus concentration versus germanium percentage for seven different samples. The surface concentration was determined from our model.

In Figure 7.15a, as we increase the germanium content in the layers, the adsorption constant increases (but not significantly). We do not know if the jump from $\sim 21\%$ to 25% is significant or just due to sample to sample variations, such as lower background phosphorus in the reactor when the samples for $\sim 21\%$ Ge were grown. The adsorption rate is on the order of 10^9 atoms/ cm^2 , on the same order as the adsorption rate resulting from silicon films. The incorporation rate constant, $i(625^\circ\text{C}, \text{SiGe})$, which determines the amount of the surface concentration incorporated into the film, is an order of magnitude greater than that for silicon. This is consistent with the phosphorus spikes when transitioning from silicon to SiGe layers (see equation 7.10 above, also trend (3)). The high incorporation rate constant indicates that there is less surface segregation of phosphorus in the presence of germanium on the growth surface. Furthermore, we compare the steady state phosphorus surface concentrations for the silicon and SiGe layers (Figures 7.14c & 7.15c above) determined from our model. The steady state surface concentrations for the silicon are roughly in the mid- $10^{12}/\text{cm}^2$ range (roughly one hundredth of a monolayer). The surface concentration in the SiGe layers are on the

$10^{11}/\text{cm}^2$ range, approximately one order of magnitude less than the surface concentrations in the silicon layers. This result arises from the fact that the surface state concentrations are proportional to the adsorption rate divided by the incorporation rate constant. The adsorption rates of the silicon and SiGe layers are on the same order of magnitude, $\sim 10^9$. The incorporation rate constant for the SiGe layers are an order of magnitude higher compared with the incorporation rate constant for the silicon layers. The incorporation constant determines the amount of phosphorus segregation. The larger the incorporation constant the more dopant is incorporated (Equation 7.10) and the steeper the rise or decay of the phosphorus profile (Equation 7.9). What this means on a microscopic level is that a SiGe surface has less surface phosphorus atoms due to the fact that they are less likely to segregate (ride back up on the surface), causing the rising and decaying phosphorus concentration profile to have a sharper turn on/off slope.

7.4 Microscopic Model of Phosphorus Segregation

7.4.1 Model

In this section we will explain what is happening on the surface on a microscopic level and relate this with our phenomenological model in the previous section, as well explain the four doping trends. We have already determined that the phosphorus adsorbed onto the surface and segregates back to the surface during epitaxial growth. This implies that it is energetically favorable for the phosphorus adatoms to be on the surface. The energy of the atom at the surface must therefore be less than its energy in the bulk. For the adatoms to segregate back to the surface, they must pass through an energy barrier. We also know that once the phosphorus is incorporated into the solid, it does not diffuse back to the

surface for growth at low temperature. Shown in Figure 7.16 below is the energy diagram for a phosphorus adatom in silicon [7.10].

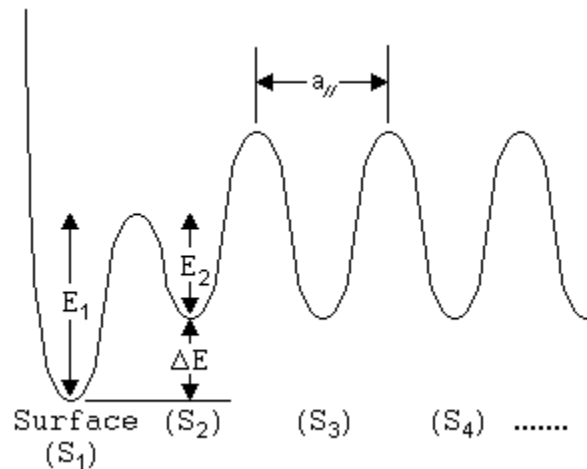


Figure 7.16. Energy diagram of a phosphorus atom in different silicon layers. The silicon layers are defined by $S_1, S_2, S_3 \dots$ where the subscript denotes the layers from the surface with 1 being the surface layer, and $a_{||}$ is the interatomic spacing between two layers. E_1 and E_2 are the energies required to pass between the barrier between the first two surface layers.

As shown in the figure above, the surface energy of the phosphorus adatom is lowest at the surface, S_1 . The energy of the phosphorus atom is higher in the solid than on the surface. When the phosphorus atom is in the second layer S_2 , it sees a smaller energy barrier, than when it is further into the solid, such as in layers S_3 or S_4 . This is because the phosphorus atom is trapped in the solid, whereas, on the subsurface layer, S_2 , it can segregate back to the surface. In Figure 7.17 we show a diagram illustrating the possible mechanisms of a phosphorus adatom in the two possible states (an adatom on the surface in layer S_1 and the adatom in one layer below the surface S_2).

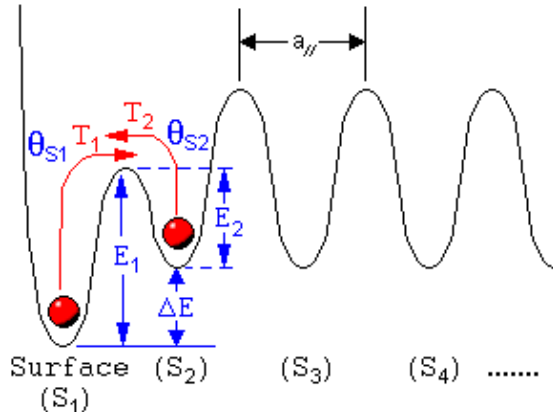


Figure 7.17. Diagram showing the incorporation and segregation mechanisms from an energy perspective. θ_{S1} and θ_{S2} are the phosphorous concentrations in the surface layer S_1 and the next layer below the surface S_2 . E_1 and E_2 are the energy barriers for an adatom to cross from layer S_1 to S_2 (E_1) and the energy to cross from layer S_2 to S_1 (E_2) respectively. T_1 and T_2 are the transition rate per atom going from layer S_1 to S_2 and from layer S_2 to S_1 respectively.

θ_{S1} and θ_{S2} are the phosphorous concentrations in the surface layer S_1 and the next layer below the surface S_2 . E_1 and E_2 are the energy barriers for an adatom to cross from layer S_1 to S_2 (E_1) and the energy to cross from layer S_2 to S_1 (E_2) respectively. T_1 and T_2 are the transition rate per atom going from layer S_1 to S_2 and from layer S_2 to S_1 respectively. In order for the phosphorus adatom to be incorporated in the solid it would have to be in layer S_2 when the new silicon monolayer is grown (Figure 7.18 dotted blue line).

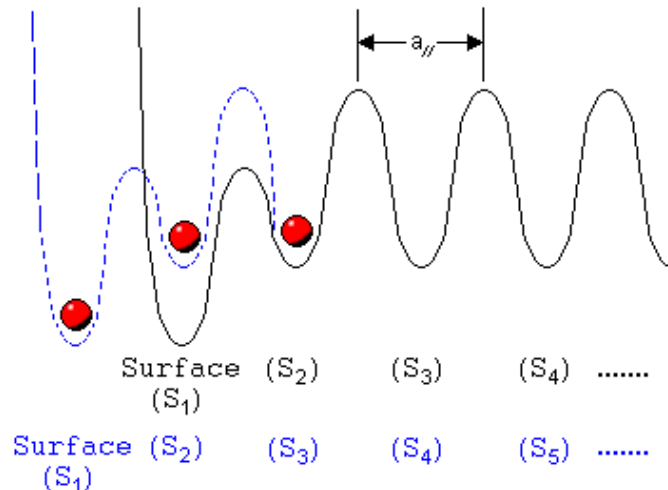


Figure 7.18. Diagram showing the change in energy barriers as a monolayer of silicon is grown onto the structure.

The phosphorus adatom will then be incorporated into the solid as the energy barrier required for diffusion in between bulk layers (i.e. from S_3 to S_2) are much higher than the energy barrier for diffusion from the second layer, S_2 , to the surface layer. If the adatom were on the surface layer S_1 when the new monolayer is grown on top of it, it would then be in layer S_2 (Figure 7.18 dotted blue line). In equilibrium, the rate of number of phosphorus atoms going between the layers S_1 and S_2 is constant (i.e. r_{12} (rate going from S_1 to S_2) = r_{21} (rate going from S_2 to S_1)). Since the rate is the surface concentration times the number of transitions this implies that $r_{12} = \theta_{S1} * T_1$ and $r_{21} = \theta_{S2} * T_2$, and $\theta_{S1} * T_1 = \theta_{S2} * T_2$. We write the transitions $T_{1,2}$ as a function of the energy barrier and temperature, $T_1 = C e^{-E_1/k_B T}$ and $T_2 = C e^{-E_2/k_B T}$, where C is a constant and k_B is Boltzmann's constant. From this we can obtain the ratio of the surface concentrations at steady state as the following equation:

$$\text{Eq. 7.11} \quad \frac{\theta_{S1}}{\theta_{S2}} = \frac{T_2}{T_1} = \frac{C * e^{-E_2/k_B T}}{C * e^{-E_1/k_B T}} = e^{-(E_2 - E_1)/k_B T} = e^{\Delta E/k_B T}$$

From the equation above we find that the ratio of the phosphorus concentration on the surface and the subsequent layer depends exponentially on the difference in the energies E_2 and E_1 , ΔE (see Figure 7.17).

We will now use this to explain why we observe the exponential rise and decay tails of the phosphorus doping. We will consider the simple case of a constant number of surface atoms with no further adsorption such that $\theta_T = \theta_{S1} + \theta_{S2}$. θ_T is the total of atoms on both the top surface layer, θ_{S1} , and the subsurface layer, θ_{S2} , the only layer that can directly segregate back to the surface layer, θ_{S1} . Let's define a "surface factor" f as $f = \exp(-\Delta E / k_B T)$. We can now write $\theta_T = \theta_{S1} + f \theta_{S1}$ using Equation 7.11. We can now write the surface concentrations θ_{S1} and θ_{S2} in terms of θ_T and f below in Equation 7.12.

Eq. 7.12

$$\theta_{S1} = \frac{1}{1+f} * \theta_T; \quad \theta_{S2} = \frac{f}{1+f} * \theta_T;$$

Note that if $f \ll 1$, as it would be if the case of surface segregation, $\theta_{S2}/\theta_T \sim f$. When the next monolayer is grown the concentration θ_{S2} is now trapped in. Thus we may think of f as the fraction of the total surface layer θ_T incorporated into the solid during the growth of each monolayer.

After the monolayer, the new total number of atoms in the surface and the first layer below the surface is $\theta_T' = \theta_{S1}$. The new surface concentrations are given by equation 7.13 below. The primes indicate the new concentration on the surface and in the next layer.

Eq. 7.13

$$\theta_{S1}' = \frac{1}{1+f} * \theta_T' = \frac{1}{(1+f)^2} * \theta_T; \quad \theta_{S2}' = \frac{f}{1+f} * \theta_T' = \frac{f}{(1+f)^2} * \theta_T;$$

The ratio of the concentration of the previous layer to the new layer is $1/(1+f)$. This leads to exponential decay of the phosphorus concentration. We can write the surface concentration as the following equation:

Eq. 7.14

$$\theta_s = C * e^{\frac{-x}{L_t}}$$

where L_t (the transition length) is defined as the distance for the surface concentration to decay by a factor of $1/e$. Assume that this requires N atomic layers so $L_D = a_{Si} N$. Then the ratio of the phosphorus concentration between the N^{th} layer (transition layer) and the original layer is $\frac{1}{(1+f)^N} = \frac{1}{e}$. We plot the concentrations of the next several layers in Figure 7.19 below:

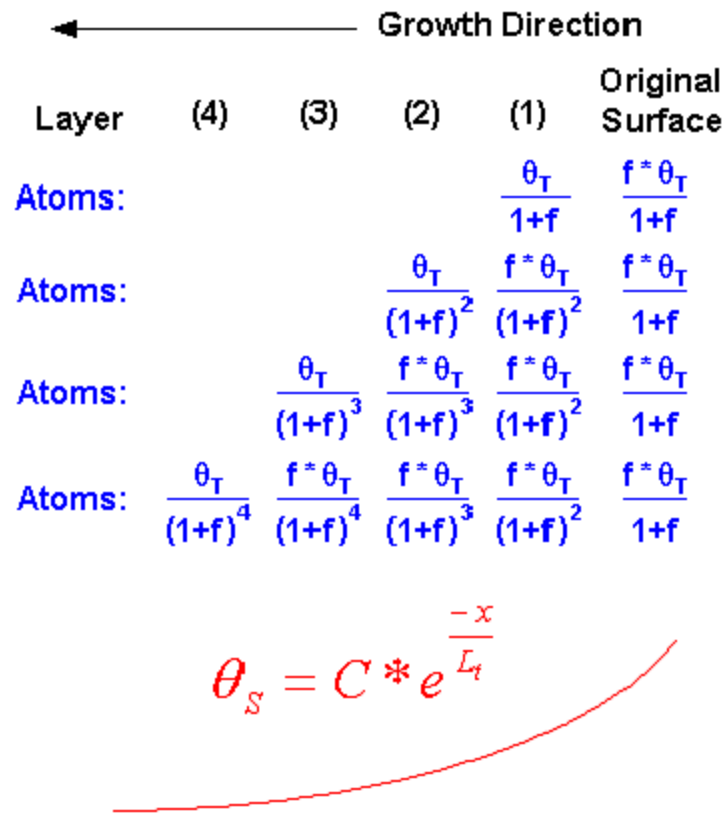


Figure 7.19. Table of surface concentrations starting with a total of θ_T surface phosphorous atoms and segregating the surface atoms as the next layer is grown for a total of four layers grown. The surface concentration follows an exponential decay.

As shown in Figure 7.19, surface segregation of phosphorus adatoms leads to the exponential decay that is observed in the SiGe layers.

We now quantitatively relate our phenomenological model with our microscopic model. From above, $(1+f)^N = e$, so

Eq. 7.15

$$N = \frac{1}{\ln(1+f)}.$$

Since $N = \frac{L_T}{a_{Si}}$, we have an expression which relates the decay length L_T to f , which itself depends on the energy difference of the phosphorus and the surface and the next layer below it.

Eq. 7.16

$$L_T = \frac{a_{Si}}{\ln(1+f)}$$

The decay of the surface concentration is then (from Equation 7.14)

Eq. 7.17

$$\theta_S = C * e^{\frac{-x}{L_T}} = C * e^{\frac{-x \ln(1+f)}{a_{Si}}}$$

From our phenomenological model, the transient is $\theta_S = C * e^{-t*i(T,M)}$ (Equation 7.9).

Comparing Equations 7.9 and Equation 7.17 and noting $x = g_r * t$ gives

Eq. 7.18

$$L_T = g_r / i(T,M)$$

Using Equations 7.16 & 7.18 to eliminate L_T one has

Eq. 7.19

$$\ln(1+f) = a_{Si} * i(T,M) / g_r$$

To find the surface factor f from the data, in principle one can use the data for L , estimated directly from SIMS, to work backwards using Equation 7.16. Alternatively, f can be found from $i(T,M)$ using Equation 7.19.

7.4.2 Comparison of Model and Data

Our model implies that as we increase the temperature, f increases (becomes closer to one) and the fraction of atoms incorporated increases. Thus the transition length should decrease at high temperatures. In Figures 7.20a & 7.20b below, we plot the transition lengths and the fraction incorporated in silicon layers at different temperatures.

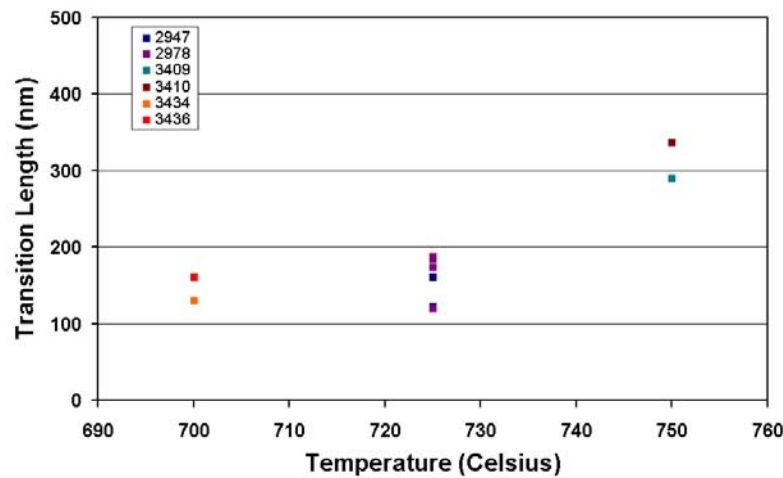


Figure 7.20a Transition length (nm) versus growth temperature of silicon layer for six different samples grown with DCS in hydrogen ambient.

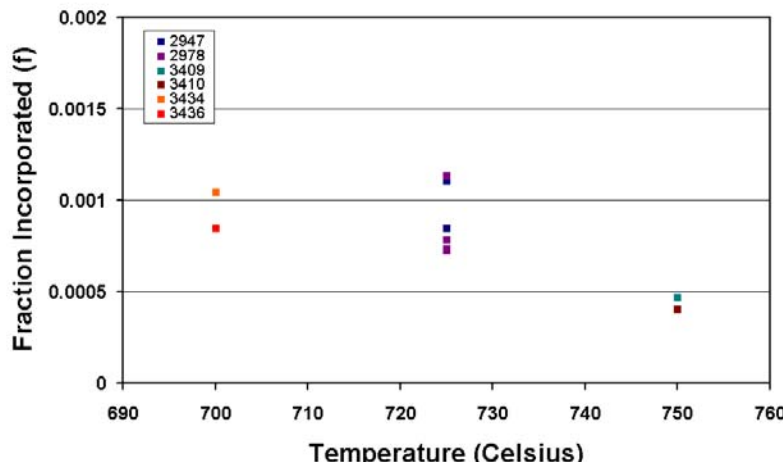


Figure 7.20b Fraction incorporated (f) versus growth temperature of silicon layer for six different samples grown with DCS in hydrogen ambient.

From Figure 7.20a above, we note that the transition is decreasing with temperature and the fraction of atoms incorporated increases with temperature. This is counterintuitive to what our model suggests. This implies that the ratio of surface to subsurface adatoms is unable to reach its equilibrium value (which was an assumption of the model). It seems that the atoms on the subsurface are not having enough time to segregate back to the surface. This indicates that to obtain a high concentration of phosphorus doping during silicon growth lower temperatures and/or higher growth rates should be used to “freeze out” the adsorbed adatoms. This implies that high-order silanes, because they allow lower growth temperatures and/or faster growth, should allow for higher incorporation levels for phosphorus doping. (As an aside, we would also like to note that the addition of chlorine during growth can increase the phosphorus dopant concentration levels by reducing the amount that is segregated back to the surface [7.12][7.13]).

7.5 Phosphorus Doping with High-Order Silanes

The growth of in-situ heavily doped ($> 10^{20}/\text{cm}^2$) phosphorus layers in silicon can be used to make low resistance layers, as desired in source/drain. Conventionally, to obtain these doping levels ion implantation is required. After ion implantation, the silicon surface becomes amorphous due to the implant damage and the dopants have to be activated (i.e. occur a substitutional lattice site). To repair all the ion implantation damage and to activate the dopants, annealing at high temperatures ($T > 900\text{ }^\circ\text{C}$) is required. Annealing at high temperatures however, causes the diffusion of phosphorous atoms, which prevents the formation of abrupt junctions and can change device profiles. In this section of the chapter we explore the use of high-order silanes for the growth of heavily doped phosphorus layers.

As described in previous sections of this chapter, the surface segregation of phosphorous makes it difficult to obtain high phosphorus doping concentrations. Furthermore, it has been shown that a high level of phosphorus doping can inhibit the growth of silicon by “poisoning” the surface (i.e. removing possible open sites for adsorption), thereby reducing the growth rate [7.13]. This occurs when a high phosphorus concentration builds up on the silicon surface and forms stable dimer pairs, which inhibit silicon adsorption.

We have previously shown (Chapter 4) that the growth with high-order silanes may not require open surface sites. A surface with a high level of phosphorus might not inhibit the growth rate when high-order silanes are used. High-order silanes also have high growth rates at low temperatures. We conducted experiments using phosphine to determine if there is any reduction of growth rate caused by phosphorus during epitaxial growth with disilane and NPS, as is observed with silane and DCS growth. Samples were grown with a chamber pressure of 6 torr and 3 slpm hydrogen flow with varying phosphine gas flows, silicon precursor gas flows and growth temperature. A plot of the normalized growth rate versus phosphorus flow (sccm) is shown in Figure 7.21 below.

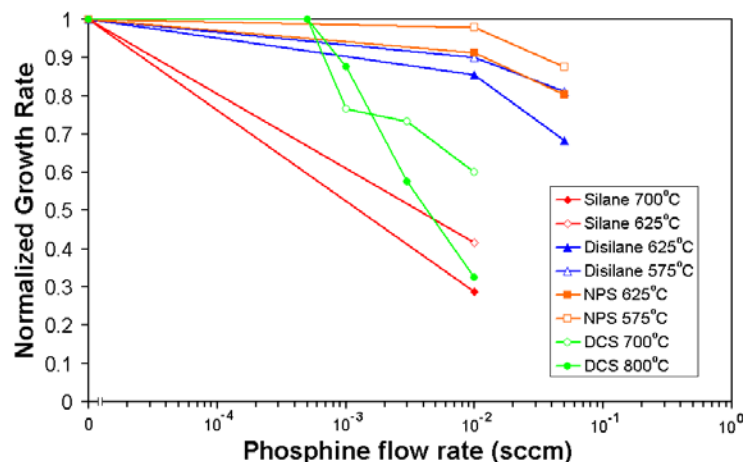


Figure 7.21. Normalized growth rate versus phosphine flow rate for four different silicon precursors at different growth temperatures. The growth rates (measured by SIMS) were normalized by the growth rate without any intentional phosphine doping.

As the phosphine flow is increased, the normalized growth rate decreases when the silicon source was silane or DCS. Ideally, the growth rates used in the experiments would be similar for different silicon precursors. However, due to experimental limitations (MFC flow controllers limiting the amount of gas we could flow) and the large discrepancy between the growth rates of the different precursors, the growth rates of the samples varied about one order magnitude for the samples. The growth rates without phosphine flow were 12.5 nm/min and 1.2 nm/min for silane at 700°C and 625°C; 19.5 nm/min and 3.7 nm/min for disilane at 625 °C and 575 °C; 23 nm/min and 4.8 nm/min for NPS at 625 °C and 575 °C; and 40 nm/min and 3 nm/min for DCS at 800 °C and 700°C respectively.

The decrease in the normalized growth rate is much smaller when disilane was the silicon source and was not observed when NPS was the silicon source. This may be due to the fact that the growth mechanism with high-order silanes is concerted reactions that do not depend on the open site fraction, unlike conventional gases such as DCS and silane. This may also imply a smaller phosphorus concentration on the growth surface with disilane and NPS.

We will now compare the total phosphorus concentration versus the phosphine flow rate in Figure 7.22 below, to determine if higher phosphorus concentrations can be achieved with high-order silanes.

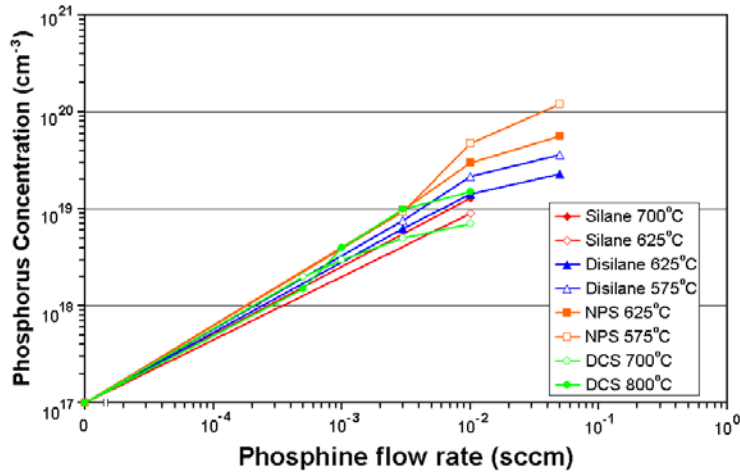


Figure 7.22. Phosphorus concentration versus phosphine flow rate (sccm) for four different silicon precursors at different growth temperatures. The phosphorus concentrations were determined from SIMS measurements and may not be electrically active (i.e. occupying substitutional sites). The DCS data was done by a previous student [7.14].

Due to the varying growth rates, it is difficult to obtain meaningful comparisons for the phosphorus concentrations. However, we observe that the highest phosphorus concentration achieved was done using NPS as the silicon source at a growth temperature of 575 °C, producing a concentration of $5 * 10^{19} \text{ cm}^{-3}$. Comparing the phosphorus concentrations at 575 °C for disilane (blue open square) and NPS (orange open square), we observe that the phosphorus concentration with NPS is about 2.5 times higher, despite a faster growth rate, 4.8 nm/min versus 3.7 nm/min for NPS and disilane respectively. Similarly, comparing the phosphorus concentration obtained at 625 °C with silane (red open square) and disilane (blue solid square) we observe that they are both similar, $\sim 1.5 * 10^{19} / \text{cm}^3$. However, the growth rate using disilane was 19.5 nm / min compared with a growth rate of 1.2 nm / min using silane. This indicates that disilane is more efficient at incorporating phosphorus than silane. We would also like to note that more phosphorus is incorporated at lower temperatures for NPS and disilane but not the case for silane and DCS. The phosphorus adsorption rate is plotted in Figure 7.23 below under steady state

conditions with every adsorbing phosphorus atom being incorporated, shown previously in chapter 4 (Figure 4.26).

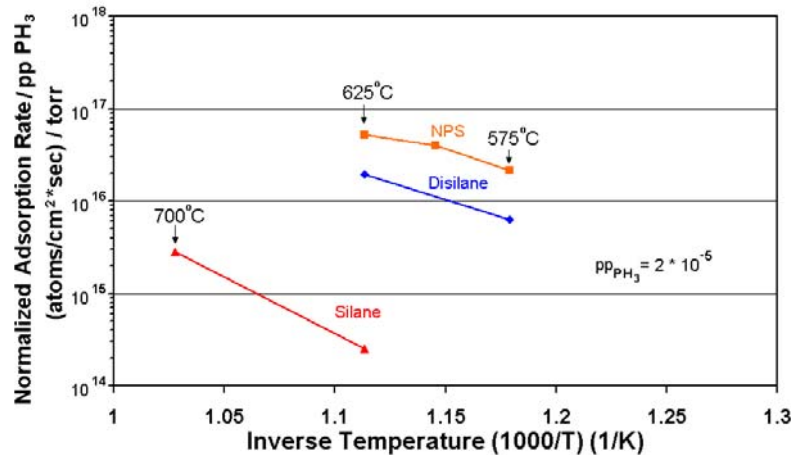


Figure 7.23. Normalized adsorption rate w.r.t. phosphine pressure vs. epitaxy temperature for the silicon sources of silane, disilane and NPS.

When we compare the phosphine adsorption rate for the three precursors at the same temperature, we observe that the phosphine adsorption rate increases with increasing silane order. Similar to boron, phosphine adsorption depends directly on the number of open sites. The increasing phosphorus adsorption rate indicates that the number of open sites for phosphorus adsorption is higher with high-order silanes, providing further evidence to the creation of open sites during epitaxial growth using high-order silanes.

We compare the growth rate vs. the phosphorus concentration in the silicon layers grown with different silicon precursors at different temperatures. The growth was done with a chamber pressure of 6 torr, with 3 slpm hydrogen flow and 0.01 sccm of phosphine flow (partial pressure = 2×10^{-5} torr). The results are plotted in Figure 7.24 below:

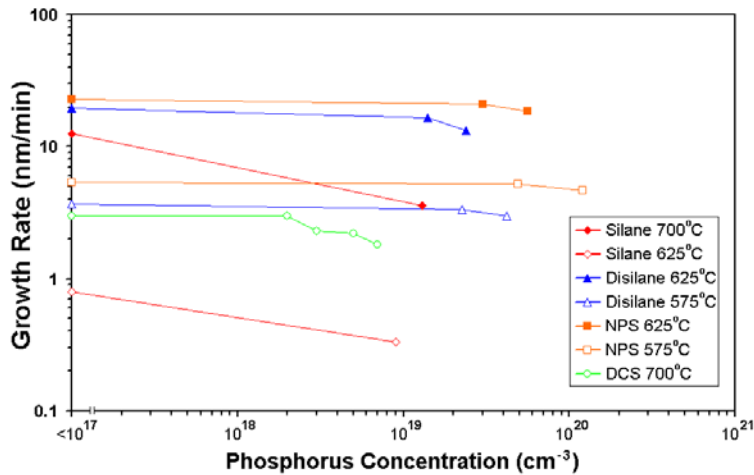


Figure 7.24. Growth rate vs. phosphorus concentration for different silicon sources at different temperatures. The growth was done with a chamber pressure of 6 torr, with 3 slpm hydrogen flow and 0.01 sccm of phosphine flow (partial pressure = 2×10^{-5} torr). The growth rate for the silicon precursors with no phosphine flow is displayed as $<10^{17}$. The silicon source flows were 26 slpm for DCS, 10 sccm of silane, 5 sccm of disilane, and 50 sccm of NPS in hydrogen respectively.

From Figure 7.24, we observe that for the same temperature (i.e. 625°C) with the same hydrogen flow and phosphine partial pressure, the amount of phosphorus incorporated in the layer increases with increasing silane order. The increase in growth rate due to the high-order silane is allowing for more incorporation of phosphorus into the solid. This increase in phosphorus incorporation may be due to the “freeze out” effect, where the phosphorus atoms in the first layer beneath the growth surface is not given the time to segregate back to the surface. As the temperature is lowered, more phosphorus is incorporated into the film despite the decrease in growth rate. This is also due to a “freeze out” effect (but related to temperature as opposed to growth rate).

Finally, we compare the rise and decay lengths of the phosphorus profiles of samples grown with NPS and disilane at two different temperatures of 575°C and 625°C at 6 torr, with 3 slpm hydrogen flow and 10^{-2} sccm of phosphine gas (Figure 7.25). The growth rates were 4.7 nm / min and 21 nm / min for NPS at 575°C and 625°C and, 4.0 nm / min and 20 nm / min for disilane at 575°C and 625°C respectively.

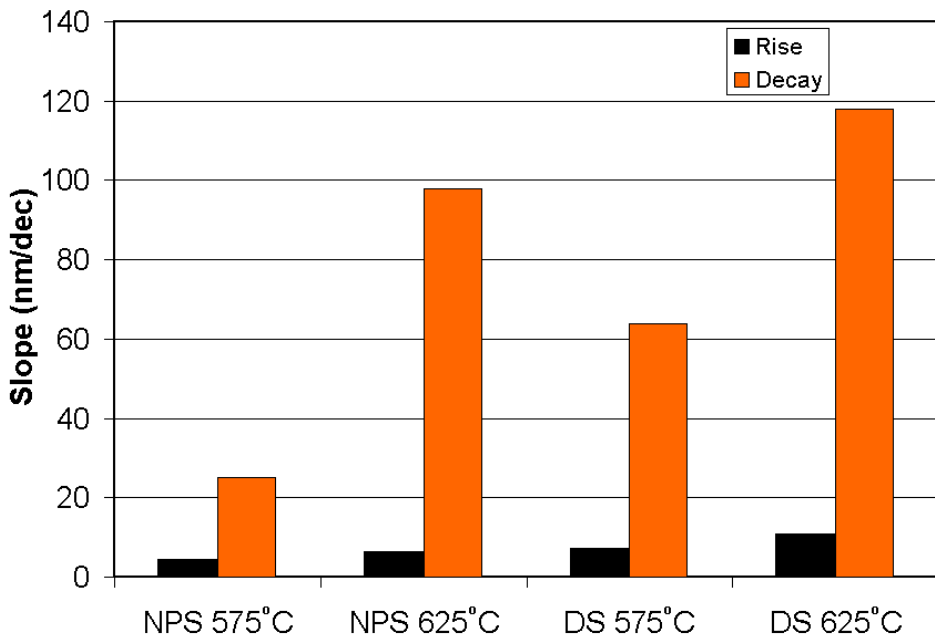


Figure 7.25. Rise and decay slopes as measured by SIMS for NPS and disilane at 575 °C and 625 °C respectively. The slopes were measured from samples 4850 (DS) and 4866 (NPS) (see Appendix E).

The smaller rise and decay slope of NPS when compared to disilane implies that NPS has a higher incorporation constant. Furthermore, both the rise and decay slope are smaller at lower temperatures for both gases, indicating that the phosphorus atoms on the surface are “freezing out” and do not have enough time to segregate at reduced temperatures. We do not know the reason why the slopes are reduced when NPS is used or why the rise and decay slopes are not the same.

7.6 Summary

In this chapter we have discussed the unwanted background concentration of phosphorus due to growth with DCS with SIMS and C-V measurements on Schottky diodes. A phenomenological model was made to model and to explain the phosphorus segregation trends that are commonly observed in from silicon and SiGe samples grown with our CVD system. Our phenomenological model was then compared with a microscopic model of how individual phosphorus adatoms are incorporated. Experimentally we found that low temperatures and high-growth rates can reduce surface segregation and hence increase phosphorus incorporation. This implies that high-order silanes should be used for growth of heavily phosphorus doped layers. Phosphorus doping experiments were conducted with different silicon precursors. We observed that high-order silanes are more efficient at incorporating phosphorous into the grown layers. This may be due to a freeze out effect, where the higher growth rate is preventing the surface segregation of phosphorus back to the surface.

Chapter 8

Summary and Conclusion

In this work, we have qualified the use of NPS as a silicon source in chemical vapor deposition. Characterization techniques such as (secondary ion mass spectrometry (SIMS), photoluminescence (PL), UV reflectance, and cross-sectional TEM) were conducted on epitaxial layers grown with NPS are analyzed and indicated that good quality epitaxial silicon layers can be grown with NPS. All deposition with NPS on oxide was found to be amorphous silicon. Etch rates of amorphous silicon layers are much higher than etch rates of crystalline silicon, implying that NPS is a suitable candidate for selective silicon deposition via a CDE (Cyclical Deposition and Etch) process. Field effect transistors (FETs) were fabricated in epitaxial layers grown with NPS. Based on carrier mobilities and curve-tracer plots we concluded that the quality of the epitaxial layers grown with NPS are comparable to the quality of epitaxial layers of prime grade silicon substrates.

The basic CVD silicon growth theory on a macroscopic, microscopic, and atomistic level was covered in this thesis. The conventional hydrogen desorption model of silicon growth was found to be inadequate in explaining high growth rates and low temperatures. Silicon growth with high-order silanes were significantly less dependent on conventional hydrogen desorption and qualitatively determined to generate its own open sites. A novel concerted reaction mechanism without the need for hydrogen desorption was proposed as the reason for the enhancement of growth rates with high-order silanes. This mechanism was supported by our experimental data using disilane and neopentasilane and by data from other groups using higher-order silanes such as trisilane. Smoother surfaces were also found with deposition from high-order silanes compared

with conventional silane under similar conditions, and can be explained by our novel model.

The ability of high-order silanes to deposit at low-temperatures and high-growth rates, makes them an attractive candidate for the epitaxial growth of dilute random carbon alloys of silicon (Si:C) and for heavily-doped-phosphorus layers in silicon. Higher substitutional carbon and phosphorus levels are achieved with NPS compared to silane and disilane under similar experimental conditions.

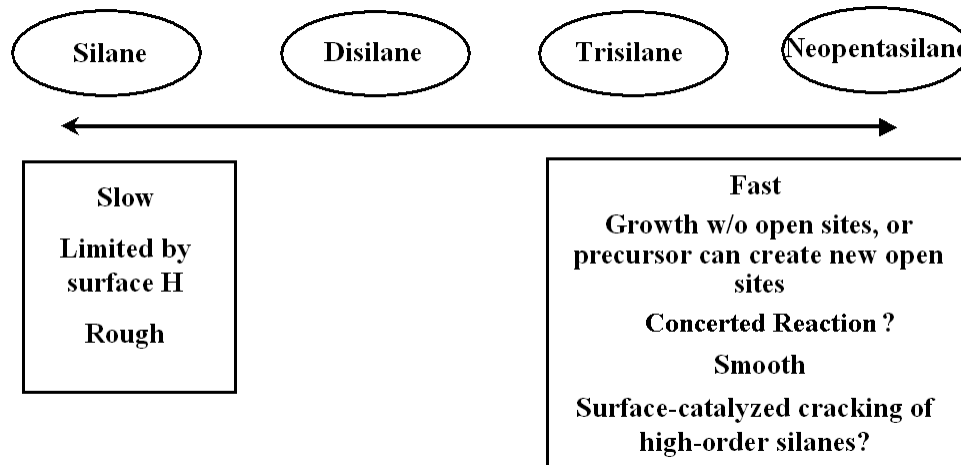


Figure 8.1 Synopsis of the effects of increasing the silane order. As the silane order is increased the growth rate increases and the smoothness of the deposited films improves.

List of References

Chapter 1 References

- [1.1] H. C. Theuerer, "Epitaxial Silicon Films by the Hydrogen Reduction of SiCl₄," *Journal of the Electrochemical Society*, v108, pp. 649-653 (1961)
- [1.2] B. D. Joyce and J. A. Baldrey, "Selective Epitaxial Deposition of Silicon," *Nature*, v195, pp. 485-486 (1962)
- [1.3] J. J. Lander and J. Morrison, "Low Voltage Electron Diffraction Study of the Oxidation and Reduction of Silicon," *Journal of Applied Physics*, v33, pp. 2089-2092 (1962)
- [1.4] R. H. Finch, H. J. Queisser, G. Thomas, and J. Washburn, "Structure and Origin of Stacking Faults in Epitaxial Silicon," *Journal of Applied Physics*, v34, pp. 406-415 (1963)
- [1.5] B. S. Meyerson, "Low-temperature Silicon Epitaxy by Ultrahigh Vacuum / Chemical Vapor Deposition", *Applied Physics Letters*, v48, pp. 797-799 (1986)
- [1.6] P. V. Schwartz and J. C. Sturm, "Oxygen Incorporation During Low Temperature Chemical Vapor Deposition Growth of Epitaxial Silicon Films," *Journal of the Electrochemical Society*, v141, pp. 1284-1290 (1994)
- [1.7] T. O. Sedgwick, M. Berkenblit, and T. S. Kuan, "Low-Temperature Selective Epitaxial Growth of Silicon at Atmospheric Pressure," *Applied Physics Letters*, v54, pp. 2689-2691 (1989)
- [1.8] R. People and J. C. Bean "Calculation of Critical Thickness versus Lattice Mismatch for Ge_xSi_{1-x} / Si Strained Heterostructures," *Applied Physics Letters*, v47, pp. 322-324 (August 1985)
- [1.9] "Properties of Silicon Germanium and SiGe: Carbon" Edited by E. Kasper and K. Lyutovich, pp. 22 (2000)

- [1.10] M. Yang, M. S. Carroll, J.C. Sturm, and T. Büyüklimanlı, “Phosphorus Doping and Sharp Profiles in Silicon and Silicon-Germanium Epitaxy by Rapid Thermal Chemical Vapor Deposition,” *Journal of the Electrochemical Society*, v147, pp. 3541-3545 (2000)
- [1.11] T. O. Mitchell, J. L. Hoyt, and J. F. Gibbons, “Substitutional Carbon Incorporation in Epitaxial $\text{Si}_{1-y}\text{C}_y$ Layers Grown by Chemical Vapor Deposition,” *Applied Physics Letters*, v71, pp. 1688-1690 (1997)

Chapter 2 References

- [2.1] J. C. Sturm, P. V. Schwartz, and P. M. Garone, “Silicon Temperature Measurement by Infrared Transmission for Rapid Thermal Processing Applications,” *Applied Physics Letters*, v56, pp. 961-964 (1990)
- [2.2] J. C. Sturm, P. M. Garone, and P. V. Schwartz, “Temperature Control of Silicon-Germanium Epitaxial Growth on Silicon Substrates by Infrared Transmission,” *Journal of Applied Physics*, v69, pp. 542-544 (1991)
- [2.3] J.C. Sturm and C. M. Reaves. “Silicon Temperature Measurement by Infrared Absorption Fundamental Processes and Doping Effects,” *IEEE Trans. Electron Dev.*, v39, pp. 81-88 (1992)
- [2.4] I. Vasiliev, S. Öğüt, and J. R. Chelikowsky, “*Ab Initio* Absorption Spectra and Optical Gaps in Nanocrystalline Silicon,” *Physical Review Letters*, v86, pp. 813-816 (Feb 2001)
- [2.5] Dow Chemical Phase Report
- [2.6] G. Pares, J. L. Regolini, J. Mercier, D. Dutartre, and D. Bensahel, “Kinetic Aspects of Epitaxial Silicon Growth using Disilane in a Rapid Thermal Processing System,” *Journal of Applied Physics*, v68, n9, pp. 4885-7 (Nov 1990)

- [2.7] Y. Suda, D. Lubben, T. Motooka, and J. E. Green, “Adsorption and Thermal Dissociation of Disilane (Si_2H_6) on Si(100) 2x1,” *Journal of Vacuum Science and Technology A*, **v8**, pp. 61-67 (1990)
- [2.8] M. A. Todd and K. D. Weeks, “Low Temperature, High Growth Rate Epitaxial Silicon and Silicon Germanium Alloy Films,” *Applied Surface Science*, **v224** pp. 41-45 (2004)
- [2.9] P. R. Fischer, M. Bauer, S. R. A. Van Averde, T. G. M. Oosterlaken, M. Yan, W. A. Verweij, B. W. M. Bozon, and P. M. Zagwijn, “Low Temperature Silcore ® Deposition of Undoped and Doped Silicon Films,” *ECS Transactions*, **v3**, pp. 203-215 (2006)
- [2.10] M. S. Carroll, J. C. Sturm, and M. Yang, “Low-Temperature Preparation of Oxygen- and Carbon-Free Silicon and Silicon Germanium Surfaces for Silicon and Silicon-Germanium Epitaxial Growth by Rapid Thermal Chemical Vapor Deposition,” *Journal of the Electrochemical Society*, **v147**, pp. 4652-4659 (2000)
- [2.11] M. Hierlemann, A. Kersh, C. Werner, and H. Schäfer, “A Gas-Phase and Surface Kinetics Model for Silicon Epitaxial Growth with SiH_2Cl_2 in an RTCVD Reactor,” *Journal of the Electrochemical Society*, **v142**, pp. 259-265 (1995)
- [2.12] D. W. Foster, A. J. Learn, and T. I. Kamins, “Deposition Properties of Silicon Films Formed from Silane in a Vertical-Flow Reactor,” *Journal of Vacuum Science and Technology B*, **v4**, pp. 1182-1186 (1986)
- [2.13] A. Yin and S. J. Fonash, “Oxygen-Plasma-Enhanced Crystallization of a-Si:H Films on Glass,” *Journal of Vacuum Science and Technology A*, **v12**, pp. 1237-1240 (1994)
- [2.14] G. Harbeke, L. Krausbauer, E. F. Steigmeier, and A. E. Widmer, “Growth and Physical Properties of LPCVD Polycrystalline Silicon Films,” *Journal of the Electrochemical Society*, **v131**, pp. 675-682 (1984)

- [2.15] T. I. Kamins, “Structure and Properties of LPCVD Silicon Films,” *Journal of the Electrochemical Society*, **v127**, pp. 686-690 (**1980**)
- [2.16] A. A. Onischuk and V. N. Panfilov, “Mechanism of Thermal Decomposition of Silanes,” *Russian Chemical Review*, **v70**, **n4**, pp. 321-332 (**2001**)

Chapter 3 References

- [3.1] D. J. Eaglesham, H.-J. Grossmann, and M. Cerullo, “Limiting Thickness h_{epi} for Epitaxial Growth and Room-Temperature Si Growth on Si (100),” *Physical Review Letters*, **v65**, **n10**, pp. 1227-1230 (**1990**)
- [3.2] H.-J. Grossmann, and L. C. Feldman, “Molecular Beam Epitaxy and Reconstructed Surfaces: Initial Stages of Interface Formation in Group IV-IV Structures,” *Applied Physics A*, **v38**, **n3**, pp. 171-179 (**1985**)
- [3.3] H. Jorke, H.-J. Herzog, and H. Kibbel, “Kinetics of Ordered Growth of Si on Si (100) at Low Temperatures,” *Physics Review B*, **v40**, pp. 2005-2008 (**1989**)
- [3.4] F. Jona, “Study of the Early Stages of the Epitaxy of Silicon on Silicon,” *Applied Physics Letters*, **v9**, **n6**, pp. 235-237 (**1966**)
- [3.5] K. Winer, “Theory of Infrared Absorption in Silicon,” *Physical Review B*, **v35**, **n15**, pp. 8189-95 (**May 1987**)
- [3.6] J. Weber and M. I. Alonso, “Near-Band-Gap Photoluminescence of Si-Ge Alloys”, *Physical Review B*, **v40**, **n8**, pp. 5683-5693 (**Sept. 1998**)
- [3.7] P. J. Dean, J. R. Haynes, and W. F. Flood, “New Radiative Recombination Processes Involving Neutral Donors and Acceptors in Silicon and Germanium”, *Physical Review*, **v161**, **n3**, pp. 711-729 (**Sept 1967**)
- [3.8] B. S. Meyerson, F. J. Himpsel, and K. J. Uram, “Bistable conditions for low-temperature silicon epitaxy,” *Applied Physics Letters*, **v57**, pp. 1034-1036 (**1990**)

- [3.9] M. S. Carroll, J. C. Sturm, and M. Yang, “Low-Temperature Preparation of Oxygen- and Carbon- Free Silicon and Silicon- Germanium Surfaces for Silicon and Silicon-Germanium Epitaxial Growth by Rapid Thermal Chemical Vapor Deposition,” *Journal of the Electrochemical Society*, **v147**, pp. 4652-4659 (**2000**)
- [3.10] S. M. Celik, and M. C. Öztürk, “Low Thermal Budget In Situ Surface Cleaning for Selective Silicon Epitaxy,” *Journal of the Electrochemical Society*, **v145**, pp. 3602-3608 (**1998**)
- [3.11] R. Oberhuber, G. Zandler, and P. Vogl, “Subband structure and mobility of two-dimensional holes in strained Si/SiGe MOSFET’s”, *Physics Review B*, **v58**, no **15**, pp. 9941-9948 (**1998-9**)

Chapter 4 References

- [4.1a] T. Kamins, *Polycrystalline Silicon for Integrated Circuits and Displays*, **Kluwer Academic Publishers, 2nd Edition**, pg 8
- [4.1b] L. I. Stiel and G. Thodos, “Viscosity of Hydrogen in the Gaseous and Liquid States for Temperatures up to 5000°K”, *Industrial Engineering Chemical Fundamentals*, **v2**, **n3**, pp. 233–237 (**1963**)
- [4.1c] Chemical Rubber Company (CRC). 1984. CRC Handbook of Chemistry and Physics. Weast, Robert C., Editor. **65th edition. CRC Press, Inc. Boca Raton, Florida. USA.**
- [4.2] D. J. Chadi, “Atomic and Electronic Structures of Reconstructed Si(100) Surfaces” *Physical Review Letters*, **v43**, **n1**, pp. 43-47 (**1979**)
- [4.3] J. A. Appelbaum, G. A. Baraff, D. R. Hamann, H. D. Hagstrum and T. Sakurai, “Hydrogen Chemisorption on the 100 (2 x 1) Surfaces of Si and Ge” *Surface Science*, **v70**, pp. 654-673 (**1978**)

- [4.4] S. Ciracri and I. P. Batra, “Theory of Transition from the Dihydride to Monohydride Phase on the Si(001) Surface” *Surface Science*, **v178**, pp. 80-89 (1986)
- [4.5] S. Ciracri, R. Butz, E. M. Oellig, and H. Wagner, “Chemisorption of hydrogen on the Si(100) Surface: Monohydride and Dihydride Phases” *Physical Review B*, **v30, n2**, pp. 711-720 (1984)
- [4.6] M. Kitabatake, P. Fons, and J. E. Greene, “Molecular Dynamics Simulations of Low-Energy Particle Bombardment Effects During Vapor Phase Crystal Growth: 10 eV Si Atoms Incident on Si(001) 2x1 Surface,” *Journal of Vacuum Science and Technology A*, **v8**, pp. 3726-3735 (1990)
- [4.7] K. Sinniah, M. G. Sherman, L. B. Lewis, W. H. Weinberg, J. T. Yates, Jr. and K. C. Janda, “New Mechanism for Hydrogen Desorption from Covalent Surfaces: The Monohydride Phase on Si (100),” *Physical Review Letters*, **v62, n5**, pp. 567-570 (Jan 1989)
- [4.8] M. C. Flowers, N. B. H. Jonathan, Y. Liu, and A. Morris, “Temperature Programmed Desorption of Molecular Hydrogen from a Si(100)-2x1 Surface: Theory and Experiment,” *Journal of Chemical Physics*, **v99, n9**, pp. 7038-7048 (July 1993)
- [4.9] P. V. Schwartz and J. C. Sturm, “Oxygen Incorporation During Low Temperature Chemical Vapor Deposition Growth of Epitaxial Silicon Films,” *Journal of the Electrochemical Society*, **v141, n5**, pp. 1284-1290 (May 1994)
- [4.10] J. B. Benziger, *Metal-Surface Reaction Energies*, **VCH Publishers**, New York (1991)
- [4.11] M. L. Hitchman, J. Kane, and A. E. Widmer, “Polysilicon Growth Kinetics in a Low Pressure Chemical Vapour Deposition Reactor,” *Thin Solid Films*, **v59**, pp. 231-247 (1979)

- [4.12] S. M. Gates, C. M. Greenlief, and D. B. Beach, “Decomposition Mechanisms of SiH_x species on Si(100)-(2x1) for x = 2, 3, and 4,” *Journal of Chemical Physics*, **v93, n10**, pp. 7493-7503 (**Nov 1990**)
- [4.13] I. Alkorta and J. Elguero, “Theoretical study of the bond energy in n-silanes and n-germanes: Comparison with n-alkanes”, *Chemical Physics Letters*, **v429**, pp. 58-61 (**2006**)
- [4.14] S.M. Gates and S.K. Kulkarni, “Kinetics of Surface Reactions of Very Low-Pressure Chemical Vapor Deposition of Si from SiH₄,” *Applied Physics Letters*, **v58, n25**, pp. 2964-2966 (**1991**)
- [4.15] S. M. Gates, “Adsorption Kinetics of SiH₄, Si₂H₆, and Si₃H₈ on the Si(111)-(7x7) Surface,” *Surface Science* **v195**, pp. 307-329 (**1988**)
- [4.16] Y. Suda, D. Lubben, T. Motooka, and J. E. Greene, “Adsorption and thermal dissociation of disilane (Si₂H₆) on Si (100) 2x1,” *Journal of Vacuum Science and Technology A*, **v8, n1**, pp. 61-67 (**1990**)
- [4.17] D.Lubben, R. Tsu, T. R. Bramlett, and J. E. Greene, “Mechanisms and kinetics of Si atomic-layer epitaxy on Si(001)2x1 from Si₂H₆,” *Journal of Vacuum. Science and Technology A*, **v9, n6**, pp. 3003-3011 (**1991**)
- [4.18] R.Imbihl, J. E. Demuth, S. M. Gates, and B. A. Scott, “Interaction of Si₂H₆ with a Si (111) – 7x7 surface,” *Physical Review B*, **v39**, pp. 5222-5233 (**March 1989**)
- [4.19] W. A. P. Claassen and J. Bloem, “The Growth of Silicon from Silane in Cold Wall CVD Systems,” *Phillips Journal of Research*, **v36**, pp. 123-137 (**1981**)
- [4.20] K. H. Chung, N. Yao, J. Benziger, J. C. Sturm, K. K. Singh, D. Carlson, and S. Kuppurao, “Ultrahigh Growth Rate of Epitaxial Silicon by Chemical Vapor Deposition at low Temperature with Neopentasilane,” *Applied Physics Letters*, **v92**, pp. 113506-8 (**March 2008**)
- [4.21] T. F. Narbeshuber, H. Vinek and J. A. Lercher, “Monomolecular Conversion of

- Light Alkanes over H-ZSM-5,” *J. Catalysis*, **v157**, pp. 388-395 (**1995**)
- [4.22] Y.V. Kissin, *Catalysis Reviews* **43**, pp. 85-146 (**2001**)
- [4.23] A. Farkas and K. Bonhoeffer, *Z. Phys. Chem.*, **231**, pp. 638-640 (**1931**)
- [4.24] S. D. Jackson, G. J. Kelly, and G. Webb, “Supported Metal Catalyst; Preparation, Characterization, and Function: Part VI. Hydrogenolysis of Ethane, Propane, n-Butane and iso-Butane over Supported Platinum Catalysts”, *Journal of Catalysis*, **v176**, pp. 225-234 (**1998**)
- [4.25] B. A. Ferguson, C. T. Reeves, D. J. Safarik, and C. B. Mullins, “Silicon Deposition from Disilane on Si(100)-2x1: Microscopic Model Including Adsorption,” *Journal of Applied Physics*, **v90**, pp. 4981-4989 (**2001**)
- [4.26] P. M. Agrawal, D. L. Thompson, and L. M. Raff, “Unimolecular Dissociation Dynamics of Disilane,” *Journal of Chemical Physics*, **v98**, pp. 1069-1082 (**1990**)
- [4.27] S. K. Kulkarni, S. M. Gates, C. M. Greenlief, and H. H. Sawin, “Mechanisms of Disilane Decomposition on Si(111)-7x7,” *Surface Science*, **v239**, pp. 26-35 (**1990**)
- [4.28] W. K. Burton, N. Cabrera, and F. C. Frank, “The Growth of Crystals and the Equilibrium Structures of Their Surfaces,” *Philosophical Transactions of the Royal Society of London, Series A. Mathematical and Physical Sciences*, **v243**, pp. 299-358 (**Nov. 1951**)
- [4.29] Z. Zhang, F. Wu, and M. G. Lagally, “An Atomistic View of Si(001) Homoepitaxy,” *Annual Reviews Materials Science*, **v27**, pp. 525-553 (**1997**)
- [4.30] D. J. Chadi, “Stabilities of Single-Layer and Bi-Layer Steps on Si(001) Surfaces,” *Physics Review Letters*, **v59**, pp. 1691-1694 (**1987**)
- [4.31] G. Brocks, P. J. Kelly, and R. Car, “Binding and Diffusion Energy of Si adatom on the Si(100) surface,” *Physics Review Letters*, **v66**, pp. 1729 (**1991**)
- [4.32] Y. W. Mo and M. G. Lagally, “Anisotropy in Surface Migration of Si and GE on Si(001),” *Surface Science*, **v248**, pp. 313-320 (**1991**)

- [4.33] B. Lewis and D. S. Campbell, “Nucleation and Initial-Growth Behavior of Thin-Film Deposits,” *Journal of Vacuum Science and Technology*, **v4**, pp. 209-218 (1967)
- [4.34] C. Pearson, M. Krueger, and E. Ganz, “Direct Tests of Microscopic Growth Models using Hot Scanning Tunneling Microscopy Movies,” *Physics Review Letters*, **v76**, pp. 2306-2309 (1996)
- [4.35] C Roland and G. H. Gilmer, “Epitaxy on Surfaces Vicinal to Si(001). I . Diffusion of Silicon Adatoms over Terraces,” *Physical Review B*, **v46**, pp. 13428-13436 (1992)
- [4.36] M. G. Lagally, *Kinetics of Ordering and Growth at Surfaces*, (Plenum, New York, 1989)
- [4.37] S. H. Wolff, S. Wagner, J. C. Bean, R. Hull, and J. M. Gibson, “Hydrogen Surface Coverage: Raising the Silicon Epitaxial Growth Temperature”, *Applied Physics Letters*, **v55**, pp. 2017-2019 (1989)
- [4.38] I. Mizushima, M. Koike, T. Sato, K. Miyano, and Y. Tsunashima, “Mechanism of Defect Formation During Low-Temperature Si Epitaxy on Clean Si Substrate”, *Japanese Journal of Applied Physics*, **v38**, pp. 2415-2418 (1999)
- [4.39] P. Meunier-Beillard, M. Caymax, K. Van Nieuwenhuysen, G. Doumen, B. Brijs, M. Hopstaken, L. Geenen, W. Vandervorst, “N₂ as Carrier Gas: An Alternative to H₂ for the Enhanced Epitaxy of Si, SiGe and SiGe:C”, *Applied Surface Science*, **v224**, pp. 31-35 (2004)
- [4.40] D.P. Adams and S. M. Yalisove, D. J. Eaglesham, “Effect of Hydrogen on Surface Roughening During Si Homoepitaxial Growth,” *Applied Physics Letters*, **v63**, n26, pp. 3571-3573 (1993)

- [4.41] J. W. Sharp and G. Eres, “Kinetics of Hydrogen Desorption From Si(100) and Si(111) Surfaces Following Chemisorption of Disilane and Trisilane,” *Surface Science*, **v320**, pp. 169-173 (**1994**)
- [4.42] M.P. D’Evelyn, Y. L. Yang, and L. F. Sutcu, “ π -Bonded Dimers, Preferential Pairing, and First-Order Desorption Kinetics of Hydrogen on Si(100)-(2x1),”, *Journal of Chemical Physics*, **v96**, **n1**, pp. 852-855 (**1996**)
- [4.43] M. L. Wise, B. G. Koehler, P. Gupta, P. A. Coon, and S. M. George, “Comparison of Hydrogen Desorption Kinetics from Si(111) 7 x 7 and Si(100) 2 x 1,” *Surface Science*, **v258**, pp. 166-176 (**1991**)
- [4.44] U. Höfer, L. Li, T. F. Heinz, “Desorption of Hydrogen from Si(100) 2 x 1 at Low Coverages: The Influence of π -Bonded Dimers on the Kinetics,” *Physical Review B*, **v45**, **n16**, pp. 9485-9488 (**1992**)
- [4.45] ASM Patent, WO 02/080244 (**10/10/2002**)
- [4.46] M. Bauer, V. Machkaoutsan, and C. Arena, “Highly Tensile Strained Silicon-Carbon Alloys Epitaxially Grown into Recessed Source Drain Areas of NMOS Devices,” *Semiconductor Science and Technology*, **v22**, pp. S183-187 (**2007**)
- [4.47] S. Takeuchi, N. D. Nguyen, J. Goosens, M. Caymax, R. Loo, “ $\text{Si}_{1-x}\text{Ge}_x$ Growth Using Si_3H_8 by Low Temperature Chemical Vapor Deposition,” *Thin Solid Films*, (**Oct 2009**), in press.
- [4.48] S. K. Kulkarni, S. M Gates, C. M. Greenlief, and H. H. Sawin, “Mechanisms of Disilane Decomposition on Si(111)-7x7,” *Surface Science*, **v239**, pp. 26-35 (**1990**)

Chapter 5 References

- [5.1] K. W. Ang, K. J. Chui, V. Bliznetsov, C. H. Tung, A Du, N. Balasubramanian, G. Samudra, M. F. Li, and Y. C. Yeo, “Lattice Strain Analysis of Transistor

- Structures with Silicon-Germanium and Silicon-Carbon Source / Drain Stressor," *Applied Physics Letters*, v86, pp. 093102-1- 093102-3 (2005)
- [5.2] Y. C. Yeo, "Enhancing CMOS Transistor Performance using Lattice-Mismatched Materials in Source / Drain Regions," *Semiconductor Science and Technology*, v22, pp. s177-s182 (2007)
- [5.3] P. A. Stolk, D. J. Eaglesham, H. – J. Gossman, and J. M. Poate, "Carbon Incorporation in Silicon for Suppressing Interstitial – Enhanced Boron Diffusion," *Applied Physics Letters*, v66, pp. 1370-1372 (1995)
- [5.4] H. Rücker, B. Heinemann, W. Röpke, R. Kurps, D. Krüger, G. Lippert, and H. J. Osten, "Suppressed Diffusion of Boron and Carbon in Carbon-Rich Silicon," *Applied Physics Letters*, v73, pp. 1682-1685 (1998)
- [5.5] R. F. Scholz, P. Werner, U. Gösele, and T. Y. Tan, "The Contribution of Vacancies to Carbon Out-Diffusion in Silicon," *Applied Physics Letters*, v74, pp. 392-395 (1999)
- [5.6] G. Davies and R.C. Newman, "Carbon in Monocrystalline Silicon," in *Handbook on Semiconductors*, T.S. Moss, pp. 1558 Ed. 1994
- [5.7] A. R. Bean and R. C. Newman, "The Solubility of Carbon in Pulled Silicon Crystals" *Journal Physical Chemical Solids*, v32, pp. 1211-1219 (1971)
- [5.8] C. A. Londos, "Deep-level Transient Spectroscopy Studies of the Interstitial Carbon Defect in Silicon," *Physical Review B*, v35, pp. 6295-6297 (1987)
- [5.9] T. O. Mitchell, J. L. Hoyt, and J. F. Gibbons, "Substitutional Carbon Incorporation in Epitaxial Si_{1-y}C_y Layers Grown by Chemical Vapor Deposition," *Applied Physics Letters*, v71, pp. 1688-1690 (1997)
- [5.10] H. J. Osten, "Substitutional versus Interstitial Carbon Incorporation During Pseudomorphic Growth of Si_{1-y}C_y on Si(001)," *Journal of Applied Physics.*, v80, pp. 6711-6715 (1996)

- [5.11] J. L. Hoyt, T. O. Mitchell, K. Rim, D. V. Singh, and J. F. Gibbons, “Comparison of Si/Si_{1-x-y}Ge_xC_y and Si/Si_{1-y}C_y Heterojunctions Grown by Rapid Thermal Chemical Vapor Deposition” *Thin Solid Films*, v321, pp. 41-46 (1998)
- [5.12] H. J. Osten, “MBE Growth and Properties of Supersaturated, Carbon-Containing Silicon / Germanium Alloys on Si(001),” *Thin Solid Films*, v367, pp. 101-111 (2000)
- [5.13] P. C. Kelires, E. Kaxiras, “Substitutional Carbon Impurities in Thin Silicon Films: Equilibrium Structure and Properties,” *Journal of Vacuum Science and Technology B*, v16, pp. 1687-1691 (1998)
- [5.14] J. M. Hartmann, T. Ernst, F. Ducroquet, G. Rolland, D. Lafond, A-M. Papon, R. Truche, P. Holliger, F. Laugier, M. N. Semeria, and S. Deleonibus, “High C Content Si/Si_{1-y}C_y Heterostructures for n-type Metal Oxide Semiconductors Transistors,” *Semiconductor Science and Technology*, v19, pp. 593-601 (2004)
- [5.15] D. De Salvador, M. Petrovich, M. Berti, F. Romanato, E. Napolitani, A. Drigo, J. Stangl, S. Zerlauth, M. Mühlberger, F. Schäffler, G. Bauer, and P. C. Kelires,” *Physical Review B*, v61, pp. 13005-13013 (2000)
- [5.16] P. C. Kelires, “Short-Range Order, Bulk Moduli, and Physical Trends in c-Si_{1-x}C_x Alloys,” *Physical Review B*, v55, pp. 8784-8787 (1997)
- [5.17] P. Lavéant, G. Gerth, P. Werner, U. Gösele, “Epitaxy of Carbon-Rich Silicon with MBE,” *Materials Science and Engineering B*, v89, pp. 241-245 (2002)
- [5.18] J. C. Bean, L. C. Feldman, A. T. Fiory, S. Nakahara, I. K. Robinson, “Ge_xSi_{1-x} / Si Strained-Layer Superlattice Grown by Molecular Beam Epitaxy,” *Journal of Vacuum Science and Technology A*, v2, pp. 436- 440 (1984)
- [5.19] Malcolm Carroll, Ph. D. Thesis, *Princeton University*, 2001
- [5.20] J. L. Hoyt, in *Silicon Germanium Carbon Alloys*, edited by S. T. Pantelides and S. Zollner, pp. 59-89 (**Taylor & Francis, New York, 2002**),

- [5.21] M. Bauer, V. Machkaoutsan, C. Arena, “Highly Tensile Strained Silicon-Carbon Alloys Epitaxially Grown Into Recessed Source Drain Areas of NMOS Devices,” *Semiconductor Science and Technology*, v22, n1, pp. S183-S187 (2007)
- [5.22] A. C. Mocuta, and D. W. Greve, “Epitaxial Si_{1-y}C_y Alloys: The Role of Surface and Gas Phase Reactions,” *Journal of Applied Physics*, v85, n2, pp. 1240-1242 (1999)
- [5.23] F. Hirose and H. Sakamoto, “Desorption Rate of Surface Hydrogen in SiGe Gas-Source Molecular Beam Epitaxy using Si₂H₆ and GeH₄,” *Journal of Vacuum Science and Technology A*, v16, n5, pp. 2974-2978 (1998)
- [5.24] B. S. Meyerson, K. J. Uram, and F. K. LeGouse, “Cooperative Growth Phenomena in Silicon/Germanium Low-Temperature Epitaxy,” *Applied Physics Letters*, v53, n25, pp. 2555-2557 (1988)
- [5.25] M. Oehme, M. Bauer, C. P. Parry, G. Eifler, E. Kasper, “Carbon Segregation in Silicon,” *Thin Solid Films*, v380, pp. 75-77 (2000)
- [5.26] Eric Stewart, Ph. D. Thesis, *Princeton University*, 2004

Chapter 6 References

- [6.1] E.G. Alexander and W.R. Runyan, *Trans. Metl. Soc.*, AIME 236, pp. 284 (1966)
- [6.2] B. S. Meyerson, F. J. Himpsel, and K. J. Uram, “Bistable Conditions for Low-Temperature Silicon Epitaxy,” *Applied Physics Letters*, v57 pp. 1034-1036 (1990)
- [6.3] M. K. Sanganeria, M. C. Öztürk, and K. E. Violette, “Low Thermal Budget *In Situ* Removal of Oxygen and Carbon on Silicon for Silicon Epitaxy in an Ultrahigh Vacuum Rapid Thermal Chemical Vapor Deposition Reactor,” *Applied Physics Letters*, v66, pp. 1255-1257 (1995)
- [6.4] M. S. Carroll, J. C. Sturm, and M. Yang, “Low-Temperature Preparation of Oxygen- and Carbon- Free Silicon and Silicon- Germanium Surfaces for Silicon

- and Silicon-Germanium Epitaxial Growth by Rapid Thermal Chemical Vapor Deposition," *Journal of the Electrochemical Society*, v147, pp. 4652-4659 (2000)
- [6.5] S. M. Celik, and M. C. Öztürk, "Low Thermal Budget In Situ Surface Cleaning for Selective Silicon Epitaxy," *Journal of the Electrochemical Society*, v145, pp. 3602-3608 (1998)
- [6.6] Y. Bogumilowicz, J. M. Hartmann, R. Truche, Y. Campidelli, G. Rolland, and T. Billon, "Chemical Vapour Etching of Si, SiGe and Ge with HCl; Applications to the Formation of Thin Relaxed SiGe Buffers and to the Revelation of Threading Dislocations," *Semiconductor Science and Technology*, v20, pp. 127-134 (2005)
- [6.7] K. E. Violette, P. A. O'Neil, M. C. Ozturk, K. Christensen, and D. M. Maher, "On the Role of Chlorine in Selective Silicon Epitaxy by Chemical Vapor Deposition," *Journal of the Electrochemical Society*, v143, pp. 3290-3296 (1996)
- [6.8] J. P. Dismukes and R. Ulmer, "Gas-Phase Etching of Silicon with Chlorine," *Journal of the Electrochemical Society: Solid State Science*, pp. 634-636 (1971)
- [6.9] K.H. Chung, J.C. Sturm, E. Sanchez, K.K. Singh, and S. Kuppurao, "The High Growth Rate of Epitaxial Silicon-Carbon Alloys by Using Chemical Vapour Deposition and Neopentasilane" *Semiconductor Science and Technology*, v22, n1, pp. S158-60 (Jan 2007)
- [6.10] M. A. Todd and K. D. Weeks, "Low Temperature, High Growth Rate Epitaxial Silicon and Silicon Germanium Alloy Films," *Applied Surface Science*, v224, pp. 41-45 (2004)
- [6.11] M. Liehr, M. Offenberg, S.R. Kasi, G.W. Rubloff, and K.Holloway, p1099 of Extended Abstracts of the 22nd Conference on Solid State Devices and Materials, Sendai (1990)

- [6.12] Y. Tsukidate, and M. Suemitsu, “Growth Kinetics and Doping Mechanism in Phosphorus-Doped Si Gas-Source Molecular Beam Epitaxy,” *Applied Surface Science*, **v175-176**, pp. 43-48 (2001)
- [6.13] Y. Wang, X. Chen, and R. J. Hamers, “Atomic-Resolution Study of Overlayer Formation and Interfacial Mixing in the Interaction of Phosphorus with Si(001),” *Physical Review B*, **v50, n7**, pp. 4534-4547 (1994)
- [6.14] M Yang, M. Carroll, J. C. Sturm, and T. Büyüklimanlı, “Phosphorus Doping and Sharp Profiles in Silicon and Silicon-Germanium Epitaxy by Rapid Thermal Chemical Vapor Deposition,” *Journal of the Electrochemical Society*, **v147, n9**, pp. 3541-3545 (2000)
- [6.15] S-M. Jang, K. Liao, and R. Rief, “Phosphorus Doping of Epitaxial Si and $\text{Si}_{1-x}\text{Ge}_x$ at Very Low Pressure,” *Applied Physics Letters*, **v63, n12**, pp. 1675-1677 (1993)
- [6.16] J. M. Hartmann, L. Clavelier, C. Jahan, P. Holliger, G. Rolland, T. Billon, and C. Defranoux, “Selective Epitaxial Growth of Boron- and Phosphorus- Doped Si and SiGe for Raised Sources and Drains,” *Journal of Crystal Growth*, **v264**, pp. 36-47 (2004)
- [6.17] J. Murota, N. Nakamura, M. Kato, and N. Mikoshiba, T. Ohmi, “Low-Temperature Silicon Selective Deposition and Epitaxy on Silicon Using the Thermal Decomposition of Silane Under Ultraclean Environment”, *Applied Physics Letters*, **v54, n11**, pp. 1007-1009 (March 1989)

Chapter 7 References

- [7.1] P. J. Roksnoer, J. W. F. M. Maes, A. T. Vink, C. J. Vriezema, and P. C. Zalm, “Sharp Boron Spikes in Silicon Grown by Fast Gas Switching Chemical Vapor Deposition,” *Applied Physics Letters*, **v58**, pp. 711-713 (1990)

- [7.2] A. J. Learn and D. W. Foster, “Deposition and Electrical Properties of In-Situ Phosphorus-Doped Silicon Films Formed by Low-Pressure Chemical Vapor Deposition,” *Journal of Applied Physics*, **v61**, n5, pp. 1898-1904 (**March 1987**)
- [7.3] B. S. Meyerson and W. Olbricht, “Phosphorus-Doped Polycrystalline Silicon via LPCVD,” *Journal of the Electrochemical Society*, **v131**, n10, pp. 2361-2365 (**1984**)
- [7.4] M. M. Mandurah, K. C. Saraswat, R. C. Helms, and T. I. Kamins, “Dopant Segregation in Polysilicon,” *Journal of Applied Physics*, **v51**, n11, pp. 5755-5763 (**1980**)
- [7.5] L. J. Giling and J. Bloem, “The Incorporation of Phosphorus in Silicon; The Temperature Dependence of the Segregation Coefficient,” *Journal of Crystal Growth*, **v31**, pp. 317-322 (**1975**)
- [7.6] J. F. Nützel, M. Holzmann, P. Schittenhelm, and G. Abstreiter, “Segregation of n-Dopants on SiGe Surfaces,” *Applied Surface Science*, **v102**, pp. 98-101 (**1996**)
- [7.7] Wibo van Noort, Ph.D. Thesis
- [7.8] M. Yang, M. Carroll, J. C. Sturm, and T. Büyüklimanlı, “Phosphorus Doping and Sharp Profiles in Silicon and Silicon-Germanium Epitaxy by Rapid Thermal Chemical Vapor Deposition,” *Journal of the Electrochemical Society*, **v147**, pp. 3541-3545 (**2000**)
- [7.9] S.M. Sze, *VLSI Technology* (**1988**)
- [7.10] J. F. Nützel and G. Abstreiter, “Segregation and Diffusion on Semiconductor Surfaces,” *Physical Review B*, **v53**, n20, pp. 551-557 (**1996**)
- [7.11] Y. Wang, X. Chen, and R. J. Hamers, “Atomic-Resolution Study of Overlayer Formation and Interfacial Mixing in the Interaction of Phosphorus with Si(001),” *Physical Review B*, **v50**, n7, pp. 4534-4557 (**Aug 1994**)

- [7.12] L. Kipp, R. D. Bringans, D. K. Biegelsen, J. E. Northrup, A. Garcia, and L.-E. Swartz," *Physical Review B*, **v52, n8**, pp. 5843-5859 (**Aug 1995**)
- [7.13] E Suvar, H. H. Radamson, and J. V. Grahn, "Phosphorus Profile Control in Low-Temperature Silicon Epitaxy by Reduced Pressure Chemical Vapor Deposition," *Material Science and Engineering B*, **v89**, pp. 314-318 (**2002**)
- [7.14] Min Yang, Ph. D. Thesis, *Princeton University*, **2000**

Appendix A

List of Publications and Presentations Resulting from This Thesis

Under Review:

- [1] K.H. Chung, J. C. Sturm, K. K. Singh, D. Carlson, and S. Kuppurao, "MOSFET Performance in Epitaxial Silicon Layers Grown by Ultra-High Growth Rate Chemical Vapor Deposition with Neopentasilane," Submitted- *Journal of Materials Research*

Published:

- [1] K. H. Chung, N. Yao, J. Benziger, J. C. Sturm, K. K. Singh, D. Carlson, and S. Kuppurao, "Ultrahigh Growth Rate of Eitaxial Silicon by Chemical Vapor Deposition at Low Temperature with Neopentasilane," *Applied Physics Letters*, **v92**, pp 113506-8 (**March 2008**)
- [2] J.C. Sturm, K. H. Chung, N. Yao, E. Sanchez, K. K. Singh, and S. Kuppurao, "Chemical Vapor Deposition Epitaxy of Silicon and Silicon-Carbon Alloys at High Rates and Low Temperatures Using Neopentasilane," *ECS Transactions*, **v6**, **n1**, pp 429-436 (**May 2007**)
- [3] K. H. Chung and J. C. Sturm, "Chlorine Etching for In-Situ Low Temperature Silicon Surface Cleaning for Epitaxial Applications," *ECS transactions*, **v6**, **n1**, pp 401-407 (**May 2007**)
- [4] K. H. Chung, J. C. Sturm, E. Sanchez, K. K. Singh, and S. Kuppurao, "The High Growth Rate of Epitaxial Silicon-Carbon Alloys by Using Chemical Vapour Deposition and Neopentasilane," *Semiconductor Science and Technology*, **v22**, **n1**, pp S158-60 (**Jan 2007**)

List of Presentations:

- [6] K. H. Chung, N. Yao, J. C. Sturm, D. Carlson, K. K. Singh, and S. Kuppurao, “Ultra-High Growth Rate of Epitaxial Silicon by Chemical Vapor Deposition at Low Temperature with a Novel Precursor,” **Materials Research Symposium, April 2006**
- [7] K. H. Chung, J. C. Sturm, E. Sanchez, K. K. Singh, and S. Kuppurao, “High Growth Rate of Epitaxial Silicon-Carbon Alloys by High-Order Silane Precursor and Chemical Vapor Deposition,” **International SiGe Technology and Device Meeting (ISTDM), May 2006**
- [8] K. H. Chung, J. C. Sturm, D. Carlson, K. K. Singh, and S. Kuppurao, “FET Mobilities in Layers Grown by Ultra-High Growth Rate CVD with High-Order Silane Precursor,” **Electronic Materials Conference, June 2006**
- [9] K. H. Chung and J. C. Sturm, “Chlorine Etching For In-Situ Low-Temperature Silicon Surface Cleaning For Epitaxy Applications”, **Electrical Chemical Society, June 2007**
- [10] J. C. Sturm, K. H. Chung, N. Yao, E. Sanchez, K.K. Singh, and S. Kuppurao, “Chemical Vapor Deposition Epitaxy of Silicon and Silicon-Carbon Alloys at High Rates and Low Temperatures Using Neopentasilane” **Electrical Chemical Society, June 2007**
- [11] J. C. Sturm and K. H. Chung, “Chemical Vapor Deposition Epitaxy of Silicon-based Materials using Neopentasilane”, **Electrical Chemical Society, Oct. 2008**
- [12] K. H. Chung and J. C. Sturm, “Smooth Silicon Surfaces at Ultra-High Growth Rates by Low Temperature CVD Epitaxy with High-Order Silanes”, **ICSI-6: 6th International Conference on Silicon Epitaxy and Heterostructures, May 2009**

- [13] K. H Chung and J. C. Sturm, “Impact of High Order Silane Precursors for Silicon Epitaxial Growth on Surface Open Sites”, **Electronic Materials Conference, June 2009**

Appendix B

Modifications to the Princeton RTCVD for Neopentasilane, HCl / Chlorine Sources

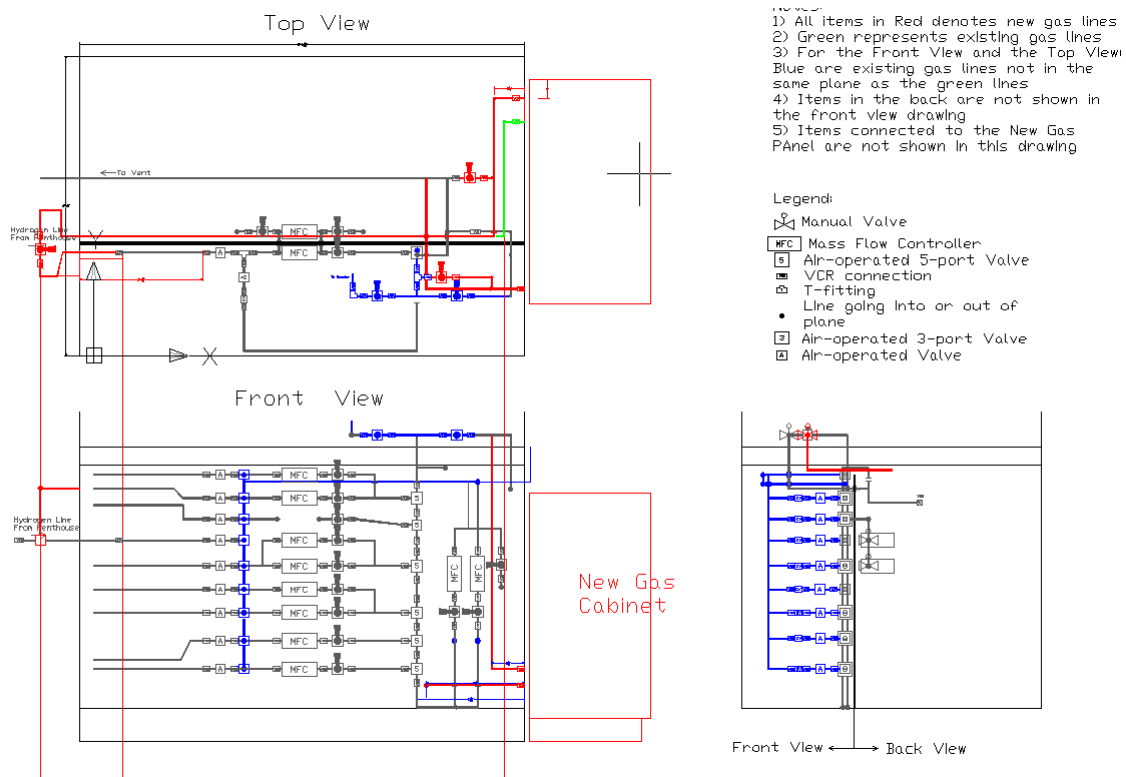


Figure B1. Top view, front view, and side view of modifications to the Princeton RTCVD. Shown in red are the changes made to the existing gas delivery system to accommodate for NPS.

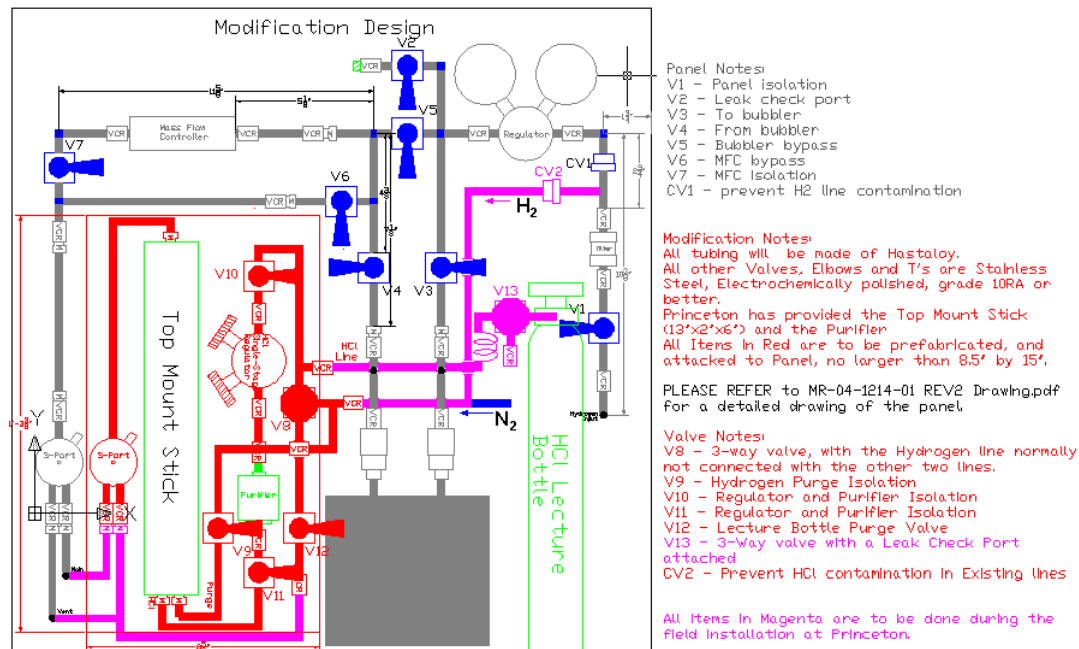


Figure B2. Schematic of components inside the NPS cabinet. Shown in gray is the original delivery system for NPS, shown in chapter 2. In red and pink are the appended gas delivery system for lecture bottles. Due to lack of space in the diagram not shown are nitrogen and hydrogen manual valves to prevent cross contamination between the two lines. The location of the hydrogen chloride (HCl) lecture bottle is also shown. Sometimes a chlorine bottle was used in this location.

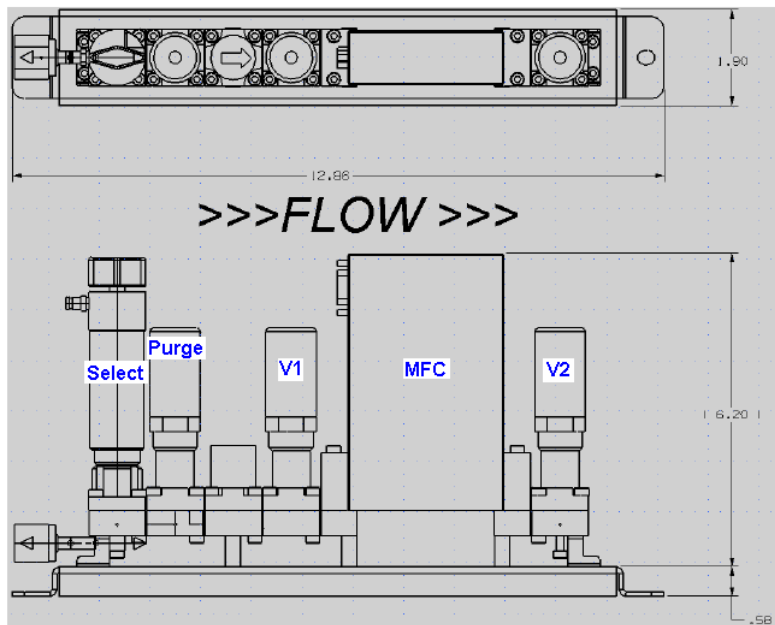


Figure B3. Top and side view of Top Mount Stick. Shown in the side view of the diagram are the HCl select valve (labeled Select), V1 and V2, and the HCl purge valve (labeled Purge) along with HCl MFC.

Functional Description of NPS Gas Panel:

The NPS gas panel is designed to allow for the flow of hydrogen either into the NPS ampule or bypassing the NPS ampule. The hydrogen line to the NPS cabinet is teed-off from the main hydrogen after the hydrogen purifier (see Figure B1). The **Regulator** is used to control the pressure hydrogen going directly into the NPS ampule. This value is typically set at 0 psig. A check valve (**CV1**) is to prevent the backflow of NPS into the hydrogen line. **V2** is the leak check port for the gas panel. **V6** is the **NPS MFC** bypass value.

The hydrogen flows is as follows:

V1 (NPS panel) => **Filter** => **CV1** => **Regulator** => Either **V5** or (**V3 =>NPS Ampule =>V4**) => **NPS MFC** => **V7** => RTCVD Chamber **Main** or **Vent** (3-port valve).

The **NPS MFC** is calibrated for DCS, so a calibration factor of 0.434 is used. The range of the MFC is 300 sccm of DCS. A setting of 0.434 on the MFC corresponds to 300 sccm of hydrogen.

NPS Gas Flow and NPS Panel Purge Instructions

Gas Flow

- [1] Before any gas panel usage, follow the standard RTCVD startup procedure and verify that the reactor and the **Burnbox** are in operational status with hydrogen flowing (MFC =0.1) through the main chamber. All manual valves in the cabinet should be closed.
- [2] Flow hydrogen gas from the NPS panel by doing the following:
 - [2a] Open the **Vent Valve**, then open the **Cabinet Vent Valve** shown connected to the vent line in the top view of Figure B1 above.
 - [2b] In DAQ Factory, set the **NPS MFC** to 1. Open **V1**, **V5**, and **V7**. The chamber pressure reading should be 1.6 torr. Fully open the regulator to flush the NPS lines. Toggle **NPS Inject** (DAQ factory) to flush the NPS line to the RTCVD chamber.
 - [2c] Adjust the **NPS MFC** to your target gas flow (i.e.0.72 for 50 sccm of NPS in hydrogen). Then adjust the regulator till the outlet pressure of the regulator reads ~0 psig
- [3] To flow NPS instead of hydrogen:
 - [3a] Leave **V5** open and then open **V4**, wait for the pressure to stabilize

- [3b] Open **V3**, then open the **Outlet Ampule Valve** (Not shown in Figure B2) and then open the **Inlet Ampule Valve**
- [3c] Close **V5** (Due to the temporary clogging of the **NPS MFC** this step is not done until 5 minutes before the **NPS Inject** in your recipe.
- [4] You are now ready to run your recipe!
- [5] When your recipe is complete close the two **NPS Ampule Valves**

Gas Purge

- [6] Flush the lines with hydrogen after completion of recipe
 - [6a] Verify step [1] and verify that the **NPS Ampule Valves** are both closed.(NPS gas panel manual values do not have to be closed)
 - [6b] Set **NPS MFC** to 1 and then open the manual valve shown connected to the vent line in the top view of Figure B1 above.
 - [6c] Open **V1, V4, V7** and fully open the **Regulator**
 - [6d] Open **V2** and **V3**, then close **V1**
 - [6e] When **Regulator** reading is <-30 mmHg close **V2** and **V3**
 - [6f] Cycle Steps 6c to 6e, 10 times
- [7] When the purge is complete, reduce **Regulator** so that the outlet pressure reads 20 psig
- [8] Close **V7**, then close **V1** and **V4**, and follow standard RTCVD shutdown procedures
- [9] The next morning check the Regulator pressure (If it still reads 20 psig then there is no leak) to see if there are any leaks in the NPS panel

Functional Description of Lecture Bottle Gas Panel:

The gas panel modification above is designed to inject the contents from a lecture bottle (shown in green in Figure B2 above) into the existing reactor chamber via the use of top mount (aka surface mount) technology to minimize the use of space. The lecture bottle can be either HCl or Chlorine gas. The line connection to the lecture bottle is a **CGA 660** fitting. The components of the Top Mount Stick are shown in Figure B3 above. All of the valves on the surface mount are pneumatic valves, and are controlled by the DAQ factory program. **V1** and **V2** are tied together and called **HCl V1** in the DAQ factory program. **HCl Purge** is the purge valve for the Top mount stick, and can flow either N₂ or H₂ gas. **HCl Select** is a manual and pneumatic valve, where the valve is opened only when both the manual and pneumatic valve is opened (See the top view of the select valve). The **HCl MFC** is a 300sccm MFC with a 9-pin connection.

Lecture Bottle Gas Flow Instructions:

- [1] Before any lecture bottle usage, follow the standard RTCVD startup procedure and verify that the reactor and the **Burnbox** are in operational status with hydrogen flowing (MFC =0.1) through the main chamber. All manual valves in the cabinet should be closed.
- [2] Open the Tank valve to the lecture bottle.
- [3] Verify that **V13** and **V8** are closed (i.e. the T-direction of the 3-way valve is closed. Open **V10** and **V11**.
- [4] Open the either the nitrogen or hydrogen manual valve (Open only one NOT both!) on the panel to enable either N₂ or H₂ flow into the HCl line. Open **V9**.
- [5] Flow gas from the lecture bottle by doing the following:
 - [5a] Open the **Vent Valve**, then open the **Cabinet Vent Valve** shown connected to the vent line in the top view of Figure B1 above.
 - [5b] In DAQ Factory, set the **HCl MFC** to 1, then open **HCl V1** and **HCl V2** in the program. This will now flow H₂ or N₂ through the Top Mount Stick and out to the vent line. The reactor pressure should be around 1.10 torr.
 - [5c] In DAQ Factory, click **HCl Select** (the line is now flowing HCl through the Top Mount Stick up to V11). HCl is now flowing to vent.
- [6] Turn off **HCl Select**, so that H₂ or N₂ is flowing through the Top Mount Stick
- [7] You are now ready to run your recipe!

Lecture Bottle Change Instructions:

- [1] Before any lecture bottle usage, follow the standard RTCVD startup procedure and verify that the reactor and the **Burnbox** are in operational status with hydrogen flowing (MFC =0.1) through the main chamber. All manual valves in the cabinet should be closed.
- [2] Close the Tank valve to the lecture bottle.
- [3] Verify that **V13** and **V8** are closed (i.e. the T-direction of the 3-way valve is closed. Also verify that **V10** and **V11** are closed.
- [4] Open the either the nitrogen or hydrogen manual valve (Open only one NOT both!) on the panel to enable either N₂ or H₂ flow into the HCl line. Open **V9**.
- [5] Open the **Vent Valve**, then open the **Cabinet Vent Valve** shown connected to the vent line in the top view of figure B1 above.
- [6] Open **V12** slowly, this will directly pump out the HCl in the line up to the lecture bottle out through the vent, and pump out up to **V10** on the other side of the line.
- [7] When the RTCVD pressure reading is back down to 0.7, closed **V12**
- [8] Open **V8**, the line is now pressurized with N₂
- [9] Close **V8**
- [10] Cycle Steps 6-9 for 50 times.
- [11] Open **V8** so that the line is pressurized with N₂
- [12] Close **V8**, change **Lecture Bottle** then cycle steps 6-9 for 50 times.
- [13] Leak check the new bottle by installing the leak checker onto the 3-port of **V13**
- [14] Open **V13** to leak check
- [15] If the leak check is successful, cycle purge and flush the lines with N₂ thoroughly before opening the lecture bottle.

Appendix C

Hydrogen Desorption

This section is to explain hydrogen desorption in more detail. There are two types of hydrogen desorption, called β_1 (monohydride), and β_2 (dihydride) desorption. At roughly 400°C (673°K) dihydride desorption occurs, and the silicon surface transitions from a dihydride surface (Si: 1x1) reconstruction, with 2 hydrogen atoms per surface silicon atom to a monohydride surface (one hydrogen atom per silicon surface atom). The surface silicon atom now has an empty bond that will pair with its nearest neighbor reconstructing the silicon surface into a Si: 2x1 surface. Monohydride desorption occurs around 510°C (783°K), at temperatures higher than 510°C all of the hydrogen on the surface will desorb and the surface will be a perfect 2x1 reconstruction. The β_1 and β_2 peaks are shown in Figure C1 below:

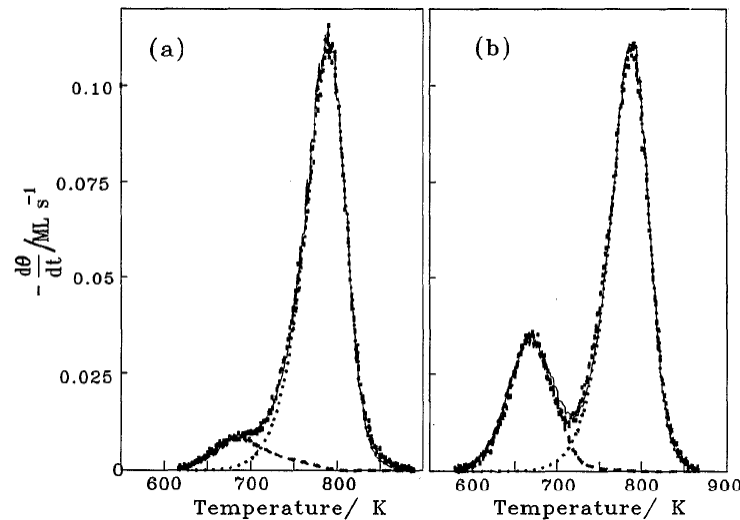


Figure C1. Experimental and fitted TPD spectra of D₂ from Si(001) surfaces initially dosed with (a) 1.09 and (b) 1.31 ML atomic deuterium [4.8].

Both the experimental (circles) and fitted (dashed line) TPD spectra of deuterium are shown. Note that in (b) of figure C1, the β_2 peak is higher as there are more dihydride phases on the silicon lattice than in (a). The monohydride peak is also higher than the

dihydride peak. Dihydride desorption is a second-order process and occurs by desorption of the two surface hydrogen atoms, attached to a lone silicon surface atom, to form H₂ [4.8].

Monohydride hydrogen desorption is a first order process at high surface coverages ($\theta_H \sim 1$), and a second order process at low coverages ($\theta_H < 0.1$). In Figure C2 below we show the different configurations of hydrogen on the 2x1 reconstructed silicon surface.

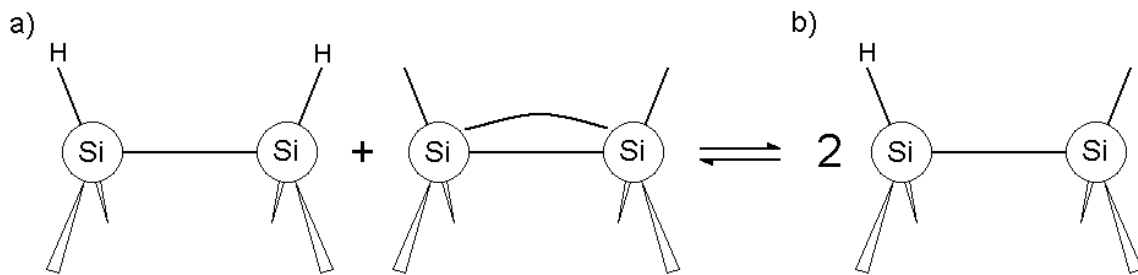


Figure C2. Schematic of a doubly occupied dimer and unoccupied dimer (a) and two singly occupied dimers (b) of silicon atoms on the surface of Si(100) 2x1. The unoccupied silicon dimer forms a partial double bond. [4.42]

Two surface hydrogen atoms on the surface can take either of the two configurations. It can form a doubly occupied dimer and an unoccupied dimer (2 two open surface sites) or two singly occupied dimers. It was determined that a small pairing energy of 0.25eV [4.44] causes the two surface hydrogen atoms to take configuration (a) instead of (b). At high surface coverages ($\theta_H \sim 1$), almost all hydrogen atoms are preferentially paired, whereas at low coverages ($\theta_H < 0.1$), more of configuration (b) is observed. This makes hydrogen desorption a first order process at high θ_H and a second-order process at low θ_H . In our typical CVD conditions (600°C, 6 torr hydrogen), the surface is expected to be monohydride and the desorption is first order.

Appendix D

Terrace-Step-Kink Model

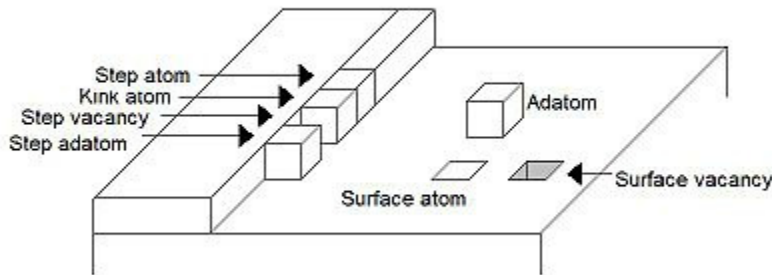


Figure D1. Schematic showing the different positions of an adatom, based on the Terrace-Step-Kink Model for a simple cubic lattice. Picture taken from Wikipedia.com.

The Terrace-Step-Kink model is based upon the idea that position of an adatom on the crystal surface is determined by its bonding to neighboring atoms and that transitions simply involve the counting of broken and formed bonds. Below is a table of the possible positions of an adatom and the number of broken bonds and formed bonds for each position.

Table D1: Possible positions of the adatom and the number of broken and formed bonds for a simple cubic lattice based on Figure D1.

	# of Broken Bonds	# of Formed Bonds
Adatom	5	1
Step Adatom	4	2
Kink Atom	3	3
Step Atom	2	4
Surface Atom	1	5

The adatom diffuses on the surface to minimize its energy by landing on the step, kink or onto the (sub)surface. Based on table D1, we find that the adatom would want to diffuse to the steps if possible. However if another adatom landed on top of the diffusing adatom,

it would become less mobile due to the lowered energy from having more bonds. The silicon surface is not cubic, but it is expected that the concepts of the model could be extended to the silicon surface.

Appendix E

SIMS Sample 4850 and Sample 4866

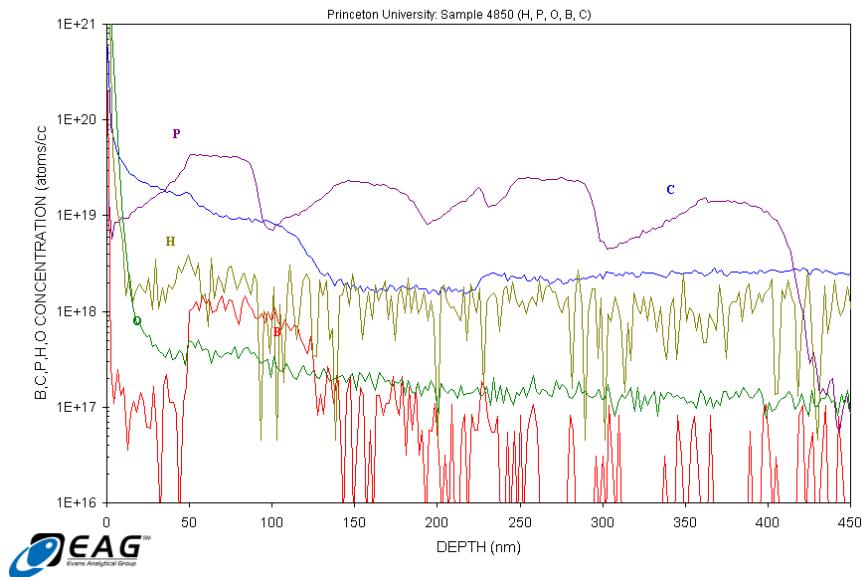


Figure E1. SIMS of sample 4050 grown with disilane at 6 torr with 3 slpm hydrogen carrier.

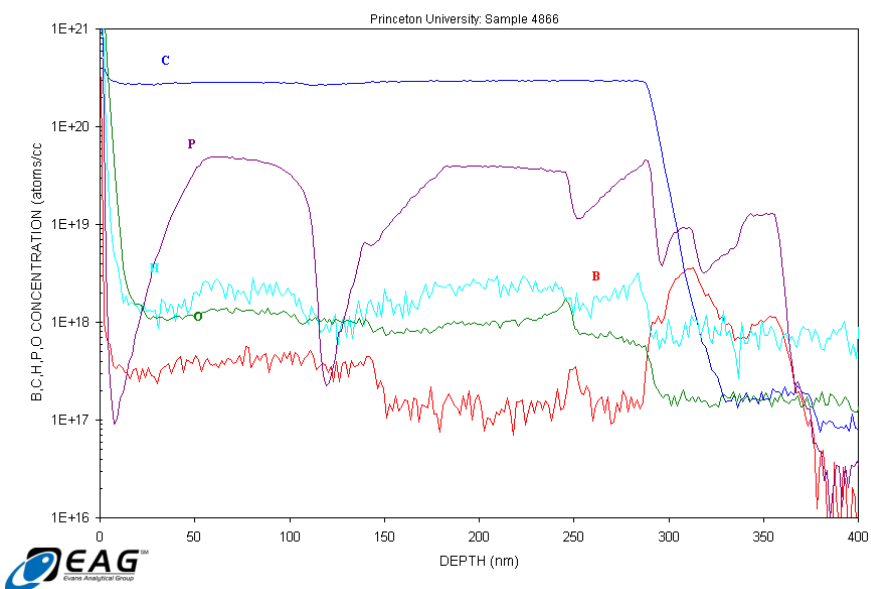


Figure E2. SIMS of sample 4066 grown with NPS and silane at 6 torr with 3 slpm hydrogen carrier. The layers grown with NPS are easily distinguishable due to the high carbon background.